# MEASUREMENT OF CAPTURE EXCITATION FUNCTIONS WITH NEUTRON-RICH NUCLEI

By

Nathan Watwood

A DISSERTATION

Submitted to
Michigan State University
in partial fulfillment of the requirements
for the degree of

Chemistry – Doctor of Philosophy

2021

## ABSTRACT

MEASUREMENT OF CAPTURE EXCITATION FUNCTIONS WITH NEUTRON-RICH NUCLEI

By

Nathan Watwood

The study of heavy and superheavy elements is important for understanding nuclear structure at the limit of stability where macroscopic and microscopic effects are delicately balanced. It is a benchmark domain for a rich variety of calculations including time-dependent Hartree-Fock (TDHF) and density functional theory (DFT). One difficulty in studying these nuclei is the low formation probability. There is limited reliability in models to predict the outcome of superheavy particle formation due to the significantly large number of degrees of freedom. The fusion-fission process is a key reaction to access heavy element formation.

Experiments were performed at the National Superconducting Cyclotron Laboratory (NSCL) at Michigan State University and at the Heavy Ion Accelerator Facility at Australian National University to measure fusion-fission excitation functions of two different combinations of Ca+Sm and K+Pb with varying neutron-richness. The excitation functions were measured at center-of-mass energies ranging from 1.1% to 0.9% above and below the predicted barrier heights. Measured cross sections were found to be comparable above the barrier regardless of neutron-richness. At and below the barrier, cross sections were enhanced for systems with positive Q-value neutron transfer channels.

Furthermore the experiment performed at the NSCL was the first measurement of fusion-fission cross sections using the Active-Target Time Projection Chamber. This experiment demonstrated the successful reconstruction and identification of fission tracks and established the viability of performing similar experiments in the future.

# TABLE OF CONTENTS

# LIST OF TABLES

# LIST OF FIGURES

# Chapter 1

# Introduction

Naturally occurring abundant elements found on Earth range from hydrogen to uranium; any heavier element is man-made and created in nuclear facilities. The primary goal of creating these super heavy elements (SHE) is to study the stability and structure of these nuclei, which exist in a domain that delicately balances macroscopic effects (Coulomb repulsion, surface tension) together with microscopic effects (shell and pairing effects). Because of this delicate balance, predicting the stability of these nuclei is difficult and is very sensitive to the quality of the model. As such, SHEs are benchmarks for nuclear models. Some models suggest the likelihood of stable SHEs with nuclear magic numbers at Z = 114, 120, 126 and N = 184 [1, 2]. In fact four new elements, Z = 113, 115, 117, 118, were added to the periodic table by the IUPAC (International Union of Pure and Applied Chemistry) in 2016 alone [3]. There is the possibility that the periodic table can even extend beyond. The study of SHEs and their creation is essential to explore this domain.

The main difficulty in SHE synthesis is the extremely low cross sections, which are of the order of picobarns [4]. There is limited reliability in models that can be used to successfully predict the outcome of such heavy particle formation due to the significant number of degrees of freedom. As heavy-ion beam facilities, such as FRIB, begin to produce neutron-rich rare isotope beams (RIBs) with high beam intensities, it opens the door to new possibilities. One possibility is the production of a group of long lived neutron-rich SHEs not accessible

with stable beams [5]. These nuclei will be important for the study of atomic physics and chemistry at the limit of stability as well as nuclear spectroscopy [6].

## 1.1 Heavy Ion Reactions

The primary method of SHE synthesis is through heavy ion fusion reactions. The process of fusion entails a projectile and target nuclei colliding and forming a single compound nucleus. In Figure 1.1 are shown the possible outcomes in a heavy ion fusion reaction. The projectile and target come into contact forming a dinuclear system (capture) and can either reseparate (quasi-fission) or form an equilibriated compound nucleus (fusion).

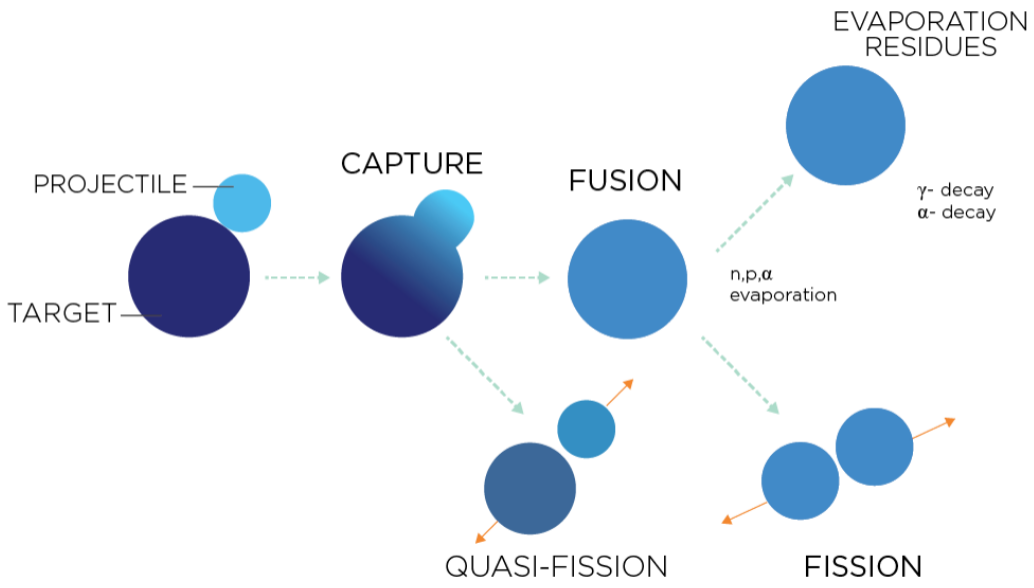


Figure 1.1: Depiction of the possible processes in a heavy ion capture reaction.

After fusion, the compound nucleus (CN) has a variable amount of excitation energy and can follow two primary exit channels in order to dissipate that energy. The first is light particle evaporation, where light particles such as neutrons, protons, gamma rays, and alpha particles are ejected from the CN, carrying with them part of the excitation energy. The

result is a heavy or super-heavy element with an N,Z slightly lower than that of the CN. The second exit channel is the binary separation of the CN nucleus into two particles with similar mass, called fission.

### 1.1.1 Capture and Fusion

The interaction between the projectile and target nuclei can be expressed by an interaction potential along their relative motion ($r_{12}$). A barrier is formed at a certain distance through a combination of Coulomb, centrifugal, and nuclear potentials where the repulsive electrostatic and centrifugal, and nuclear attractive forces are equal. This barrier determines whether capture can occur and depends on the kinetic energy of the projectile nuclei and, to a lesser degree, on the probability of quantum tunneling. Figure 1.2 describes the barrier in terms of potential energy.

Nuclear fusion is the creation of, through the capture process, an equilibrated CN generated by irreversible energy dissipation. When a compound nucleus is formed, all specific information on the entrance channel is lost [8]. Only the conserved quantities, such as energy and linear and angular momentum, are preserved in the compound nucleus.

### 1.1.2 Fission and Evaporation Residue

After compound nucleus formation and equilibrium, the compound system is in a highly excited state. The two main exit channels this system can take is the evolution to fission or to evaporation of light particles resulting in an evaporation residue. The excited compound nucleus can deform, thus decreasing the nuclear Coulomb energy. The nuclear surface energy increases until the system reaches the saddle point configuration. At saddle point, or

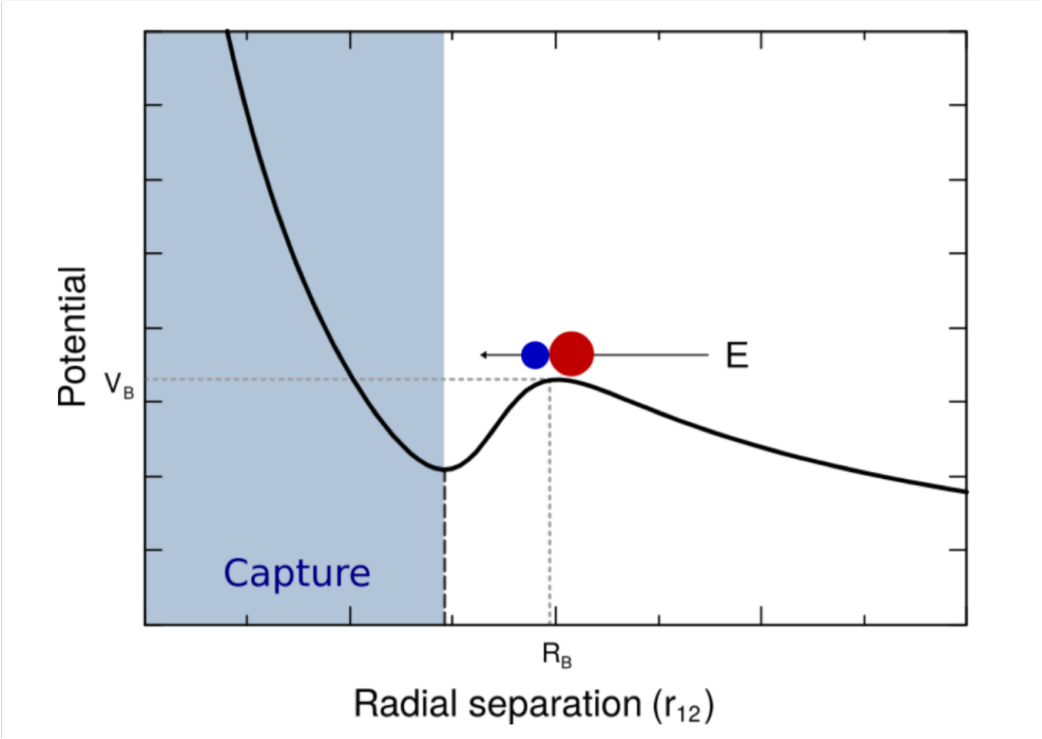


Figure 1.2: Description of the total interaction potential for a capture reaction to occur [7]. Nuclei with enough energy to overcome the fusion barrier $V_B$ at a radial separation $R_B$ will result in capture (shaded).

transition state, the rate of change between these two energies are equal. The decay of this state may lead to the separation of the compound nucleus into two smaller fragment nuclei, or fission fragments. Alternatively, if a nucleon or group of nucleons obtain enough energy to overcome the separation energy of the compound nucleus, they are evaporated from the compound nucleus and de-excite the system. A further look into these exit channels are discussed in Section 2.

## 1.2 Motivation

In a series of experiments by Loveland et al. [9] and Zyromski et al. [10, 11], the above barrier capture excitation functions using a degraded neutron rich RIB ($^{38}$S + $^{208}$Pb,$^{181}$Ta)

were measured. Figure 1.3 shows the reduced excitation functions compared to the same reaction with a stable $^{32}$S beam. In a reduced excitation function, the center of mass energy is scaled by a calculated fusion barrier from Bass systematics [12, 13] and the cross section is scaled by the interaction radius ($\pi R^2$). This eliminates the expected changes in cross section when increasing the mass of the system and the two excitation functions should overlap. It was experimentally found that the capture cross sections with the more neutron rich $^{38}$S show an increase in cross section with respect to the $^{32}$S beam. The fusion barrier heights were also measured in these experiments and compared to barrier heights calculated by Bass systematics and can be found on Table 1.1. The Bass barrier heights are expected to be higher than experimental barriers, but the change in barrier height when increasing the mass of the system should be accurately predicted [14]. The experimental results show a much larger decrease in barrier height when changing the beam from $^{32}$S to $^{38}$S than predicted by the Bass systematics. This leads to the possibility that neutron-rich beams add possibilities to the synthesis of heavy and super-heavy nuclei. The formation at lower excitation energy also might allow for higher survival probabilities of the evaporation residue.

| | **Fusion Barrier** | | | |
|---|---|---|---|---|
| **Reaction** | **Exp. (MeV)** | **Bass (MeV)** | **ΔV Exp.** | **ΔV Bass** |
| *RIB to Stable Beam Comparison* | | | | |
| $^{32}$S + $^{208}$Pb | 144.4 ± 0.2 | 147.4 | 11.1 | 3.7 |
| $^{38}$S + $^{208}$Pb | 133.3 ± 10 | 143.7 | | |
| $^{32}$S + $^{181}$Ta | 130.7 ± 0.3 | 134.1 | 5.9 | 3.4 |
| $^{38}$S + $^{181}$Ta | 124.8 ± 0.3 | 130.7 | | |
| *Stable Beam Comparison* | | | | |
| $^{32}$S+$^{208}$Pb | 144.4 ± 0.2 | 147.4 | 2.1 | 1.9 |
| $^{36}$S+$^{204}$Pb | 142.3 ± 0.2 | 145.47 | | |

Table 1.1: Barrier height comparison between stable and neutron-rich RIB reactions [9, 10, 15]

The aim of the experiments discussed in this thesis is to establish the AT-TPC as a

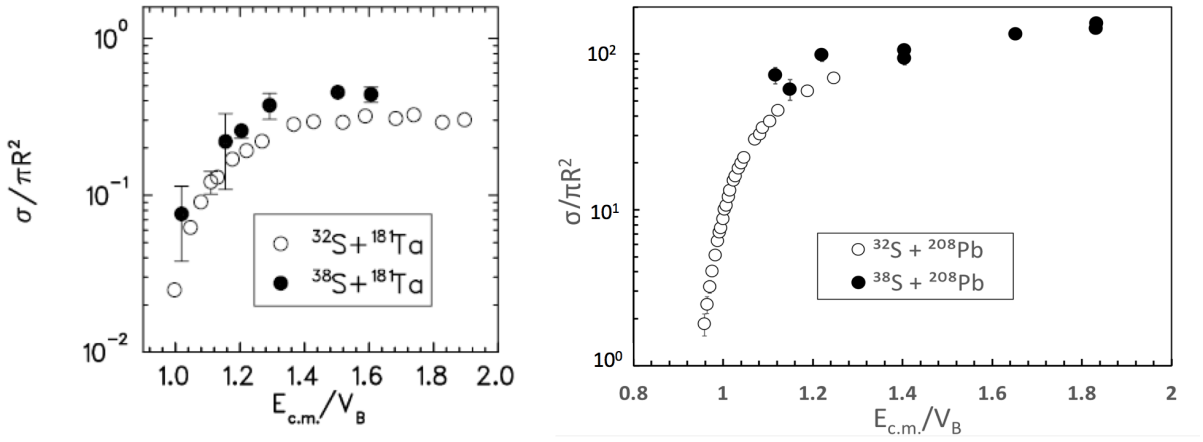


Figure 1.3: Reduced excitation functions for $^{32,38}$S + $^{208}$Pb,$^{181}$Ta, where the capture cross section is reduced by the interaction radius and the center of mass energy ($E_{c.m}$) is reduced by the barrier height ($V_B$). [9, 10]

reliable fusion-fission detector, and in turn explore other systems nearby the $^{32,38}$S + $^{208}$Pb reaction and identify the possibility of enhancements using neutron-rich RIBs.

# Chapter 2

# Theory

## 2.1 Fusion

### 2.1.1 Classical Approach - Single Barrier

The relationship between two colliding nuclei can be classically represented as an interaction potential, with contributions from repulsive Coulomb and centrifugal forces and an attractive nuclear force,

$$V_{total}(r) = V_{Coul}(r) + V_{cent}(r) + V_{nuc}(r) \tag{2.1}$$

A simple expression for the Coulomb potential between two nuclei at a distance $r$ is given by

$$V_{Coul}(r) = \frac{e^2}{4\pi\epsilon_0}\frac{Z_1 Z_2}{r} \tag{2.2}$$

where the atomic number of the colliding nuclei are represented by $Z_{1,2}$. The centrifugal potential takes into account the angular movement of the colliding nuclei in non head-on collisions and is expressed as

$$V_{cent}(r) = \frac{L(L+1)\hbar^2}{2\mu r^2} \tag{2.3}$$

where $L$ is the orbital angular momentum and $\mu$ is the reduced mass of the system. A simple version of the attractive nuclear force uses the Woods-Saxon potential [16]

$$V_{nuc}(r) = \frac{-V_0}{1 + exp[(r - R_0)/a_0} \tag{2.4}$$

with a potential depth $V_0$ and diffuseness parameter $a_0$. $R_0$ is proportional to the radius of the colliding nuclei

$$R_0 = r_0(A_1^{1/3} + A_2^{1/3}). \tag{2.5}$$

with a radius parameter $r_0$. An example of the sum of these three potentials is illustrated in Figure 2.1a. At a specific distance $R_B$, the sum of these three potentials forms a potential barrier, known as the capture barrier $V_B$. Within the barrier is a potential well wherein the projectile and nucleus irreversibly form into a compound nucleus. Both barrier height and well depth are dependent on angular momentum and can be seen in Figure 2.1b. At a critical angular momentum $l_{crit}$ the well and the barrier disappear.

Using this classical approach of a single barrier, the capture cross section can be expressed as

$$\sigma(E) = \begin{cases} \pi R_B^2(1 - \frac{V_B}{E}), & E \geq V_B \\ 0, & E < V_B \end{cases} \tag{2.6}$$

where $R_B$ is the interaction radius of the barrier at $l = 0$. This indicates the capture cross section is inversely proportional to the energy with no capture possible below the barrier. It has been used to describe capture cross sections with energies above the barrier in the region $l < l_{crit}$ [17, 18] and is also used in this work to extract barrier heights and interaction radii.

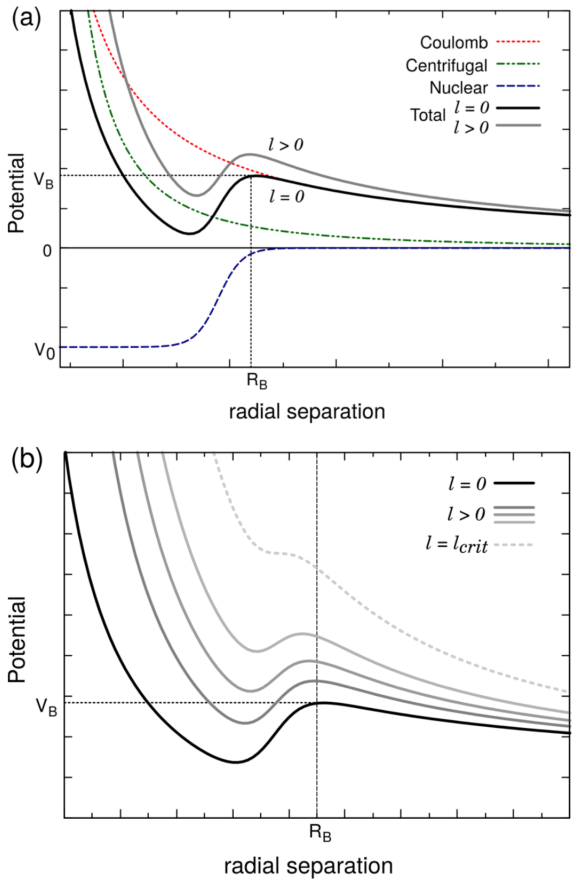


Figure 2.1: (a) Depiction of the total interaction potential of colliding nuclei when angular momentum l=0 (black) and l>0 (grey) as a function of radial separation with contributions from Coloumb repulsion (dashed), centrifugal repulsion (double dot dashed), and nuclear attraction(long dashed). $R_B$ is the capture barrier radius. (b) Depiction of the total interaction potential along increasing angular momentum l. As angular momentum increases, the barrier increases and the potential well becomes more shallow. The potential well disappears at a critical angular momentum $l_{crit}$.

As mentioned in Section 1.2, maximizing capture cross sections is important for SHE production. Using this classical approach, the capture cross sections can be increased by using neutron-rich projectiles. The interaction radius is proportional to the sum of the radii of the projectile and target nuclei, $R_B \propto (A_p^{1/3} + A_t^{1/3})$. Due to the third root, $R_B$ will increase and an increase in capture cross section is expected for more neutron rich nuclei of a particular element. Additionally, the barrier height is proportional to both the Z and A of

the colliding nuclei $V_B \propto \frac{Z_p Z_t}{(A_p^{1/3}+A_t^{1/3})}$. Therefore, increasing the total mass of the system without affecting $Z_{p,t}$, the energy required for capture is decreased.

### 2.1.2 Quantum Mechanical Approach - Single Barrier

While the classical approach can be accurate in predicting fusion cross sections above the barrier, it becomes unreliable for reactions with energies at or below the barrier due to barrier penetration (tunneling). To account for this, an angular momentum dependent transmission coefficient $T_l$ is used to represent barrier penetrability and reflection probability. The quantum mechanical approach then represents the capture cross section as

$$\sigma(E) = \frac{\pi}{k^2} \sum_{l=0}^{\infty} (2l+1) T_l(E) \tag{2.7}$$

where $(k = 2\pi/\lambda)$ is the wave vector inversely related to the de Broglie wavelength $\lambda$. The transmission coefficient can be calculated using the parabolic barrier approximation, Wentzel-Kramers-Brillouin (WKB) approximation, or the optical model [19, 20].

Heavy ion fusion experiments in the 1970's and 1980's found that measured capture cross sections were significantly higher than the predicted cross sections using this quantum mechanical single barrier penetration model and thus subsequently revealed that nuclear structure had a profound effect on fusion reactions [21, 22, 23].

## 2.2 Modelling Fission

The nuclear matter within an equilibrated CN with some excitation energy, angular momentum, shape, and fissility, will be expected to fluctuate shape with various oscillations that

can lead to deformations of the CN. These deformations can cause the splitting, or fissioning, of the nucleus into two or more fragments of similar mass. This process is contingent on the potential energy landscape described by the shape deformation of the CN and the mass asymmetry of the fissioning system. During deformation, the repulsive forces between constituent nucleons counteract the restoring nuclear forces that are responsible for the surface tension of the nucleus. Figure 2.2 shows an example of a potential energy surface (PES) of a CN as a function of deformation and mass asymmetry [24]. An adequate excitation energy is required for the evolution of the CN from the equilibrated initial state to the saddle point and finally to fragment separation, although quantum tunneling through the potential barriers is also possible [25]. The optimum fissioning path is then an evolution of deformation configurations within the valleys of minimum potential energy leading to scission.

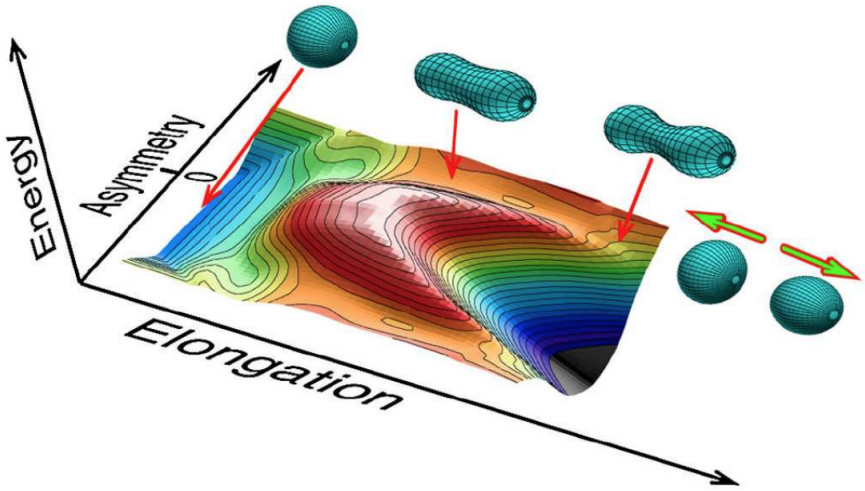


Figure 2.2: Example of the potential energy surface of $^{180}Hg$ as a function of nuclear deformation and mass asymmetry [24]

Fission is a complex, dynamical process that cannot be described perfectly by macroscopic models and is typically too complex to be solved accurately by microscopic many-body calculations [26]. As a result, the PES of a fissioning system is often described by mean-field

theories or macroscopic-microscopic models [27, 28, 29, 30]. In the macroscopic-microscopic models, the macroscopic potential may be generated from the liquid drop model (LDM) [31] and corrected by microscopic shell-structure and pairing effects [32]. Even these models must be considered as approximations, since the generated PES is a static representation of a time-dependent process.

The LDM describes three main contributions to the potential energy of deformation: the Coulomb repulsion between nucleons within the nucleus, the surface tension on the outside of the nucleus stemming from attractive nuclear forces, and angular momentum, which energetically favors large moments of inertia. For small quadrupole distortions, the radius of a nuclear sphere at the lowest order is expressed as

$$\begin{aligned} R(\theta) &= R_0(1 + \alpha_2 P_2(cos\theta)) \\ \alpha_2 &= \sqrt{\frac{5}{4\pi}}\beta_2 \end{aligned} \tag{2.8}$$

where $P_2$ is the Legendre polynomial and $\beta_2$ is the quadrupole deformation parameter. The Coulomb $E_c$ and surface $E_s$ energies can then be represented by quadrupole deformation parameters as

$$\begin{aligned} E_c &= E_c^0(1 - \frac{1}{5}\alpha_2^2) \\ E_s &= E_s^0(1 + \frac{2}{5}\alpha_2^2) \end{aligned} \tag{2.9}$$

$E_c^0$ and $E_s^0$ are the energies of a uniformly charged sphere and can be represented as

$$\begin{aligned} E_c^0 &= \frac{3}{5}\frac{Z^2e^2}{R_0A^{1/3}} \\ E_s^0 &= 4\pi R_0^2 S A^{2/3} \end{aligned} \tag{2.10}$$

where $R_0$ is the radius of the sphere, S is the surface tension energy parameter, A is the

nuclear mass, Z is the atomic number, and $e$ is the charge of an electron. Using the above terms, the deformed LDM energy is

$$E_{LD} = E^0_{LD} + \frac{1}{5}\alpha_2^2(2E^0_s - E^0_c) \tag{2.11}$$

When the changes of the Coulomb and surface energies are the same, the CN becomes unstable and the relation between the uniform surface and Coulomb energies becomes

$$x = \frac{E^0_c}{2E^0_s} = (\frac{a_c}{2a_s})(\frac{Z^2}{A}) = (\frac{Z^2}{A})/(\frac{Z^2}{A})_{critical} \tag{2.12}$$

where $a_c = 3e^2/5R_0$, $a_s = 4\pi R_0^2 S$, $(\frac{Z^2}{A})_{critical} = (a_c/2a_s)^{-1}$, and $x$ is the fissility parameter. The fissility parameter is used to determine if a CN will fission; if $x > 1$, the CN will fission, if $x < 1$, the CN will equilibrate as a spherical or moderately deformed nucleus. This description is true only in macroscopic conditions as it doesn't account for pairing or shell effects. As mentioned in Section 1, SHE production is difficult due to the extremely low cross sections. Using the expression for fissility, increasing the mass of the system with a near constant Z (neutron-rich beam) would lead to a decrease in fissility of the CN, which would increase the survival chance of a SHE's.

The LDM, using macroscopic effects, can describe the fission barrier with basic features like in Figure 2.3. However, to get a more accurate representation of the fission barrier, shell effects and pairing corrections need to be included. Strutinsky proposed a technique for including these microscopic effects into the total energy of the compound nucleus by

$$E = E_{LDM} + \sum_{(p,n)} (\delta S + \delta P) \tag{2.13}$$

where the sum of the shell effects and pairing corrections ($\delta S + \delta P$) are added to the energy of the LDM ($E_{LDM}$) [33]. The addition of these effects produces a more complex fission barrier for heavy nuclei and is illustrated in Figure 2.3. A double humped or even triple humped barrier can exist with deep secondary and tertiary minima. The addition of asymmetric and symmetric deformations transforms the barrier into a multidimensional surface, making calculation of the barrier height a complex task.

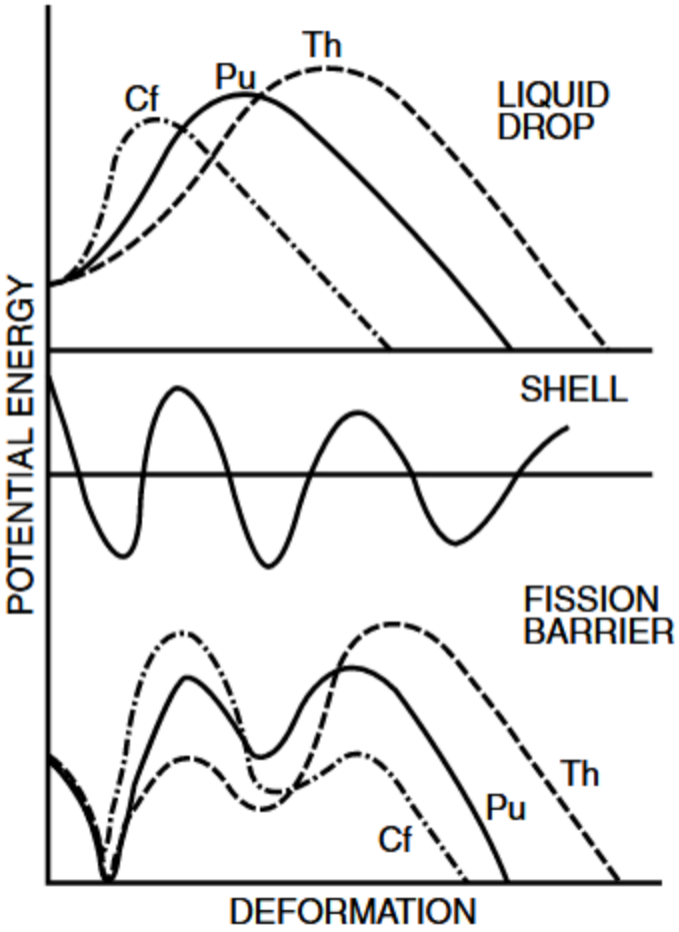


Figure 2.3: Illustration of 1-dimensional interaction potentials for Cf, Pu, and Th nuclei as a function of deformation using the liquid drop model (top), shell effects (middle), and the combination of the both (bottom). [34]

The fission decay width can be described by Bohr and Wheeler's transition-state model

(TSM) [35, 36]. The transition-state model can be used to describe the CN at the saddle point as a transition state between scission and the equilibrated CN and the decay rate depends on the level density of states above the fission barrier. This model characterized the fission process as having to compete with other modes of nuclear de-excitation, and that the decay width could be written as

$$\Gamma_f = \frac{N_f}{N_f + N_n + N_\gamma + N_{ch.p}} \tag{2.14}$$

where $N_x = 2\pi\Gamma/D$ is the level density of exit channels for each de-excitation channel. The calculation of $N_f$ requires an evaluation of the level density of the transition state nucleus.

The transition-state model calculates the decay width of fission using three quantum numbers: 1) the total angular momentum of the system J, the projection of J onto the nuclear symmetry axis K, and the projection of J onto the fixed space axis M. (Figure 2.4). This model makes the assumption that fission fragments separate along a nuclear symmetry axis that remains unchanged throughout the fission process. Quantum numbers J and M are conserved throughout this process and K is determined at the saddle point configuration. Using this model, the decay width of a CN can be expressed as

$$\Gamma_f^{BW} = \frac{1}{2\pi\rho(E_i)} T_{sad}\rho(E_i - B_f) \tag{2.15}$$

where $T_{sad}$ is the nuclear temperature at the saddle point. The nuclear temperature describes the kinetic energy of the system or the velocity in which the fragments cross the saddle point, therefore can be represented as the transition rate. $B_f$ is the fission barrier that can be calculated by Sierk's finite-range drop model [37] with corrections from the

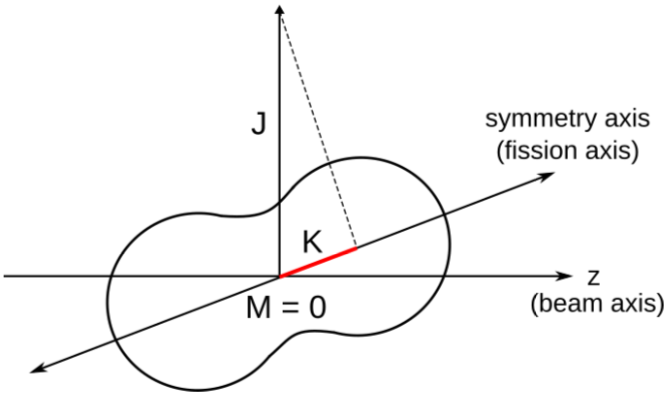


Figure 2.4: Illustration of the angular momentum vectors at the saddle configuration for a fissioning nucleus. In the transition-state model for fission, the angular distribution of fission fragments can be expressed as a function of the total angular momentum J and the projection of J onto the fission axis K at the saddle point if the projection of J onto the space fixed axis (here the beam axis) M=0.

ground-state shell structure. The TSM can also be used in predicting the fission angular cross sections[38] and is described in more detail in Section 6.3

Using a one dimensional diffusion model, Kramers [39] formulated a similar representation of the fission decay width. For a large viscosity, the width is expressed as

$$\begin{aligned} \Gamma_{Kramers}(E^*, J) &= f_k \Gamma_f^{BW}(E^*, J), \\ f_k &= \sqrt{1 + (\frac{\gamma}{\omega})^2} - \frac{\gamma}{\omega} \end{aligned} \tag{2.16}$$

where $\gamma$ is the magnitude of viscosity and $\omega$ is the curvature of potential energy at saddle point.

A simple approach to the kinetic energy of fission fragments is the result of Coulomb repulsion after scission and can be expressed as

$$TKE = \frac{Z_1 Z_2}{r_0(A_1^{1/3} + A_2^{1/3})} \tag{2.17}$$

where $r_0 = 1.8$ instead of the typical value of 1.2 due to the highly deformed fragments

at scission. More empirically derived representations of fragment TKE are given by Viola et. al [40]. The excitation energy of the fission fragments can be calculated as the difference between the Q value of the reaction and the TKE of the fission fragments.

## 2.3 Nuclear Codes

The fusion-fission process can be modelled through a number of different codes [41, 42, 43, 44]. This section describes the relevant codes used in this analysis.

### 2.3.1 General Description of Fission Observables

The **GE**neral Description of **F**ission Observables (GEF) is a model that utilizes a large body of empirical fission observables for a general description of the fission process. It provides a reliable prediction of fission observables for fissioning nuclei ranging from Polonium to Seaborgium with excitation energies up to 100 MeV. GEF uses the Monte Carlo method to calculate event by event fission observables of two fragments at fission, as well as the nuclear de-excitation of the fragments, including prompt gamma and neutron emission. The potential energy surface is calculated using the macroscopic-microscopic approach, relying on the "separability principle" to empirically determine the stiffness of the macroscopic potential and the position and strength of fragment shells.

The fission decay width is calculated using a primarily macroscopic approach by Hasse [45] with a few extensions and is expressed by

$$\Gamma_f = \frac{F_{rot} T_f}{G \cdot exp(B_{max}/T_f)}) \tag{2.18}$$

where $B_{max}$ is the maximum value of the inner and outer fission barriers, $T_f$ is the

nuclear temperature of the compound system at $B_{max}$. $F_{rot}$ is the influence of the rms angular momentum distribution, which is dependent on fissility and nuclear temperature. $G$ considers the collective enhancement of the level densities at the top of the inner and outer barriers as well as barrier penetrability.

The excitation energy partition between the fragments is determined through statistical mechanics, where the assumption is made that all energetically possible configurations in the system have equal probabilities to be populated. The average excitation energies can be determined with a probability distribution that is a product of the level densities of each fragment

$$< E_L >= \frac{\int_0^{E^*_{intr}} E_L \rho_L(E_L)\rho_H(E^*_{intr} - E_L)dE_L}{\int_0^{E^*_{intr}} \rho_L(E_L)\rho_H(E^*_{intr} - E_L)dE_L} \tag{2.19}$$

where $\rho_L$ and $\rho_H$ are the level densities of the light and heavy fragments respectively, and $E^*_{intr}$ is the intrinsic excitation energy determined from the sum of the excitation energy above the barrier plus the dissipated potential energy after the saddle point. Further explanation of GEF can be found in the documentation by K. H. Schmidt [46, 47, 48].

### 2.3.2 Decay of Excited Nuclei

In this work, the Decay of Excited Nuclei is described by a Monte Carlo method for calculating the evaporation residue cross sections as utilized in LISE++. It randomly selects an exit channel based on a probability distribution that is expressed as

$$P_b = \frac{\Gamma_b}{\Gamma_{total}},\ b = n, p, \alpha, \gamma, fission \tag{2.20}$$

The decay widths for particle emission are described as

$$\Gamma_{C\to B+b}(E^*,J)=\frac{2s_b+1}{2\pi\rho_C(E^*,J)}\int_0^{E^*_{B_b}}\sum_l T_l(e_b)\cdot\sum_{I=|J-l|}^{I=J+l}\rho_B(E^*-B_b-e_b,I)de_b \quad (2.21)$$

where $s_b$ is the spin of emitted particle b, $B_b$ is its binding energy, and $T_l(e)$ and $e_b$ are the transmission coefficient and kinetic energy of the particle respectively. The fission barrier used is the sum of the LDM barrier height plus the shell corrections corresponding to the ground state Q-value. Further documentation can be found [49].

### 2.3.3 GEMINI++

Gemini++ is a statistical model calculation for the evaporation of high spin CN. The evaporation of light particles is implemented within the Hauser-Feshbach formalism [50] in which spin degrees of freedom are taken into account. The partial decay width of a CN with excitation energy $E^*$ and spin $J_{CN}$ for a light particle $i$ is

$$\Gamma_i(E^*,J_{CN})=\frac{1}{2\pi\rho_{CN}(E^*,J_{CN})}\int d\epsilon\sum_{J_d=0}^{\infty}\sum_{J=|J_{CN}-J_d|}^{J_{CN}+J_d}\sum_{l=J-S_i}^{J+S_i}T_l(\epsilon)\rho_d(E^*-B_i-\epsilon,J_d) \quad (2.22)$$

where $J_d$ is the spin of the resulting nucleus, $T_l$ is the transmission coefficient, $S_i, J, l$ are the spin and orbital and angular momentum of the evaporated particle, and $\epsilon$ and $B_i$ are its kinetic and separation energies respectively. The level densities are approximated using the Fermi-gas form [51], which is obtained using a spherical nucleus with constant single-particle

level densities in the independent particle model and is expressed as

$$\rho_{FG}(E^*, J) = \frac{2J+1}{24\sqrt{2}a^{1/4}U^{5/4}{}_{\sigma^3}} exp(S) \tag{2.23}$$

where $\sigma^2$ is the product of the moment of inertia of a rigid body, $S$ is the nuclear entropy, $U$ is the thermal excitation, and $a$ is the level density parameter.

The model calculates the fission decay width using the Bohr-Wheeler formalism using the angular momentum dependent fission barriers of Sierk [52], assuming the level densities from ground-state to saddle-point are identical except for a scaling factor. Further explanation is provided by R.J. Charity [53, 54].

# Chapter 3

# Michigan State University Experiment

## 3.1 Active Target Time Projection Chamber

The main goal of the experiments described below was to measure fission fragments for the first time using the Active Target Time Projection Chamber (AT-TPC). This chapter will consist of a brief summary of time projection chambers (TPCs) and a more detailed description of the AT-TPC.

## 3.2 Background

### 3.2.1 Ionization Chambers

An ionization chamber is a simple radiation detector that measures ionizing radiation with no electron amplification. It consists of a gas filled chamber with an applied voltage across an anode and cathode, creating a uniform electric field. The electrodes can be oriented in either a parallel plate configuration or a cylindrical orientation where a wire anode runs coaxially through the center of the detector. When an incident ionizing particle enters the chamber, the particle will produce an ionizing track in the detector gas, creating ion pairs.

The number of electron-ion pairs generated is dependent on the density, atomic number, and the ionizing potential of the gas as well as the atomic number and energy of the incident particle. Under the influence of the electric field, the positive ions and the freed electrons will move towards the oppositely charged electrodes with a drift velocity that is dependent on the electric field and type and pressure of the gas. In general, the typical drift velocity of electrons (10's of cm/$\mu$s) is much slower than the speed of the incoming particles (0.3c) and the drift velocity of the positive ions is typically a factor 100 smaller than the negative ions [55]. This generates a small ionization current that can then be measured by an electrometer circuit.

The energy loss of ionization radiation in a gas has been studied and modelled to a good precision. Several tools allow for the prediction of energy loss of particles in mediums; the program TRIM (TRansport of Ions in Matter) utilizes data to infer energy loss. A simpler approach is the Bethe-Bloch formula, which expresses the stopping power S as

$$S = \frac{4\pi Z_2 e^4}{mv^2} Z_1^2 \left[ ln\frac{2mv^2}{< I >} - ln(1-\beta^2) - \beta^2 + \Psi(Z_1) \right] \tag{3.1}$$

Given a velocity of the incoming particles in a detector gas, the energy loss of an incoming particle is proportional to the square of the number of protons of a particle. Hence, ionization chambers can provide energy loss and total energy. This information can be used to determine the Z and mass/charge of the beam, respectively.

### 3.2.2 Time projection chambers

A time projection chamber is a gas filled chamber used to detect charged incoming particles. It was originally invented in the 1970s by David Nygren [56] and was used to study high

energy electron-positron collisions at Lawrence Berkeley Laboratory. When a charged particle enters the detector, it ionizes a number of the atoms of the chamber's gas proportionally to the amount of energy the charged particle loses in the gas. The result is a trail of free electrons that will then drift in a mostly uniform electric field produced by an anode and cathode within the detector. Near the anode of the chamber there is electron amplification and a position sensitive readout that measures the number of electrons. This is where it differs from an ionization chamber

The 3-dimensional coordinates of the electrons are measured; 2-dimensions coming from the 2D-position sensitivity of the readout, and the 3rd dimension can be reconstructed from the timing of the signals from the electrons relative to the timing of the trigger signal. Because the drift velocity of the free electrons is constant in a gas in a homogeneous field, the timing of each signal is equivalent to a space coordinate, hence the title 'time projection' chambers [57].

### 3.2.3 Active Target

In order to fully observe the products of a nuclear reaction within a TPC, the target of the reaction needs to be inside the detector where the beam particles enter. One way to do this is by making the ionizing gas and the target gas the same, or an active target [58]. There are advantages to using this method over the traditional solid target. Reaction detection solid angle is essentially $4\pi$. Without any compromise on target thickness, reactions can happen anywhere in the detector volume, resulting in the measurement of a reaction at a continuum of energies as the beam traverses the detector, instead of measuring just one energy with a thin target. As a result, excitation functions of reactions can be measured without changing the initial beam energy.

There are some constraints to this method as well. Primarily the inner volume gas needs to have good electron transport and amplification properties and it must contain the target nuclei of interest. A thin solid target was introduced for this experiment as $^{208}$Pb does not exist in gaseous form. This will be discussed in more detail in Section 3.4.6.

## 3.3 Structure of AT-TPC

The AT-TPC is a variation of a TPC that mainly is used in the active target mode. In the instance of this experiment, as solid target was used. The following section comprises a brief description of the AT-TPC. A more complete description of the half-scale prototype version (pAT-TPC), which was also used in experiments described in this dissertation, can be found in the dissertation by Carpenter et al. [59] and in the articles written by Suzuki et al [60, 61]. The full size detector is described in depth by the dissertation written by Bradt et al [62]. A schematic of the detector can be found in Figure 3.1.

### 3.3.1 Inner and outer gas volumes

The inner volume of the detector is contained in an epoxy coated fiberglass cylinder with a radius of 29.2 cm and a length of 1 m. The inner volume is ended on the downstream end by an aluminum frame that supports the sensor plane which operates as an anode. On the upstream end there is an aluminium plate that acts as the cathode. Within the center of the cathode is a 1 cm hole where the beam enters the detector. A thin foil window is mounted over this hole to seal the chamber from the high vacuum beam line, allowing the beam to enter with a minimum energy loss.

The outer volume of the AT-TPC is a stainless steel cylinder with a diameter of 50

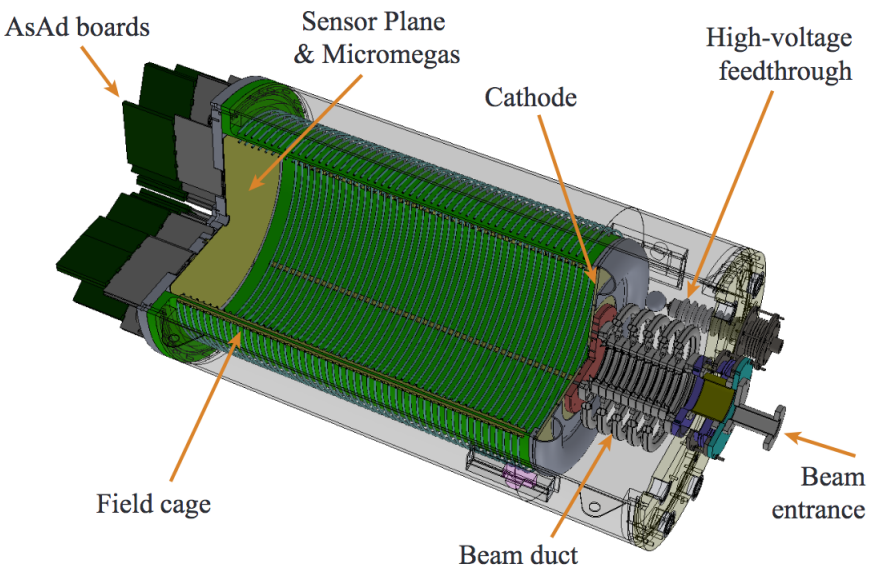


Figure 3.1: Schematic view of the Active Target Time Projection Chamber. The outer shielding was made transparent and a quarter section of the inner volume was cutout to make the details more visible. The beam enters the detector through the beam duct at the right-hand side and travels towards the sensor plane on the left. Some of the electronics described in Section 3.3.4 are shown mounted on the left-hand side

centimeters and a length of 1.4 meter that encapsulates the inner volume. The purpose of the outer volume is two-fold. First, the inner volume usually operates below atmospheric pressure and must be pumped down to a vacuum in order to be filled with the working gas. The thick stainless steel outer volume can withstand these pressure differentials and protects the less robust inner volume from being damaged by pressure. Second, the outer volume isolates the high electric potential produced by the cathode from the environment. The outer volume is filled with an inert gas with a high dielectric constant such as nitrogen in order to prevent sparking or arcing. The detector is designed for cathode voltages up to 150kV at 1 atmosphere. It is important to maintain the purity of the inner volume gas in order to maintain a constant drift velocity and amplification. The outer volume pressure is kept at a slightly lower pressure than the inner volume in order to prevent contamination of

the inner volume caused by micro-leaks .

### 3.3.2 Micromegas

On the downstream side of the detector near the sensor plane, ionized electrons are amplified by a fine conductive mesh called a Micromegas ("micro-mesh gaseous structure") [63]. A Nickel grid is placed 100$\mu$m above the sensor plane and a negative voltage of the order of 500V is applied to the grid. This produces a large electric field gradient between the mesh and sensor plane of the order of 50kV/cm. An electron passing through the mesh causes an electron avalanche before reaching the sensor plane, which amplifies the signal of that single electron by a factor of up to $10^6$. An illustration of the process can be found in Figure 3.2.

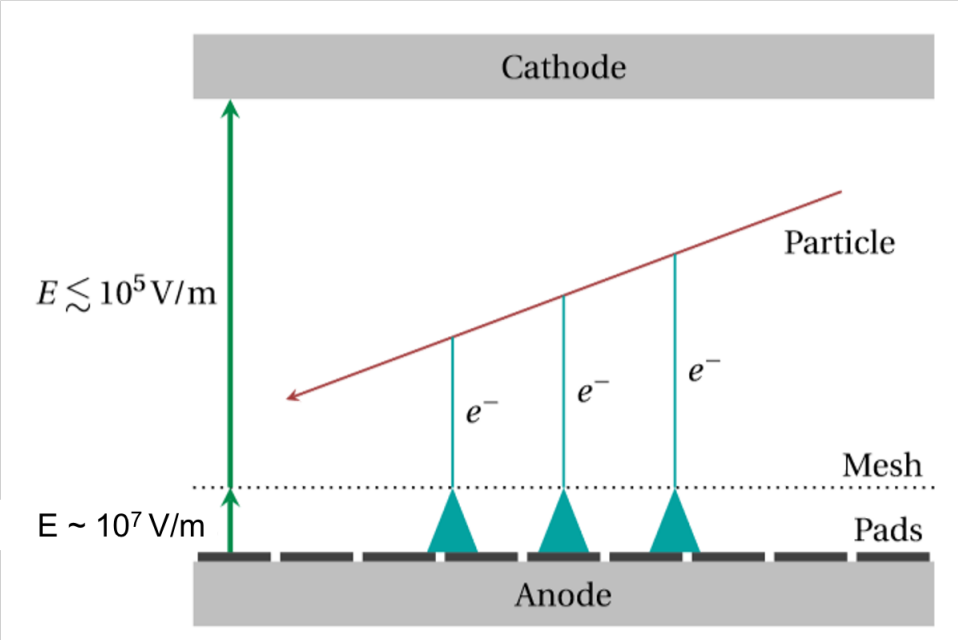


Figure 3.2: Illustration of Micromegas operation within the TPC. The electric fields will vary depending on the details of the experiment. This image is not to scale.

### 3.3.3 Sensor plane

The sensor plane is a circular printed circuit board with a radius of 27.5 cm and consists of 10,240 gold plated conductive pads. The plane is arranged with an hexagonal inner region of triangular pads with a height of 0.5cm surrounded by a circular region of triangular pads with a height of 1.0cm. A depiction of the sensor plan can be found in Figure 3.3. The pads are triangular in order to maximize spatial resolution. As a track of electrons from an ionizing particle reaches the sensor plane, the charge deposited on the sensor plane will be sampled by these triangular pads. The charge measured by each pad will change drastically depending on the location of the track on the triangular pad. With a detailed fitting procedure a localization much finer to the dimension of the pad size may be achieved.

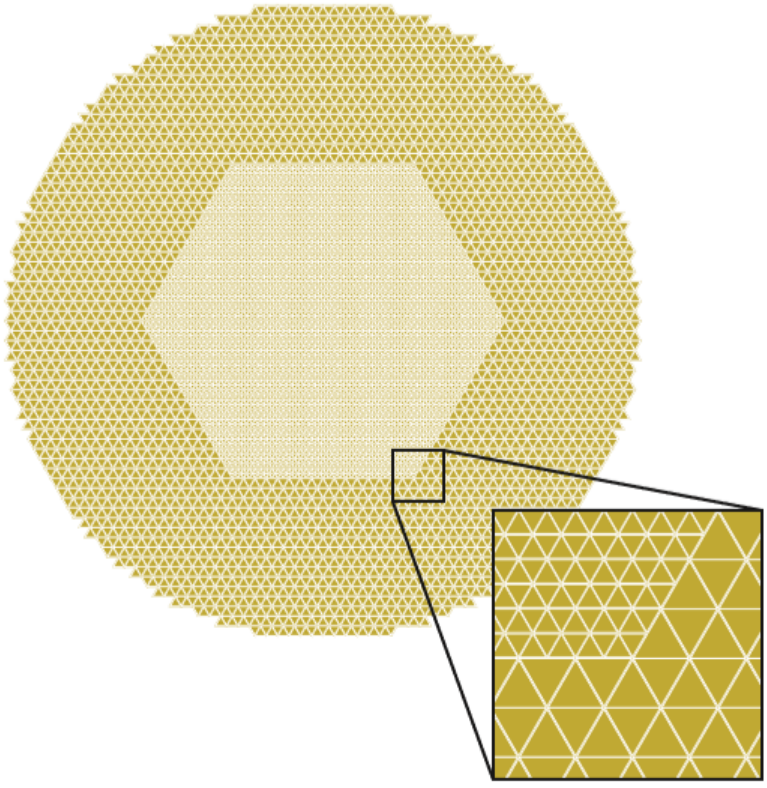

Figure 3.3: Illustration of AT-TPC sensor plane. The bottom right image is a zoomed cutout of the sensor plane showing the transition between large and small pads.

### 3.3.4 Electronics

The electronics used for the AT-TPC data collection are the General Electronics for Time Projection Chambers (GET), which were developed by a collaboration [64]. These electronics are used for amplification, digitization, and storage of data from every pad on the sensor plane. GET is divided into a number of modules. The first module is the Application Specific Integrated Circuit (ASIC) for GET electronics (AGET). This chip shaped, amplified, and sampled 64 channels at a frequency of 25MHz and stored them in a Sampling Capacitor Array (SCA) that acts as a circular buffer[65, 66]. The chip also compared the signal to a set threshold to generate a leading edge discriminator signal.

Four of these AGET chips are mounted on an AsAd (ASIC Support and Analog to Digital Conversion) board. The ADC, mounted along with the four AGET chips, digitizes the multiplicity of the leading edge discriminator of each AGET and transmits it to a different module, the CoBo. When a trigger signal is sent, the ADC is switched to digitize the signals stored in the SCA of the four AGET chips and transmits them via serial link.

The data from the AsAd boards are passed to the CoBo's (Concentration Boards, developed at the NSCL), which can house up to 4 AsAd's, which is 1024 channels. Each CoBo calculates the number of channel triggers digitized by the AGET chips and can be used to issue a global trigger. When a global trigger is issued, the CoBo reads the data in the SCAs from each AsAd, applies a local timestamp, and builds and stores the event on a cluster of computers. An illustration of the electronics can be found in Figure 3.4 and a logic circuit of the AGET chip can be found in Figure 3.5.

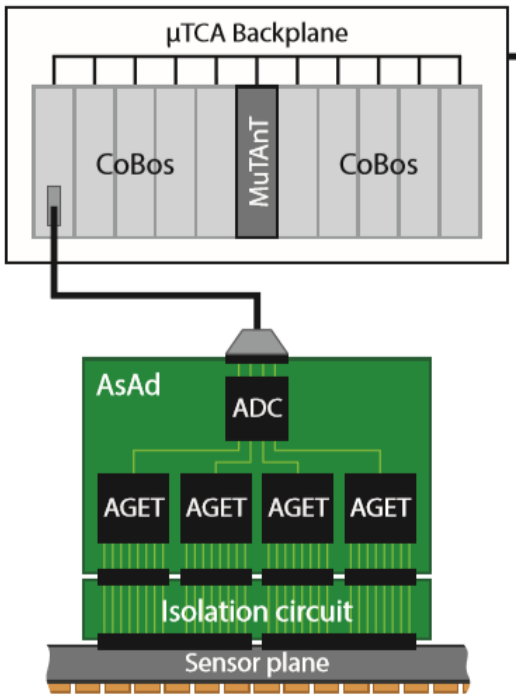


Figure 3.4: Illustration of electronic hierarchy used for the AT-TPC. The illustration only shows the inside of one AsAd, but it is important to note that 40 AsAds and 10 CoBos are used during experiments

### 3.3.5 Tilting the Detector

While the AT-TPC is usually aligned such that the beam traverses the center of the detector, there is the possibility of tilting the detector. The AT-TPC support can tilt the anode of the detector up to 6° around the entrance window with regard to the beam axis. This orientation of the detector can be beneficial for post-experiment analysis for a couple reasons. The first is that forward angle charged particle tracks are extended over a number of pads instead of just one or two in the centered orientation. This will lead to better measurements of reaction products at small angles. Another benefit for a tilted orientation is that events with multiple incoming beam particles, or pileup events, can be separated from each other, as events that occur farther away from the window will have an origin farther away from (0,0) on the pad plane. An illustration of this orientation can be found in Figure 3.6.

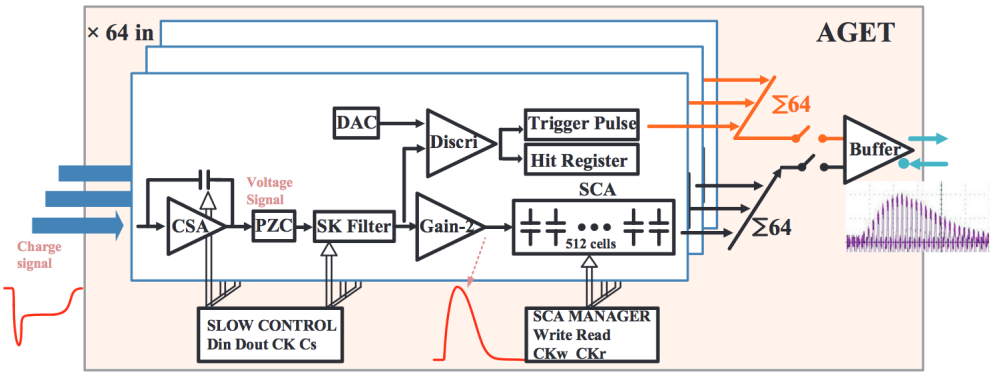


Figure 3.5: Logic diagram of the Application Specific Integrated Circuit for GET electronics (AGET) [67].

### 3.3.6 Electric and Magnetic Fields

A uniform electric field is generated within the detector in order to transport the free electrons towards the sensor plane for detection. This is done by applying a potential difference between the cathode at the upstream end of the detector and the anode at the downstream end. Uniformity of the field is obtained by a field cage consisting of 50 concentric ring electrodes through the length of the detector that are attached to a chain of resistors. The chain of resistors decreases the voltage across each ring as it progresses from the upstream end to the downstream end. A picture of the field cage can be seen in Figure 3.7 while the detector was being assembled. There are two rows of rings, one inside and one outside of the field cage. Each inner ring is in electric contact with an outer one to keep homogeneity of the electric field.

A coaxial magnetic field can also be applied to the detector by placing the detector in a large bore solenoid magnet. At the NSCL, a re-purposed MRI magnet was used, allowing for fields up to 2T. The magnetic field will bend the charged particles; if the range of the particle is long enough and the radius of curvature is small enough, they will spiral down

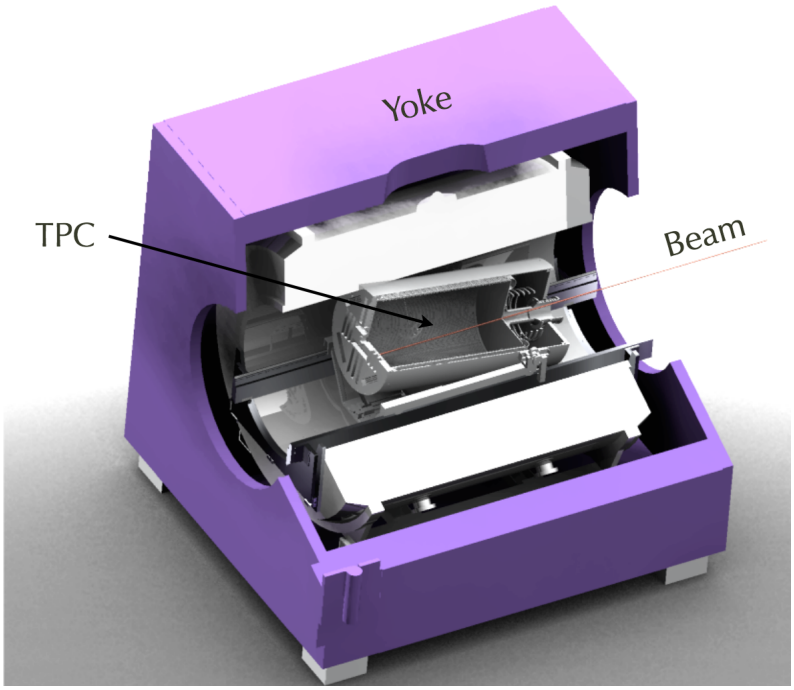


Figure 3.6: Illustration of the AT-TPC tilted inside the solenoid magnet. The detector can be tilted up to 6° and the magnet can reach a uniform magnetic strength of 2T.

the length of the detector as they lose energy in the gas. A charged particle with velocity $v$, mass $m$, and charge $q$ in a magnetic field $B$ will move in a circle radius

$$\rho = \frac{mv}{Bq}. \tag{3.2}$$

With the particles kinetic energy being $E = 1/2mv^2$, the measurement of the magnetic rigidity by the curvature of the track allows for a precise energy measurement by

$$E = \frac{B^2\rho^2q^2}{2m} = \frac{B^2\rho^2Z^2e^2}{2Am_p}. \tag{3.3}$$

The AT-TPC inside a magnetic field is also the only way to identify particles that do not completely stop within the detector. Without collecting all of a particles energy in the gas, measuring the radius of curvature is the only way to identify the particle and measure

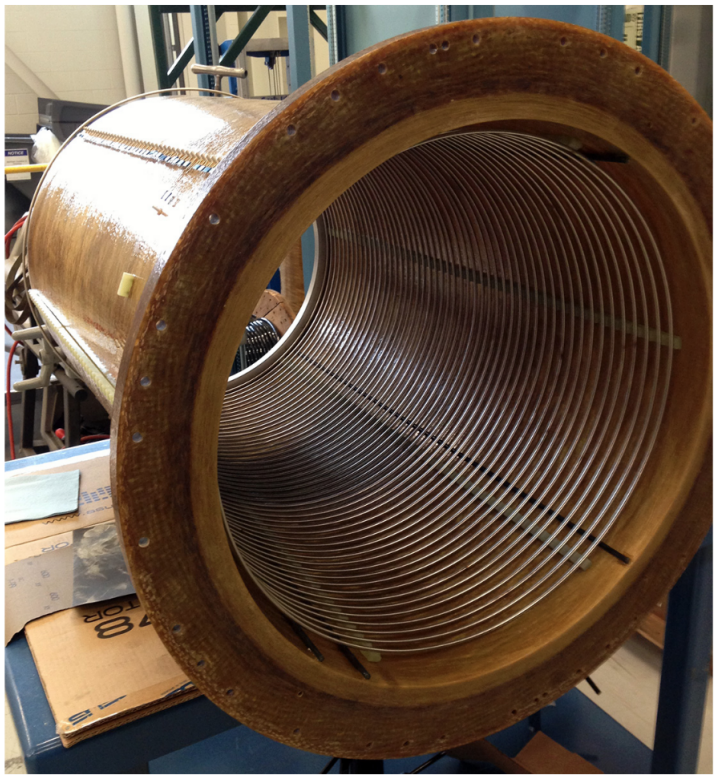

Figure 3.7: Picture of the rings of the field cage inside the inner volume of the AT-TPC detector

its momentum. For this experiment the magnetic field was not used.

### 3.3.7 Trigger

Before a trigger is produced, the GET electronics is used to execute two tasks in the waiting phase: 1) writing all channels in their circular SCA and 2) digitizing the leading edge discriminator signals and sending the result to the CoBo. A trigger signal will be produced if there is an event of interest. When it is delivered to the GET electronics it 1) stops writing in the SCA and 2) starts the digitization readout of all the sampling capacitors.

There are several primary triggers that can be used for the data acquisition of the AT-TPC; the specific setup varies with the goal of each experiment and on other ancillary detectors used in conjunction with the AT-TPC. The first trigger originates from the output of the Micromegas mesh. The mesh receives the sum of the current of all the pads (with opposite sign). This current is passed to a preamplifier-amplifier chain. A single channel discriminator may then select an experimentally set amplitude window that is dependent on the specific experiment. The output of the discriminator is then sent to the data acquisition as a trigger signal.

A second possible trigger is an internal multiplicity trigger within the GET electronics, which operates as a "number of pads with a signal" trigger. As mentioned in Section 3.3.4, the ASIC chip can compare the signal of each pad to a set threshold and generate a leading-edge trigger. In each CoBo a channel trigger threshold can be manually set, where if a certain number of channel triggers occur within a time period, 6$\mu$s for the fusion-fission experiment described in this dissertation, then the CoBo outputs a trigger signal. The trigger outputs of each CoBo are then set in an OR logic circuit, and the output of the OR circuit are sent to the data acquisition as a trigger signal. This signal can also be coupled with the

mesh trigger. Alternatively, a global multiplicity signal can be produced by the MuTAnt (Multiplicity, Trigger, and Time) module that can sum the multiplicity of all the CoBos [68]. Eventually, coincidence will be required between the different trigger signals and external detectors such as an ionization chamber or MCP.

## 3.4 Experimental Setup of the AT-TPC

The AT-TPC was chosen for this experiment essentially for its 100% detection efficiency. The AT-TPC will detect every ionizing particle that enters the detector, which ensures no loss of incoming particles. This is especially important when performing experiments that measure differential and total cross-sections as this eliminates any need for normalization. In respect to the fission experiment itself, with a solid target the detector will have a solid angle efficiency of $2\pi$ which will ensure the detection of one if not both fission fragments in a fission event. Finally, the difference of the ranges in the detector volume will make the identification of beam particles and fission fragments straightforward.

### 3.4.1 Rare Isotope Beam Production

A beam of $^{46}$K was produced by the Coupled Cyclotron Facility at the National Superconducting Cyclotron Laboratory at Michigan State University [69]. The layout of the beam-line can be found in Figure 3.8. A primary beam of $^{48}$Ca, ionized in a superconducting ECR (Electron Cyclotron Resonance) ion source, was accelerated to an energy of 140 MeV/u after the two coupled cyclotrons. The primary beam was then fragmented by a stable beryllium target in order to produce a large number of isotopes, including the desired $^{46}$K. The cocktail beam is then delivered to the A1900 fragment separator [70], where four dipole magnets

separate the beam based on momentum over charge (magnetic rigidity). A sketch of the A1900 fragment separator can be found in Figure 3.9. Once the secondary beam is filtered, it exits the fragments separator with an energy much higher than desired for the scope of this experiment. As a result, the beam is stopped and re-accelerated to the desired energy, which is done using the ReA3 facility.

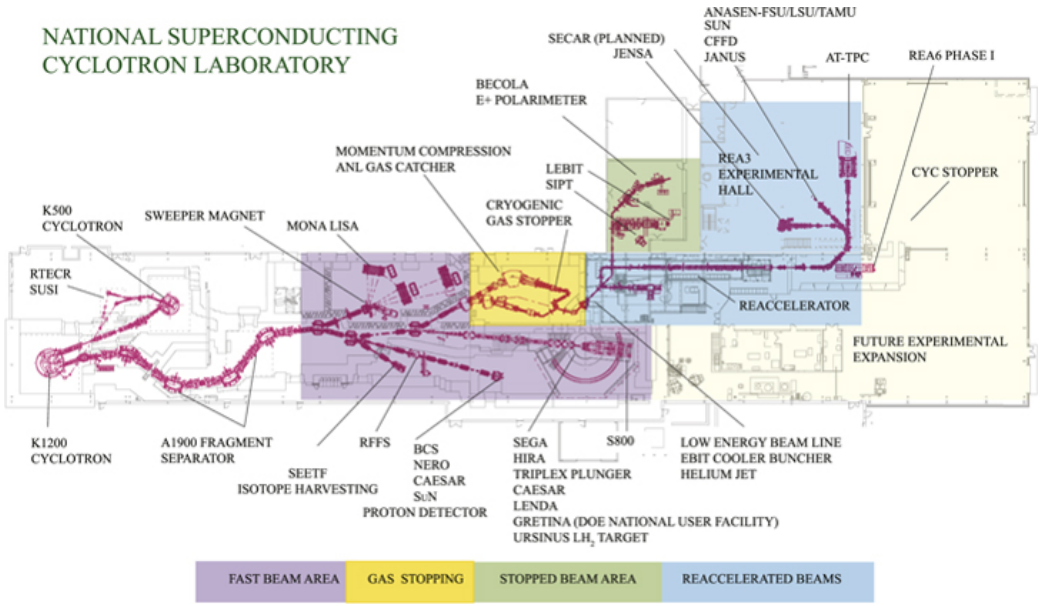


Figure 3.8: Illustration of the NSCL beam-line, with different regions labelled. The beam for this experiment is produced by a room temperature ECR (RTECR) and superconducting ECR ion source (SuSI) and accelerated sequentially by the K500 and K1200 cyclotrons. The beam is then separated by the A1900 fragment separator, stopped and re-accelerated by ReA3, and is delivered to the AT-TPC in the ReA3 experimental hall.

### 3.4.2 ReA3 Accelerator

As mentioned earlier, the secondary beam exiting the A1900 can be very energetic (∼50-140 MeV/u). In order to reach the energy desired for this experiment (4.5 MeV/u), the beam needs to be slowed down. One way of doing this is by using a degrader. The disadvantages of using a degrader are that this will decrease the intensity and the momentum dispersion of the beam in the transverse direction. This will result in a loss of energy and angular

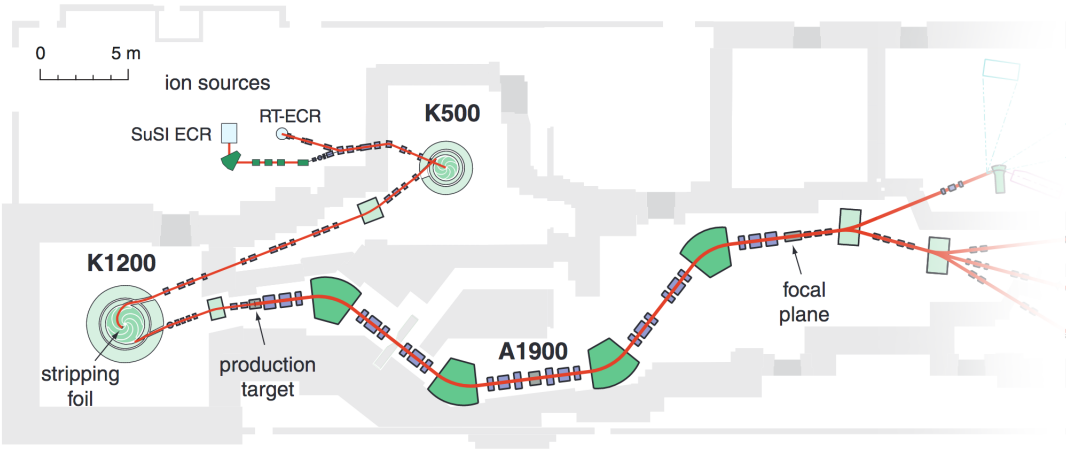


Figure 3.9: A1900 fragment separator in conjunction with the twin cyclotrons

resolution. The ReA3 facility eliminates the disadvantages of using a degrader by stopping the beam and re-accelerating it, however there will be a loss of beam intensity.

For this experiment, the beam that entered the ReA3 facility [71] is stopped in a linear gas stopper filled with helium gas. The thermalized $1^+$ ions are then cooled, accelerated (to ~30kV) from the gas stopper and transported using electromagnetic elements into an electron beam ion trap (EBIT). The ions in the trap are traversed by a high intensity electron beam for a few milliseconds and undergo electron impact ionization, increasing the charge of the ions for re-acceleration. They are then ejected and transported to a Q/A separator for charge selection. After this they are injected into the linear accelerator to reach a final energy of 4.5 MeV/u for this experiment.

$^{46}$K is an unstable isotope with a half-life of 105 seconds. During the time it takes for the secondary beam to be delivered, some of the $^{46}$K can beta decay into $^{46}$Ca. There is a dipole magnetic along the beam line from the gas cell to the EBIT that can separate contaminants from the beam, but it doesn't have a sufficient resolution to separate isobars. Fortunately the fusion cross-section for $^{46}$Ca + $^{208}$Pb is orders of magnitude lower than that of the studied system. The impurities can also be corrected for in the total cross-section

calculation. Particles with the same velocity and mass but a different number of protons will have different track lengths in the inner volume gas of the AT-TPC as it follows from the Bethe-Bloch formula. As a result it is possible to calculate the percentage of impurity in the beam based on track length of the incoming beam and subtract it from the total number of incoming beam particles. This will also be investigated in further detail in Section 3.6.3.

### 3.4.3 Characteristics of the Reaction Projectiles

Two beams, $^{46}$K and $^{19}$F, were separately delivered to the AT-TPC during this experiment; the $^{46}$K beam was delivered first for a total of 6 days and the $^{19}$F beam was delivered after for 24 hours. The $^{46}$K + $^{208}$Pb reaction was the primary focus of this study, the total fission cross-section and elastic scattering cross-sections had not been previously measured. Since the $^{19}$F + $^{208}$Pb reaction is a well studied system [72], the experimental data in this experiment was compared to this previous data in order to validate the analysis procedures. The energy of the $^{46}$K and $^{19}$F beams incident on the $^{208}$Pb target were 211.2 MeV and 107.4 MeV respectively, which was the maximum energy that could be achieved by the ReA3 accelerator. Both beams were delivered with a peak rate of about 1000 pps and a duty cycle, which is the fraction in which the beam is active over one period, of 5% and can be seen in Figure 3.10. For the $^{19}$F beam, the rate of the beam was chosen in order to limit event pileup. The rate of the $^{46}$K beam was limited by the production of the beam and the performance of the gas cell.

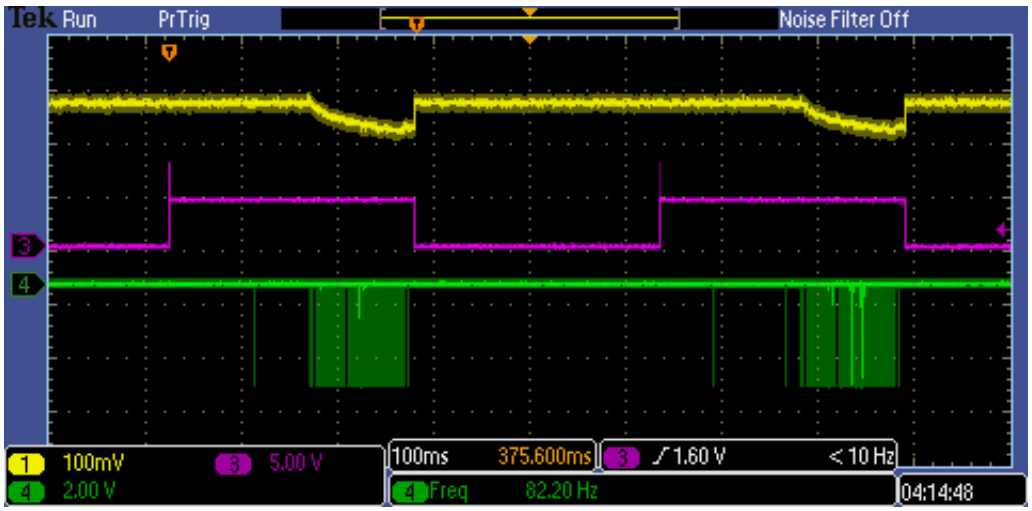


Figure 3.10: Oscilloscope trace of the $^{46}$K beam structure (green) delivered to the AT-TPC. The duty cycle of the beam is 5%.

### 3.4.4 Beam Identification

Both beams were identified using a ionization chamber located just upstream from the AT-TPC detector. During the data collection for the reaction studies, the ionization chamber was removed from the beam line in order to decrease the energy loss of the incoming particles and thus maximize the cross-section of the reaction. A schematic of the ionization chamber used can be seen in Figure 3.11. The ionization chamber was filled with 10 torr of isobutane gas, which was chosen for its high density of atoms. This pressure allowed for a sufficient signal to be achieved. The total thickness of the ionization chamber was $500\mu g/cm^2$.

### 3.4.5 Detector Gas

The inner volume of the AT-TPC detector was filled with 100 torr of P10 (10% methane, 90% Argon) gas. P10 gas was chosen as the ionizing gas due to the fast transport velocity of electrons at low electric field as well as the quenching ability of the methane. Fast electron transport in the AT-TPC will decrease the time between particle track creation and the

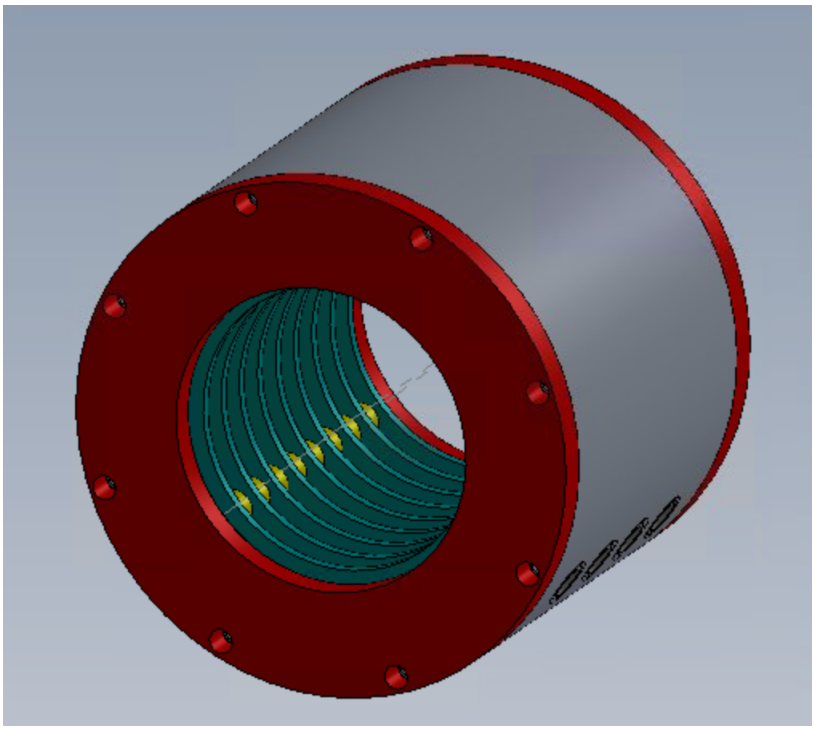

Figure 3.11: Drawing of ionization chamber used for beam identification. The ionization chamber was filled with 10 torr of isobutane which resulted in a total thickness of $500\mu g/cm^2$.

ionized electrons reaching the detector plane, decreasing the event pileup. Figure 3.12 shows the drift velocity of electrons in P10 gas. The drift velocity of the free electrons in this setup was approximately 6 cm/$\mu$s and as a result it will take 16.6 $\mu$s to travel the total length of the detector. The pressure of 100 torr was chosen in order to balance the ranges of the beams and of the fission fragments in order to easily distinguish between them. Using SRIM [73], the estimated ranges of the $^{46}$K and $^{19}$F beams in 100 torr of P10 gas are 70.8 cm and 110 cm respectively, while the estimated ranges of the fission fragments is 10-20 cm.

There was unexpected detector performance when using P10 gas in these conditions. A large amount of positive ion flow in the center of the detector due to the slow drift time of the positive ions resulted in recombination of electrons and ions. This led to a lack of signal or holes in tracks. This phenomenon is explained in more detail in the analysis section and in the publication by the AT-TPC group by Randhawaa et al [55].

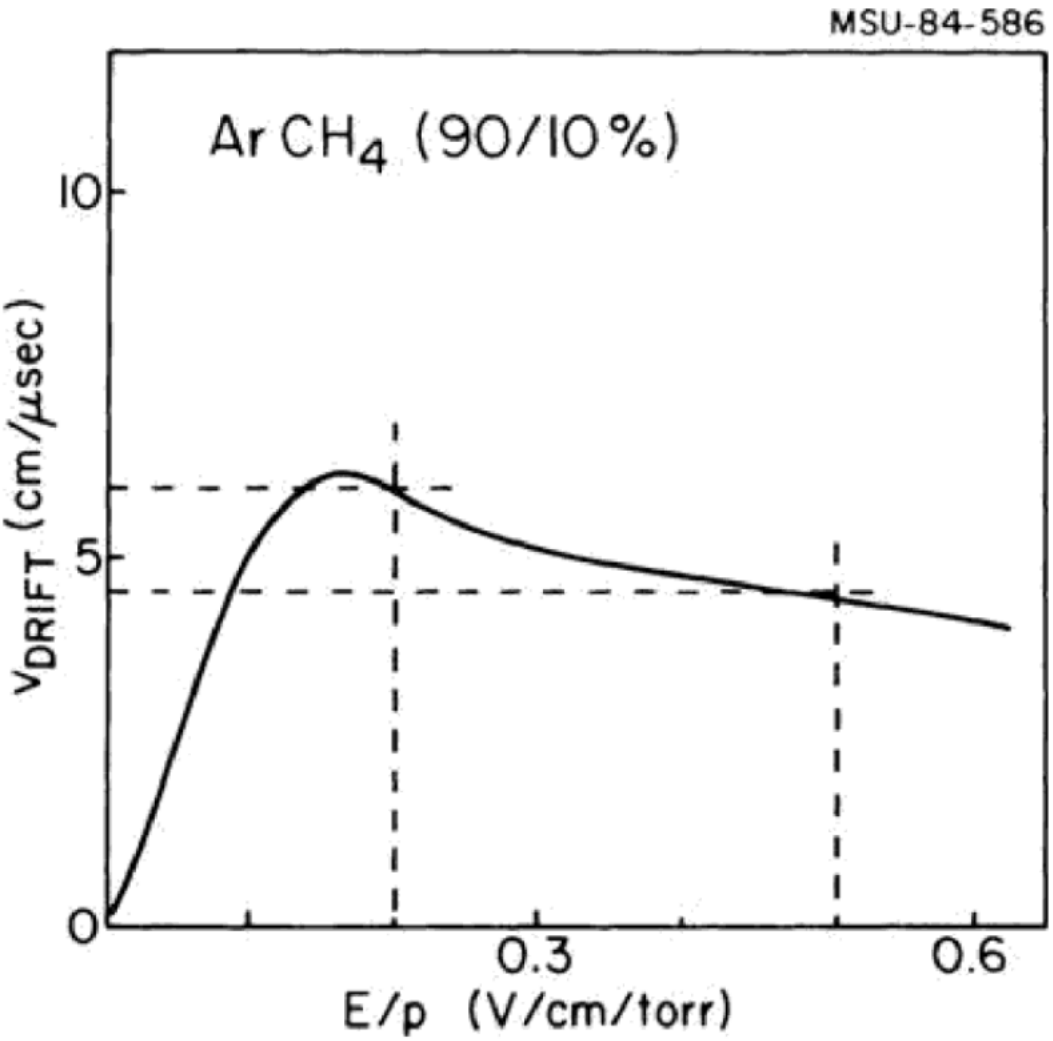


Figure 3.12: Drift velocity dependence on electric field for P10 gas [74].

### 3.4.6 Reaction Target and Window

The target for the fusion-fission experiment in this paper using the AT-TPC was $^{208}$Pb. Since there is no gaseous form of lead that exists at room temperature, a solid target was used. The lead was evaporated with a thickness of 0.635 mg/cm$^2$ onto a thin aluminized polypropylene foil . The foil, glued to an aluminum support, was placed inside the detector on the cathode and as close to the entrance window as possible. In order to minimize the energy loss through the entrance window of the detector (1cm diameter), the window material

needed to be as thin as possible while holding a pressure differential of at least 100 torr. A few materials were considered and tested as possibilities, including Mylar, polypropylene, and para-aramid(PPTA). Table 3.1 shows the variables considered, specifically maximum pressure differential and energy loss of a ∼5 MeV alpha particle. The energy loss of the alpha particle was used to estimate the energy loss of the incoming beam since dE/dx $\propto Z^2$. While the polypropylene had minimal energy loss of the alpha particle, the aluminized Mylar was chosen as the window material due to the slightly higher pressure differential. The window was glued to the window holder using AA-Bond F113 epoxy. This type of mounting results in a detection solid angle that is limited to $2\pi$.

| | Mylar | Polypropylene | PPTA (para-aramid) |
|---|---|---|---|
| Thickness | 0.9 um | 50 ug/cm2 | 6 um |
| Maximum Pressure (torr) | 330 | 300-310 | >760 |
| Energy Loss of Alpha Particle (keV) | 90 | 67 | 655 |

Table 3.1: Table of different window material considered for AT-TPC entrance window

### 3.4.7 Trigger

The two main triggers discussed in Section 3.3.7 were used in conjunction in this experiment. The trigger signal from the Micromegas mesh, or "beam trigger", was used to count the number of incoming beam particles and the SCA discriminator was set during the experiment to be just above the noise. The internal trigger from the GET electronics was set to a specific number of "hits" that did not include beam events. As a result, each CoBo was set to generate a signal if the number of channel triggers was above a lower level that was set just above threshold. The dead time of the DAQ (∼1ms, stemming from the electronics) and the rate of the beam need to be considered when setting the trigger thresholds. The product of the dead

time plus the trigger rate needs to be substantially smaller than the beam rate (1000pps).

## 3.5 Analyzing AT-TPC Data

The raw data taken by the AT-TPC DAQ consists of events with 10,240 trace signals corresponding to the pads on the pad plane. In this experiment, trace signals with no signal were suppressed by the DAQ. After amplification and shaping, each trace signal measures the amount of charge on each pad and is divided into 512 sequential segments of time called timebuckets. For this experiment, the write sampling rate of the SCA was 25MHz, which corresponds to 40ns/timebucket. Before an analysis can be conducted on data taken from the AT-TPC, the pertinent data needs to be extracted from these registered data, or "unpacked". The following section describes the unpacking progress.

### 3.5.1 Pedestal Subtraction and Charge Extraction

About 1000 traces of the 10,240 have an offset of the signal that is non-zero, which allows for information on variations of the zero offset and pulse undershoots. The zero offset is measured by averaging of the first 10 timebuckets in each trace signal and subtracting this average from the full trace. During the setup of the experiment, the signals produced by the incoming beam particles were centered within the 512 timebuckets. This is done by setting the value of the delay between the trigger signal and data stop writing signal. This time window will not only ensure that no information of the incoming particle is lost, but also guarantees that the first several timebuckets have only the pedestal information used for subtraction.

Once the pedestal has been subtracted, the charge collected by the pad and average

signal time is extracted. This can be done a number of ways, including taking the peak of the signal, the integral of the signal, or taking the center of gravity. In this experiment, the center of gravity of the signal was used. The maximum height of the signal is determined and then the signal a few timebuckets before and after the maximum are used in the weighted arithmetic mean

$$\bar{t} = \frac{\sum_{i=1}^{n} t_i a_i}{\sum_{i=1}^{n} a_i} \tag{3.4}$$

where the average timebucket $\bar{t}$ is weighted by the signal amplitude $a_i$ of each timebucket $t_i$. The average timebucket and corresponding signal height are then assigned to the pad number that each trace belongs to and will be used for track reconstruction.

### 3.5.2 3D Track Reconstruction - RANSAC

The information from the track of the incoming particle is represented by $(x_i, y_i)$ coordinates given by the centroid coordinates of the corresponding pad number, the time $t_i$ that the information was received by each pad in units of timebuckets, and the signal height $a_i$, which corresponds to the energy loss of the particle. The timing of the signal, in reference to the timing of the trigger signal, can be converted into a z-coordinate $z_i$ by measuring the drift velocity of the electrons in the active volume $v_d$ and using the ADC clock frequency $\nu$ in the equation

$$z_i = \frac{v_d t_i}{\nu} \tag{3.5}$$

After this process, there is a sufficient amount of information to reconstruct the track of the particle in 3 dimensions. There are number of approaches for track reconstruction utilized in the AT-TPC analysis; in this analysis the approach used is called RANdom

SAmple Consensus (RANSAC).

RANSAC is a mathematical algorithm that estimates the parameters of a mathematical function, in this case a 3D line. An iterative method is used to separate in a data set the inliers, which are the particle tracks, and outliers, such as noise from the detector. An illustration of RANSAC can be found in Figure 3.13.

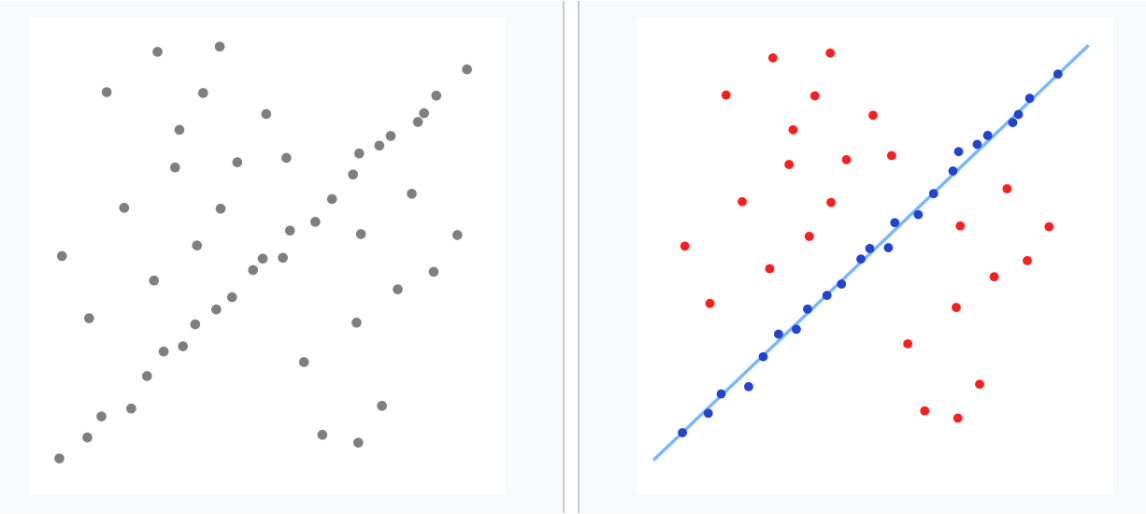

Figure 3.13: Left: A data set of 2D points that can be used as input for the RANSAC algorithm. Right: Output of the RANSAC algorithm. The blue line is the estimate that RANSAC found to be reasonably good. The blue points are part of the consensus set or inliers. The red points are outliers.

The process RANSAC used in the AT-TPC analysis is comprised of two steps that are then iteratively repeated. The first step is a random selection of two data points in the event and the construction of a 3D line with corresponding parameters. The second step involves checking the remaining data points to see if they are compatible with the constructed line within a chosen deviation. The data points that are considered compatible are called the consensus set. This process repeats with two outcomes: an estimate is rejected with too few points in the consensus set, or it is saved with a corresponding consensus set size larger than the previously saved estimate. Once a reasonably good estimate is established, then

the estimate is re-evaluated using all the data points in the consensus set [75]. Once the estimate is re-evaluated, all points in the consensus set are removed from the event data and the process is repeated.

In the AT-TPC analysis there are three main adjustable parameters that are set for RANSAC analysis: 1) the deviation in 3-D of a data point from an estimated model, 2) the number of data points in the consensus set for a line to be considered good, and 3) the deviation from one estimate to another [76]. This last parameter is important due to the chance that multiple tracks can occur within an event at the same time. The parameter needs to be tuned such that the deviation is small enough as to not reject multiple tracks, but also large enough not to double count single particle tracks.

The RANSAC algorithm outputs the number of tracks in an event and the respective data points that belong to each track. From this output, the approximate range of the tracks can be calculated by finding the distance between the first and last data points and the approximate charge can be calculated by summing the signal heights of all inlier data points. The total charge is proportional to the energy loss of the particle in the inner volume gas and can be compared to known energy loss profiles, such as the energy loss of beam particles.

## 3.6 AT-TPC Fission Analysis

### 3.6.1 Identifying Fission Fragments

Described here is the first experiment observing heavy-ion fusion fission reactions using the AT-TPC. There was no precedent analysis for fission fragment identification. As a first approach, before the experiment, a $^{252}$Cf spontaneous fission source was placed inside the

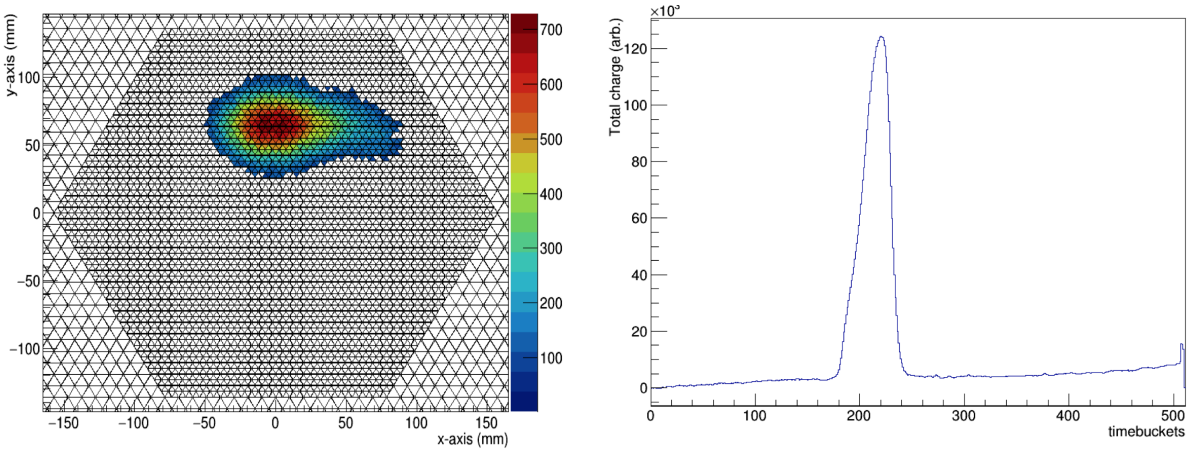


Figure 3.14: Left: X-Y projection of charge on the pad plane from a spontaneous fission event. Right: Total charge as a function of time from a spontaneous fission event

detector on the cathode near the entrance window. The data taken from these observed spontaneous fission events were used as a starting point for the identification of fusion-fission fragments for the beam induced fission. Figure 3.14 shows plots of a fission event from the spontaneous fission source. The left plot shows the 2D pad plane and the colors represent the total charge [arb. units] seen by each pad. The right plot shows the summed charge of each pad as a function of timebucket and is proportional to the energy loss profile of the particle. When looking at the energy loss profile from a spontaneous fission fragment calculated using TRIM, like in Figure 3.15, it can be seen that only the peak of the Bragg curve of the particle will be experimentally observed. When comparing the experimental energy loss profile in Figure 3.14 and the calculated energy loss profile from TRIM in Figure 3.15, the two plots are qualitatively consistent. This can also be visualized on the pad plane in Figure 3.14 (left), where it is observed that a high amount of energy is deposited at the beginning of the track (0,60) and subsequently decreases sharply.

As a result, these two plots in Figure 3.14 became essential in identifying fission fragments in the $^{46}$K + $^{208}$Pb experiment. Figure 3.16 shows the same plots from the this experiment.

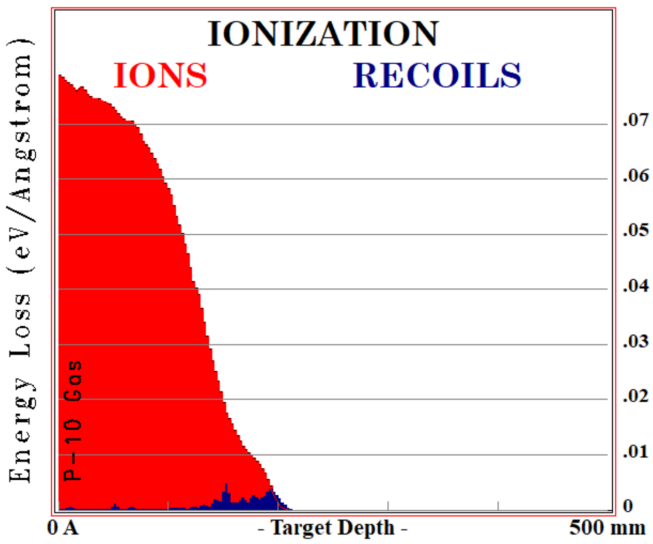


Figure 3.15: TRIM calculation of the energy loss profile of a typical $^{252}$Cf fission fragment with 100 MeV in P-10 at 100 torr.

When comparing the experimental fission event to the spontaneous fission event and to TRIM, they are qualitatively consistent, confirming that these were fission fragments.

There were three major observables used in identifying heavy-ion fission fragments in the primary experiment: 1) total range, 2) total charge, and 3) origin of the particle track. As discussed earlier in Section 3.4.5, the ranges and energy of the beam and fission fragments are significantly distinct from one another. Since the detector was tilted, any fission events from the $^{208}$Pb target will originate from the center of the pad plane (0,0) since the target was placed at the central beam entrance. Any scattering events that occur in the gas will originate further away from (0,0) the farther the beam particle progresses through the detector before reacting.

### 3.6.2 Elastic Scattering Normalization

The elastic scattering of $^{19}$F + $^{208}$Pb was analyzed in order to normalize the fission cross sections. Since the range of the $^{19}$F particles in the detector is ~90cm, the observed range of

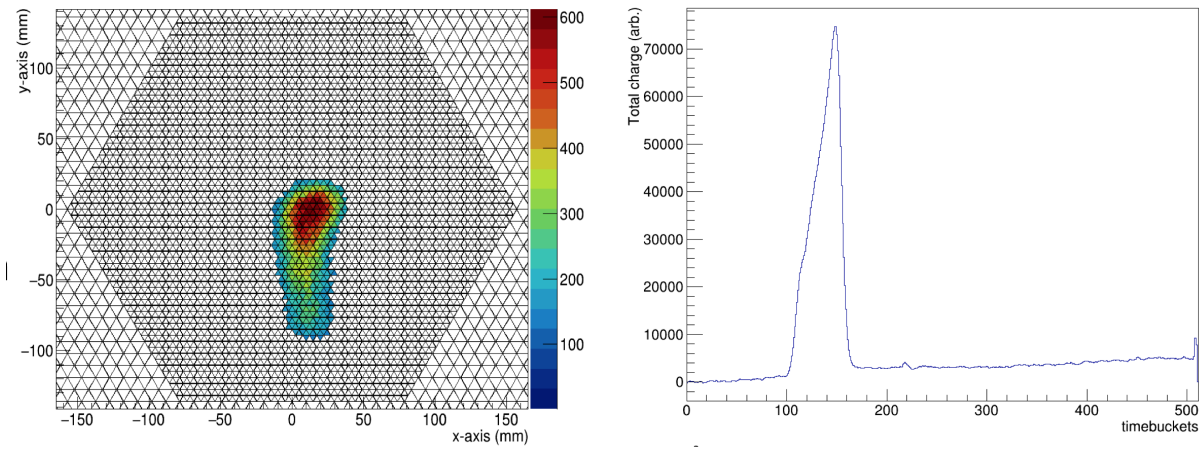


Figure 3.16: Left: X-Y projection of charge on the pad plane from an event of the primary experiment. Right: Total charge as a function of time from an event of the primary experiment. Note that the direction of the x-axis is opposite to that of Figure 3.15.

the elastically scattered particles will be constrained to the geometry of the detector. Figure 3.17 shows both the range and summed total charge as a function of lab angle for all events with a single particle track for all $^{19}$F + $^{208}$Pb runs. The summed total charge plot (left) shows a clear restriction of energy as a function of lab angle from 30° to 90°. A visual cut on the data (shown in red) results in events with ranges that are in agreement with the geometry of the detector (represented as black curve).

The elastically scattered differential cross sections in the lab frame are calculated by

$$\left.\frac{d\sigma(\theta,\phi)}{d\Omega}\right|_{lab} = \frac{1}{nt\Delta\Omega}\frac{N_{scat}}{N_{inc}} \tag{3.6}$$

where $n$ is the number density of the target, $t$ is the target thickness, $\Delta\Omega$ is the finite angular range, and $N_{scat}$ and $N_{inc}$ are the number of scattered and incoming particles respectively. They are then transformed into the center-of-mass frame by

$$\left.\frac{d\sigma(\theta,\phi)}{d\Omega}\right|_{cm} = \left.\frac{d\sigma(\theta,\phi)}{d\Omega}\right|_{lab}\frac{sin\theta_{lab}}{sin\theta_{cm}}\frac{d\Omega_{lab}}{d\Omega_{cm}} \tag{3.7}$$

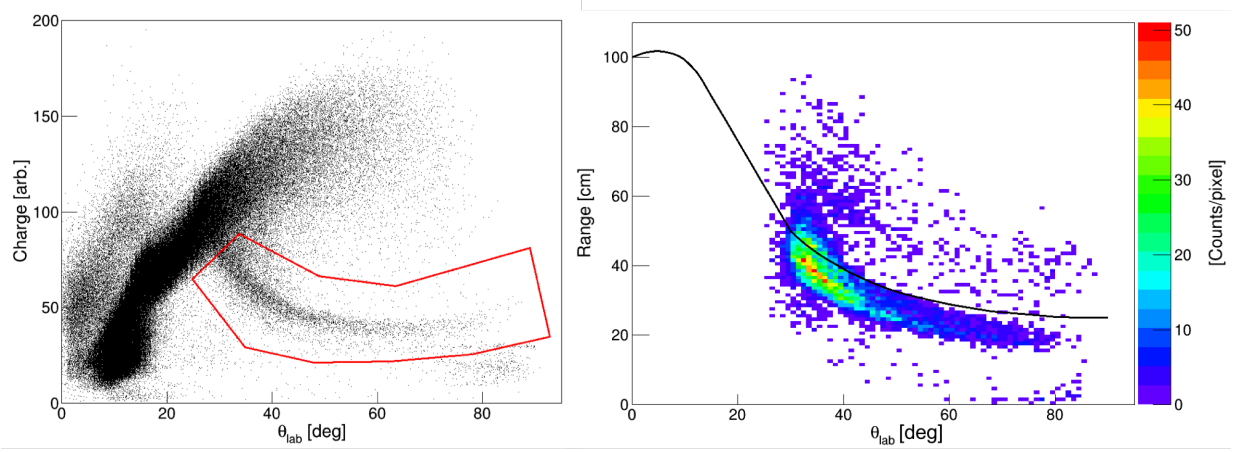


Figure 3.17: Left: Total charge of single particle events measured in the AT-TPC as a function of angle. A visual cut (solid red) is made on beam particles elastically scattered off of the $^{208}$Pb target. Right: Ranges of single particles events measured in the AT-TPC after visual cut. The black curve is the maximum ranges the AT-TPC can measure for events originating from the window.

where $\frac{d\Omega_{lab}}{d\Omega_{cm}}$ is the Jacobian and is calculated using LISE++. The elastic differential cross sections were then normalized to the Rutherford cross sections given by

$$\left.\frac{d\sigma(\theta,\phi)}{d\Omega}\right|_{Ruth} = \left(\frac{Z_1 Z_2 e^2}{4\pi\epsilon_0}\frac{1}{4KE}\right)^2 \frac{1}{sin^4(\theta/2)} \tag{3.8}$$

The elastic scattering cross sections were then compared to cross sections calculated using the Sao Paulo optical potential and is shown in Figure 3.18. The cross sections in the region between 50° and 70° were found to be in good agreement; at more forward angles there is an increasing background from elastic scattering on the gas (Figure 3.17). As a result, no further renormalization needed to be applied to the experimental fission data.

### 3.6.3 Beam Impurity

As mentioned in Section 3.4.2, the $^{46}$K beam is a radioactive beam that can decay with its characteristic lifetime. Also the ReA3 beamline between the gas cell and the EBIT has a

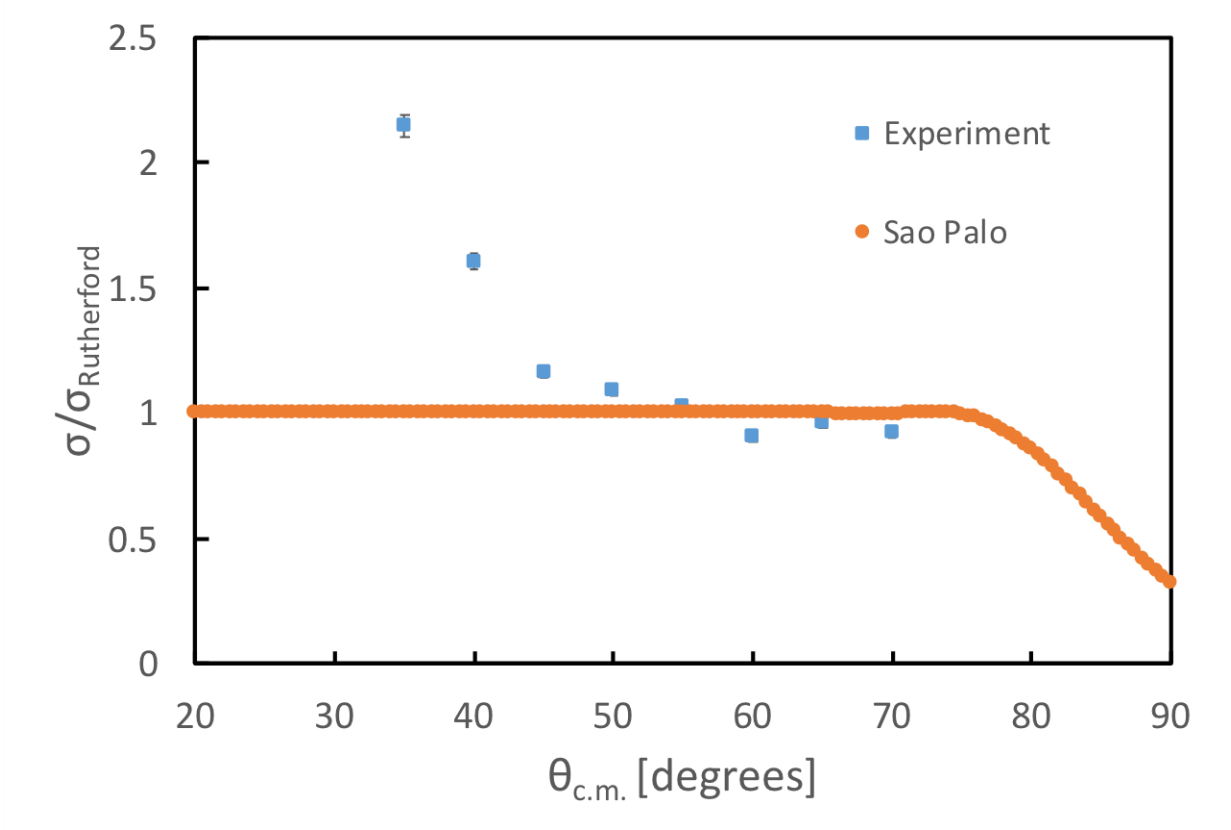


Figure 3.18: Measured (blue square) and optical model (gold circle) elastic scattering cross sections reduced by Rutherford scattering cross sections

magnetic rigidity of only $\sim 1\%$, which is not sufficient enough to separate isobars. Therefore the incoming beam is not 100% pure and this implies corrections to cross section calculation. To assess the purity of the incoming beam, the ranges of single particle events at 0° in the detector was plotted for each run and can be found in Figure 3.19. Although all incoming isobar particles have the same velocity and therefore energy, the energy loss in the detector gas will depend on Z. This results in different ranges in the gas where the $^{46}$K beam can be identified. It can be seen in Run 228, at the beginning of the experiment, that three different species of beams are present. The large peak at 65cm is consistent with the range of $^{46}$K and the secondary peak at 75cm is consistent with the primary decay of $^{46}$K, $^{46}$Ca. The tertiary peak at 85cm is consistent with $^{48}$Ti. As the experiment progresses, the percentage

of beam impurities decreases and reaches a constant impurity of 10%. The cause of this decrease could have stemmed from the implementation of a beam cleaning method used by the operators of ReA3 [77].

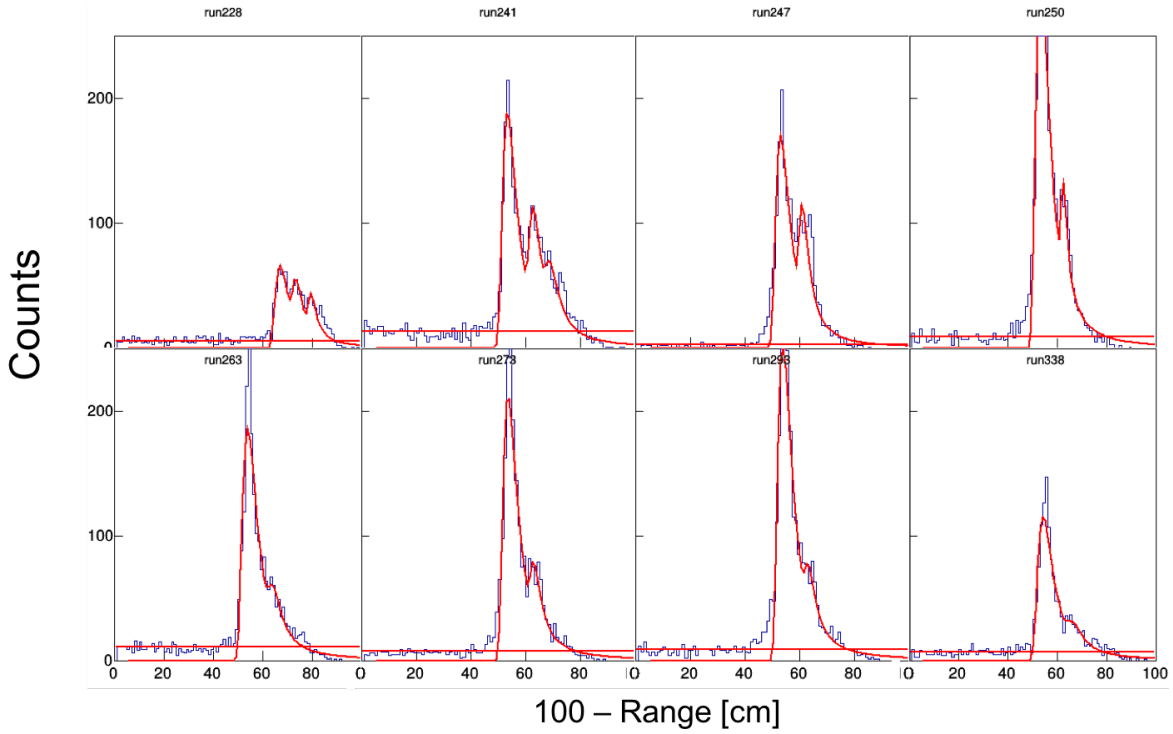


Figure 3.19: Ranges of single particle events in the AT-TPC at 0°. Each run (left to right) is further along in experiment time. Each peak was fitted with a separate Landau curve (solid red line) and summed. X-axis was inverted in order to fit with Landau curves.

The corresponding peaks were fitted with Landau functions. The integrals of the peaks and percentage of impurities were calculated for each run and are shown as a function of experimental run time in Figure 3.20. Each run was one hour in duration, and the number of incoming particles per run was found to be relatively constant. Since the total number of incoming beam particles was approximately constant for each run, a total beam impurity of 12% was calculated by fitting two linear equations to the data, one to the large slope between 0-20 hours and a second to the nearly constant percentage of impurity between 20-85 hours, and integrating.

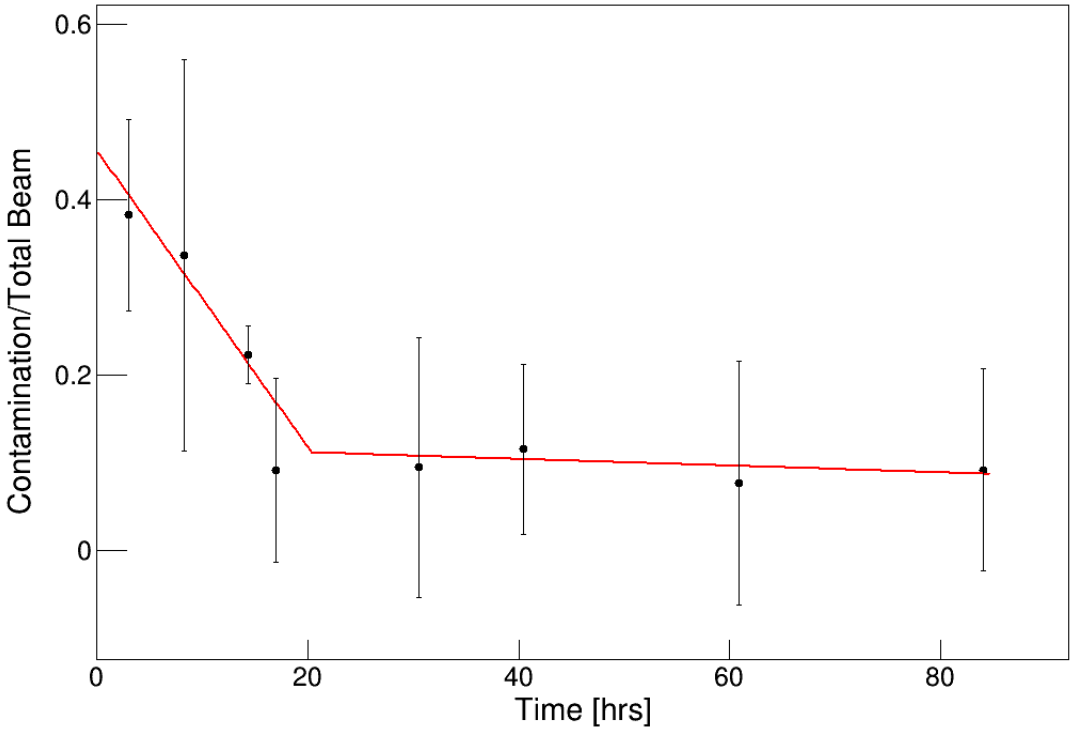


Figure 3.20: Percentage of beam impurities over the duration of the $^{46}$K + $^{208}$Pb experiment. The most likely impurities are the primary decay of the beam, $^{46}$Ca.

### 3.6.4 Differential Cross Section

The measured differential cross section of fission fragments for both the $^{19}$F + $^{208}$Pb and $^{46}$K + $^{208}$Pb reactions were determined using Equations 3.6 and 3.7.

In order to obtain total capture cross sections from these measured differential cross sections, the regions beyond the detector's angular coverage need to be extrapolated. The method used in this analysis is the transition state model. The saddle point transition model (SPTS) [78] estimates the anisotropy, the ratio of fissioning events at 180° to 90°, as

$$\frac{< W(180°) >}{< W(90°) >} \approx 1 + \frac{< I^2 >}{4K_0^2} \tag{3.9}$$

where $< I^2 >$ is the magnitude of the total angular momentum of the fissioning nucleus

and $K_0$ is the standard deviation of an assumed Gaussian distribution of K states. Using a classical approximation, $< I^2 >$ is given by

$$< I^2 > \approx [\mu(E_{cm} - V_c)/\hbar^2](R_t + R_p)^2 \tag{3.10}$$

where $\mu$ is the reduced mass, $V_c$ is the Coulomb barrier, and $R_t, R_p$ are the radii of the target and projectile nucleus respectively. The quantity $K_0^2$ is related to the effective moment of inertia $\Im_{eff}$ and the nuclear temperature at the saddle point $T_{nuc}$ by

$$K_0^2 = \frac{\Im_{eff} T_{nuc}}{\hbar^2} \tag{3.11}$$

where the parallel and perpendicular moments of inertia are used to calculate the effective moment of inertia $\Im_{eff} = J_\parallel J_\perp/(J_\perp - J_\parallel)$. The nuclear temperature at saddle can be expressed as

$$T_{nuc} \approx \sqrt{(E^* - B_f - E_{rot} - E_\nu)/a_f} \tag{3.12}$$

where $B_f$ is the fission barrier and $a_f$ is the level density parameter. A typical value used for $a_f$ is $\sim \frac{A}{8}$. Additionally, angular distributions $W(\theta)$ are commonly fitted with a series of Legendre polynomials

$$W(\theta) = \sum_n c_n P_{2n}(cos\theta) \tag{3.13}$$

where only even Legendre polynomials $P_{2n}$ are included to conserve forward and backward symmetry [78].

Equations 3.9 and 3.13 can be used to estimate the anisotropy of the the system and

predict the full differential cross sections. Figure 3.21 shows that this method (yellow) is in good agreement with the calculated cross sections of the $^{19}$F + $^{208}$Pb reaction from the AT-TPC and from Kapoor et al. [79]. The full experimental capture cross section is calculated by multiplying by $2\pi \sin\theta$ and integrating the full curve and is found to be in good agreement within error with cross sections measured by B. B. Back et al [80] in Figure 3.22.

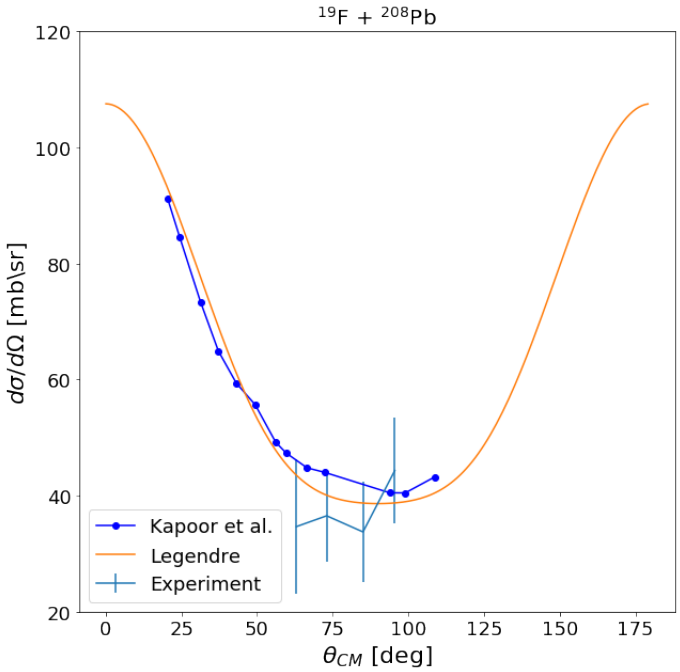


Figure 3.21: Differential cross sections of the $^{19}$F + $^{208}$Pb reaction measured by the AT-TPC as a function of center of mass energy ($E_{CM}$)and approximated cross sections from Legendre polynomials.

Since this method of total capture cross section determination is found to be in agreement with past experimental data, it is suitable to be used in cross section calculation for the $^{46}$K + $^{208}$Pb reaction and in future AT-TPC fusion-fission experiments. Figure 3.23 (left) shows the determined experimental cross sections for this reaction with the aforementioned method using an approximate anisotropy and angular distribution using Legendre polynomials. The total capture cross section is shown in Figure 3.23 (right) as a reduced cross section in comparison with the $^{39}$K + $^{208}$Pb reaction discussed in Chapter 6.

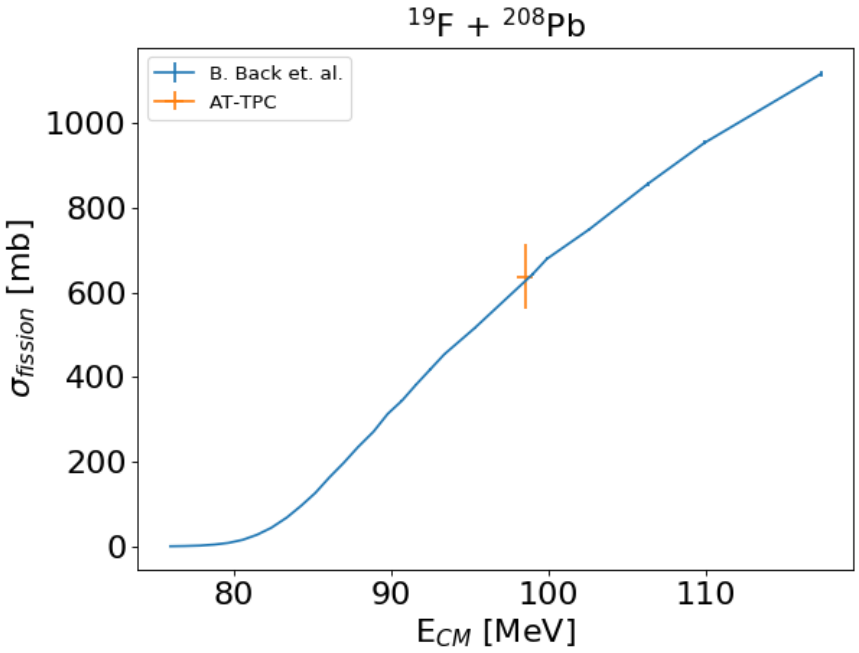


Figure 3.22: Fission cross section for the $^{19}$F + $^{208}$Pb reaction measured by the AT-TPC as a function of center of mass energy ($E_{CM}$) compared to previous measurements [80].

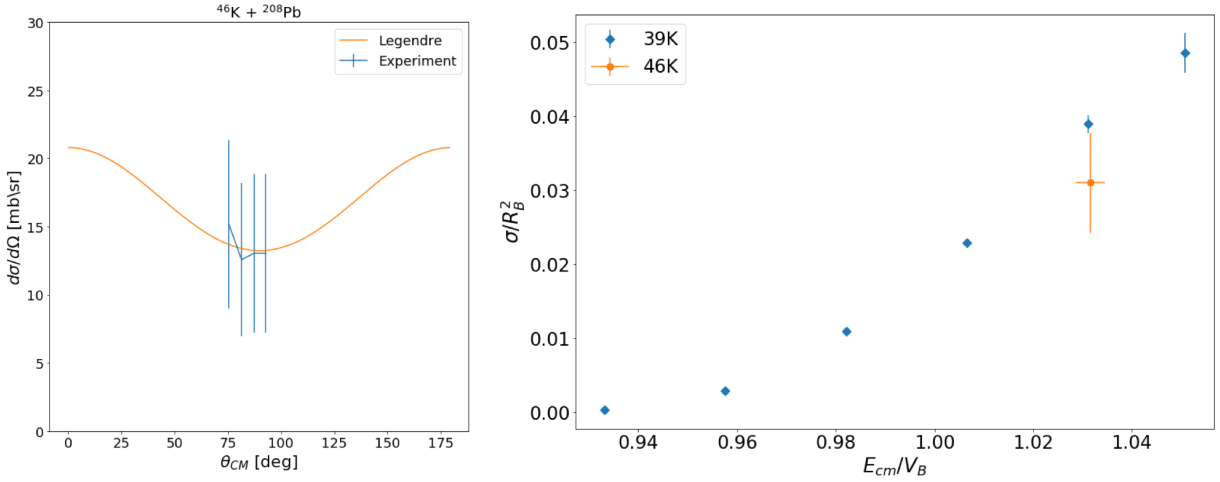


Figure 3.23: Left: Differential cross sections measured by the AT-TPC as a function of center of mass angle ($\theta_{CM}$) and approximated cross sections from Legendre polynomials. Right: Reduced capture cross sections for $^{39,46}$K + $^{208}$Pb reactions

# Chapter 4

# Measurement of Fission Fragment Tracks

The identification of fission fragment tracks is an important step in utilizing the AT-TPC as a fission fragment detector. It would allow for the distinguishing of fusion-fission and quasi-fission events, since quasi-fission events have Z distributions similar to the Z of the beam and target compared to fusion-fission Z distributions, as well as fusion-evaporation events during analysis and provide a more detailed picture of the fusion process. The AT-TPC and pAT-TPC have energy resolutions of ∼2-5%, suggesting that it could be possible to distinguish the Z value of the fusion products. The range of the stopped particles can be determined with a precision of the order of 1mm. The following chapter discusses experiments using the pAT-TPC measuring fission fragments from a spontaneous fission source and the analysis to identify these fragments based on energy loss and range.

## 4.1 Experimental Setup

A 1$\mu$Ci $^{252}$Cf spontaneous fission source was placed inside the pAT-TPC in the center region of the cathode near the entrance window (Figure 4.1); the fission fragment energies are expected to range from 70-110 MeV and light fragments are expected to vary from Kr to Ru. Two separate ionization gases, pure hydrogen ($H_2$) and He-$CO_2$ (90:10) were chosen to

measure fission fragments due to their low ionization energies. The low ionization energies as compared to the total energies will produce a large number of electron-ion pairs generated by the fragments and result in large signals generated in the electronics. SRIM was used to determine the pressure of the gases with the restriction that projected range of the light fragments could not exceed the length of the detector (50cm), with pressures of 400 torr for pure $H_2$ and 300 torr for He-$CO_2$.

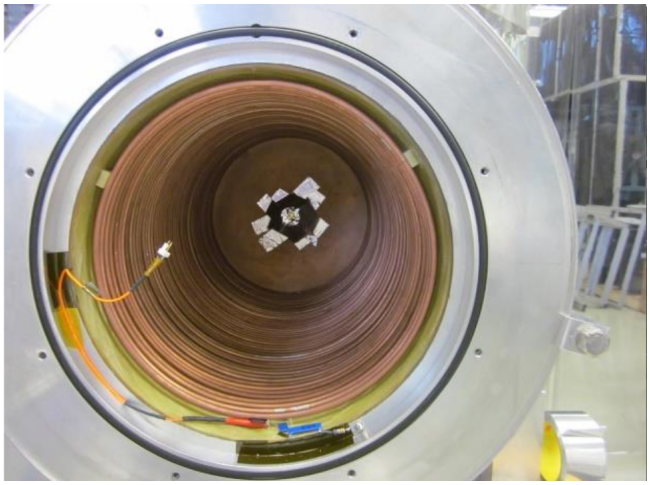

Figure 4.1: Picture of the opened pAT-TPC with the $^{252}$Cf source attached to the center of the cathode.

Micromegas alone and Micromegas+Thick Gaseous Electron Multipliers (ThGEMs) were used. ThGEMs are robust high gain electron multipliers that are constituted of a double faced Cu-clad printed circuit board perforated with millimeter to sub-millimeter diameter holes. An electric potential is applied between the faces generating a strong dipole electric field, resulting in gas avalanche multiplication of incident electrons. An illustration of the generated ThGEM electric field can be found in Figure 4.2 and a more complete description of ThGEMs can be found by A. Breskin and M. Cortesi, et al [81, 82]. Suitable voltages for these electron amplifiers were ∼300V for the Micromegas and 100V for the ThGEMs with a cathode voltage of 20kV.

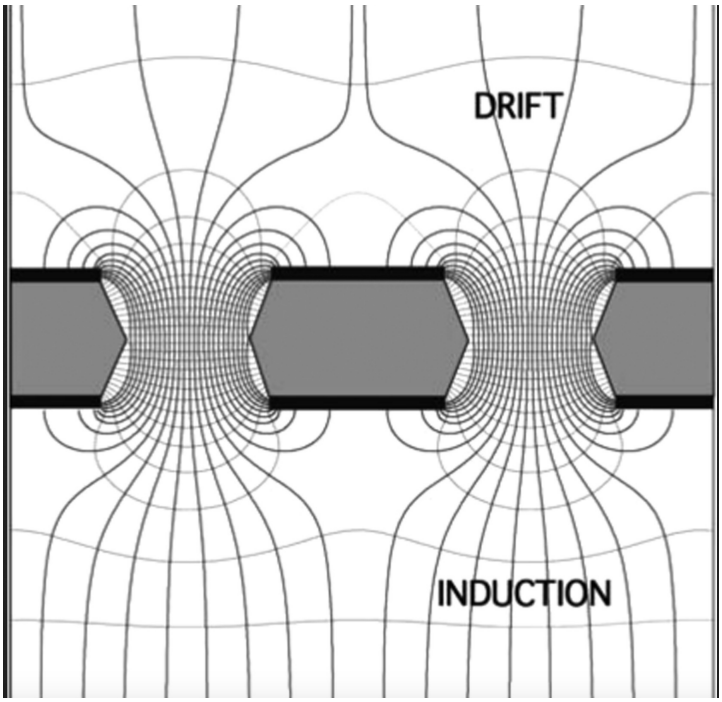


Figure 4.2: Illustration of the electric fields inside the holes of a ThGEM during operation [83]. An electric potential is applied between the faces, generating a strong dipole electric field inside the holes, depicted by the large concentration of electric field lines.

Events were selected using the Micromegas mesh trigger signal discussed in Section 3.3.7. Since the only charged particles from the spontaneous fission source are 6.1 MeV alpha particles and 70-110 MeV fission fragments, it is simple to distinguish between the two from signal amplitude. An example of a selected fission event is shown in Figure 4.3. The amplitude and shape closely resemble that of fission events measured in the AT-TPC (Figure 3.14).

## 4.2 Analysis

The range of the track was determined by the first and last timebucket ($Tb_i$) of the fission fragment signal by

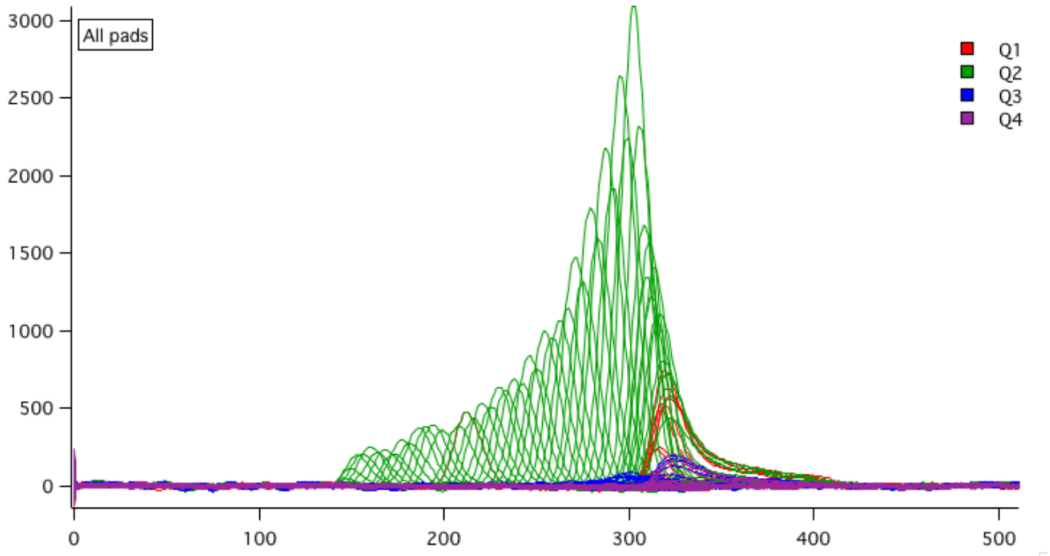


Figure 4.3: Pad signals from a fission fragment measured by the pAT-TPC. Each color is representative of one of the four quadrants into which the pad plane is separated.

$$r = \frac{v_d \nu^{-1}(Tb_f - Tb_l)}{cos\phi} \tag{4.1}$$

where $\nu$ is the ADC clock frequency, $v_d$ is the drift velocity, and $\phi$ is the angle between the track and the vertical axis (parallel to the pad plane). The drift velocity was measured using a gamma-ray detector (measuring gamma-rays from the spontaneous source) outside the downstream end of the pAT-TPC and the mesh signal from the Micromegas in coincidence. Figure 4.4 shows the oscilloscope readout of the gamma-ray detector signals (yellow) in coincidence with the mesh signals (blue). The measured drift velocities for $H_2$ and He-$CO_2$ using this method were 1.0 and 2.5 cm/$\mu$s respectively.

Energy loss calibration is performed with the 6.1 MeV alpha (81.5%) emitted from the $^{252}$Cf nucleus. Using SRIM, the energy loss profile of the particle through the detector gas can be estimated and used to calibrate experimental tracks.

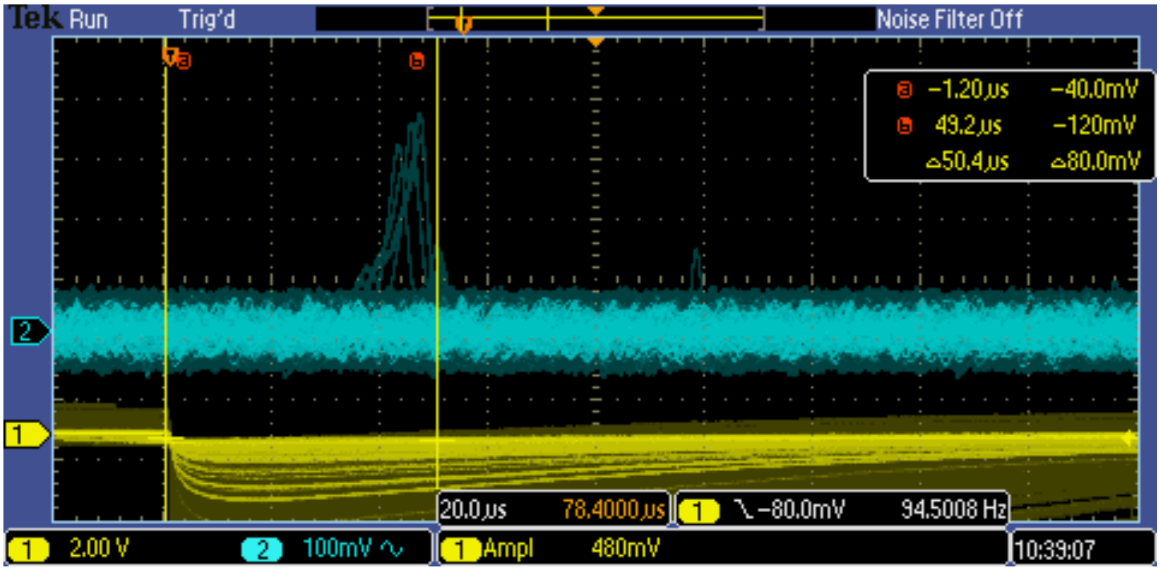


Figure 4.4: Oscilloscope view of the signal from the gamma-ray detector (yellow) in coincidence with the mesh signal of the fission fragments from the pAT-TPC (blue).

### 4.2.1 Comparison to SRIM

In order to identify fission fragments with specific Z, the energy loss profiles of the fission fragments were collated with an energy loss profile of an expected fission fragment from SRIM. For this experiment, the energy loss profile of a $^{102}$Ru fragment at 100 MeV calculated by SRIM was used as a standard for comparison. The energy loss curve was fitted with a high order exponential (Figure 4.5a) giving a continuous curve of energy loss as a function of energy. This was used to calculate the energy loss in 1mm steps (Figure 4.5b), using the equation

$$E_2 = E_1 - \frac{dE}{dx} * 1mm. \tag{4.2}$$

Both experimental and calculated energy loss curves were normalized by dividing each curve by their respective areas and the ratio between the two curves was used to differentiate fragments. Figure 4.6 shows an example of this ratio with one experimentally measured

energy loss curve. The ratio between experimental and calculated energy loss curves will be analysed.

Figure 4.7a shows the energy loss ratios for fission fragments. Although there are not visible discrete bands, it is clear that there is separation in the energy loss curves, with the greatest separation at ∼50mm. A series of gates on range were applied to this plot and projected onto the Y-axis in order to differentiate between fragments. Figure 4.7b shows an example with a range gate of 45-55mm.

If the range $\Delta R/R$ and energy $\Delta E/E$ resolution of the order of ∼1-2% can be achieved in the p-ATTPC, it should be possible to determine the Z-value of individual particles. Figure 4.7b shows that this resolution is being approached. The Cf source makes it difficult to obtain quantitative information due to the broad ranges of A, Z, and kinetic energy that comes with spontaneous fission sources as well as the energy degradation of the fission fragments as they travel through the source. One solution is to conduct an experiment with a small accelerator that can provide beams with well determined A, Z, and energy.

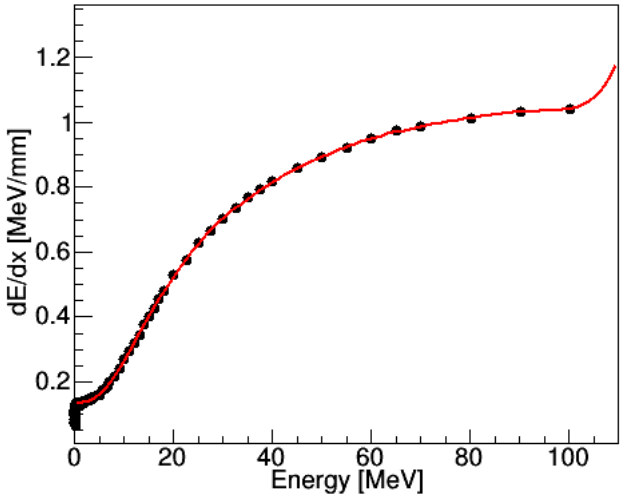


(a)

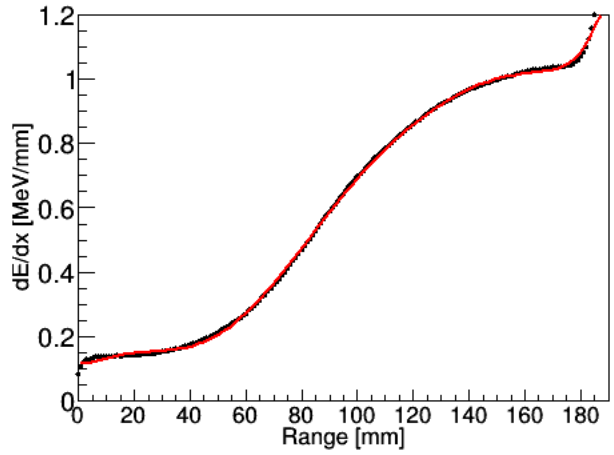


(b)

Figure 4.5: Left: Calculated energy loss of $^{102}$Ru at 100MeV as a function of energy fitted with a polynomial function. Right: Energy loss of $^{102}$Ru as a function of range interpolated from the polynomial fit from (a).

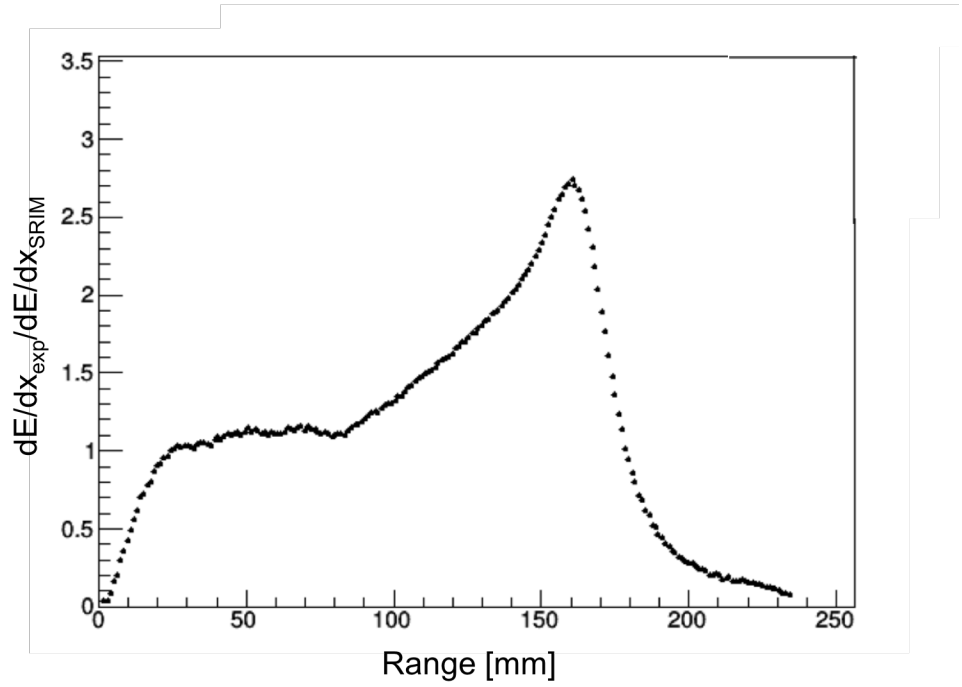


Figure 4.6: Ratio of experimentally measured energy loss curve of a fission fragment with the calculated energy loss curve (SRIM) of $^{102}$Ru at 100MeV.

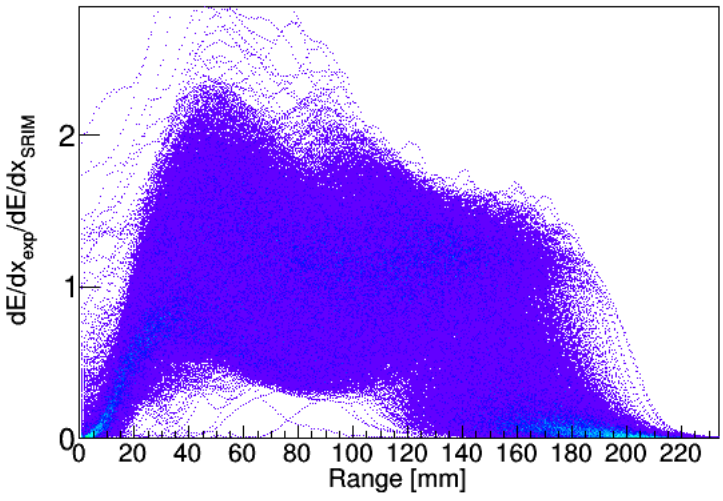


(a)

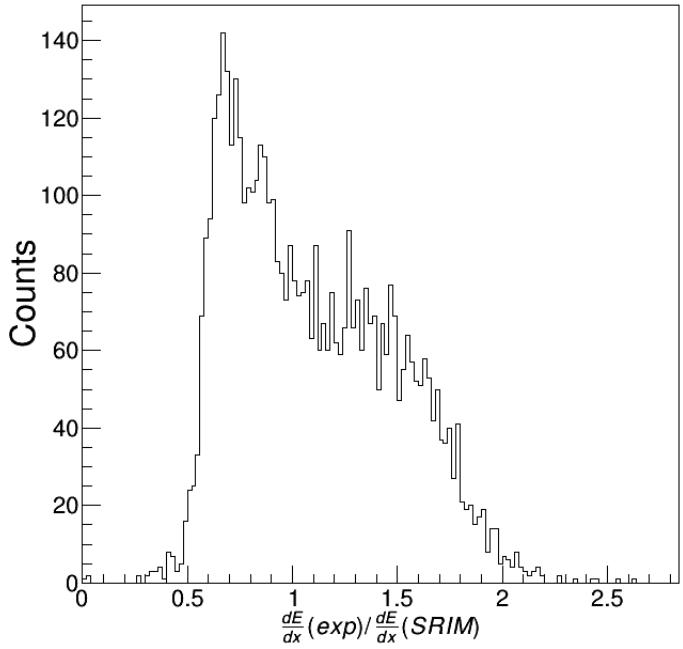


(b)

Figure 4.7: Left: Ratio of experimental and calculated (SRIM) energy loss curves of fission fragments. Right: Y-projected data of (a) between the ranges of 45-55cm

# Chapter 5

# Australian National University

The motivation of the experiments detailed in this dissertation was to study the possibility of enhancements of heavy-ion fusion-fission cross sections for more neutron-rich beams in systems nearby to the $^{32,38}$S + $^{208}$Pb reaction. The $^{46}$K + $^{208}$Pb fusion-fission measurement with the AT-TPC determined the cross section for a neutron-rich reaction, however the measurement of a more stable beam fusion-fission reaction was needed to make a conclusion about possible cross section enhancements. Therefore the $^{39}$K + $^{208}$Pb fusion-fission excitation function was measured at Australian National University (ANU) with the use of the Nuclear Reaction Dynamics Group's CUBE detector. Another nearby system, $^{40,48}$Ca + $^{144}$Sm, was also chosen for fusion-fission excitation function measurement. This chapter details these experiments at ANU with the CUBE detector and the analysis techniques used to determine fusion-fission cross sections.

## 5.1 Heavy Ion Accelerator

Two complimentary experiments were performed at the Australian National University (ANU) Heavy Ion Accelerator Facility using the 14UD tandem accelerator. The 14UD is a National Electrostatics Corporation Pelletron accelerator that uses an electric field generated by an accelerating voltage $V_A$ of up to 15MV to accelerate particles for nuclear physics and applied experiments [84, 85].

Negative ions are produced using a SNICS (Source of Negative Ions by Caesium Sputtering)[86]. A Cs oven produces Cs vapour that is then introduced into an ion source chamber. These Cs atoms can become positively ionized when coming in contact with a hot ionizer. As a result, the positively charged Cs ions accelerate towards a water cooled cathode containing a solid sample of the desired beam species. Atoms and ions are sputtered out of the sample and gain a negative charge by collecting an electron from the layer of condensed neutral Cs atoms on the surface of the cathode. These negative $1^-$ ions are repelled by the cathode, refocused, and transported by a positively biased extractor electrode[87, 88]. Then the beam is accelerated and transported to a mass selection magnet.

The mass selection magnet consists of a dipole magnet that separates beam particles by momentum over charge. After this selection, the beam enters an accelerator tube located in the 14UD tank where it undergoes acceleration. The beam accelerates towards a positive high voltage terminal in the middle of the tank and then passes through a carbon stripping foil, which changes the beam from negatively charged to positively charged with a distribution of charge states ($Q^1+, 2+, .., Q = Z$)[89, 90]. The now positively charged beam accelerates away from the high voltage terminal and enters a 90 $^\circ$ energy selection magnet, where only a specific charge state is selected [91]. The final energy exiting the accelerator is $(1 + Q^+)V_A$. The beam can either be sent to a superconducting LINAC for further acceleration or directly to the experimental area. In these experiments, the beam bypassed the LINAC and went directly to the CUBE detector.

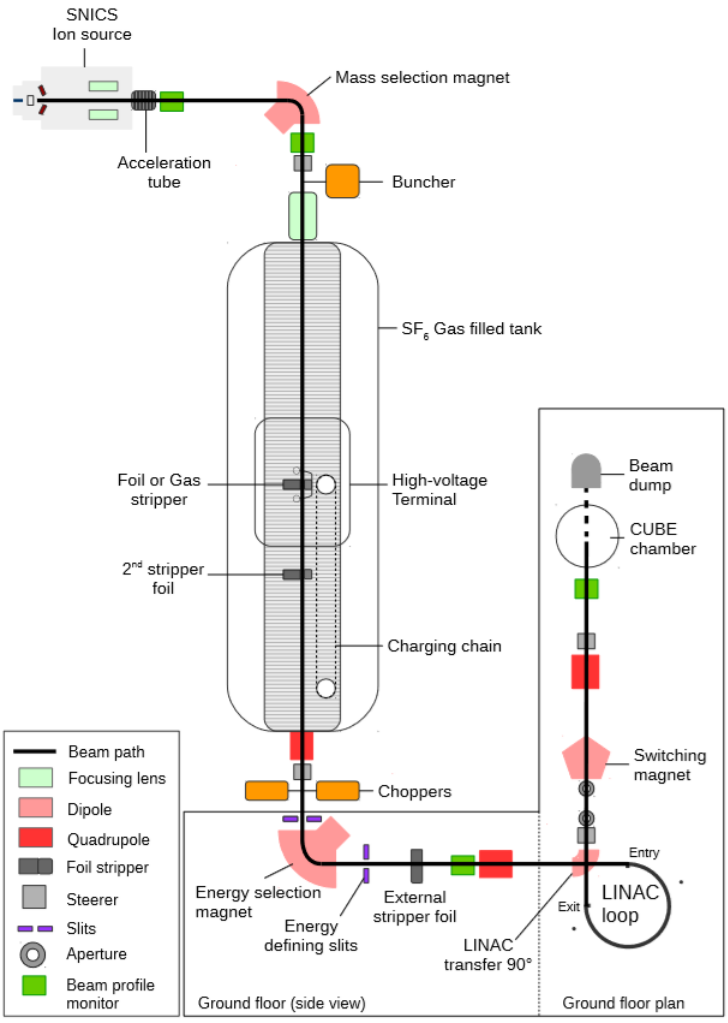


Figure 5.1: Schematic view of the ANU Heavy Ion Accerlator Facility beam line

## 5.2 Structure of CUBE Detector

The CUBE detector [92], operated by the reaction dynamics group located at the Australia National University, is a binary fission spectrometer that reconstructs fission events using the kinematical coincidence method [93]. It consists of both multi-wire proportional counters (MWPC) and silicon monitor detectors. Charged particles are detected by three MWPC's located at 45°, 90°, and 135°off the beam axis and at a distance of 180.0 - 195.0 mm. The MWPC's labelled "Front Det." and "Back Det." have a relatively large area of 279.0 mm x 357.0 mm. The MWPC labelled "Small back Det." covers roughly half the area as on of the first two. Figure 5.2 shows the angular coverage of the MWPC's. The MWPC's consists of horizontal and vertical anode wires sandwiching a cathode foil. The anode wires are $20\mu m$ Tungsten wires coated with gold spaced every 1mm. The cathode foil is a $0.9\mu m$ Mylar foil with a thin layer ($40\mu g/cm^{-2}$) of gold evaporated onto each side. The cathode foil is segmented (4 segments for the large detectors, 2 for the small) in order to decrease the capacitance and increase the pulse height of the signals.

The MWPC's are filled with propane gas at 4 Torr. As a charged particle passes through the detector, it ionizes the propane molecules and the resulting free electrons drift towards the nearest anode wire. The electrons produce an avalanche in the high electric field near the wires and generate a pulse that is delivered to a readout at the end of the wires. The crossed wire anodes were used to determine the (X,Y) position and allow for the precise measurement of the coordinates with a resolution down to 1mm (FWHM) [94, 95]. An illustration of a MWCP used in the CUBE detector can be found in Figure 5.3

The signal from the particle passing through the cathode and the signal from the pulsed beam RF are used to produce time of flight measurements of the beam. The charge collected

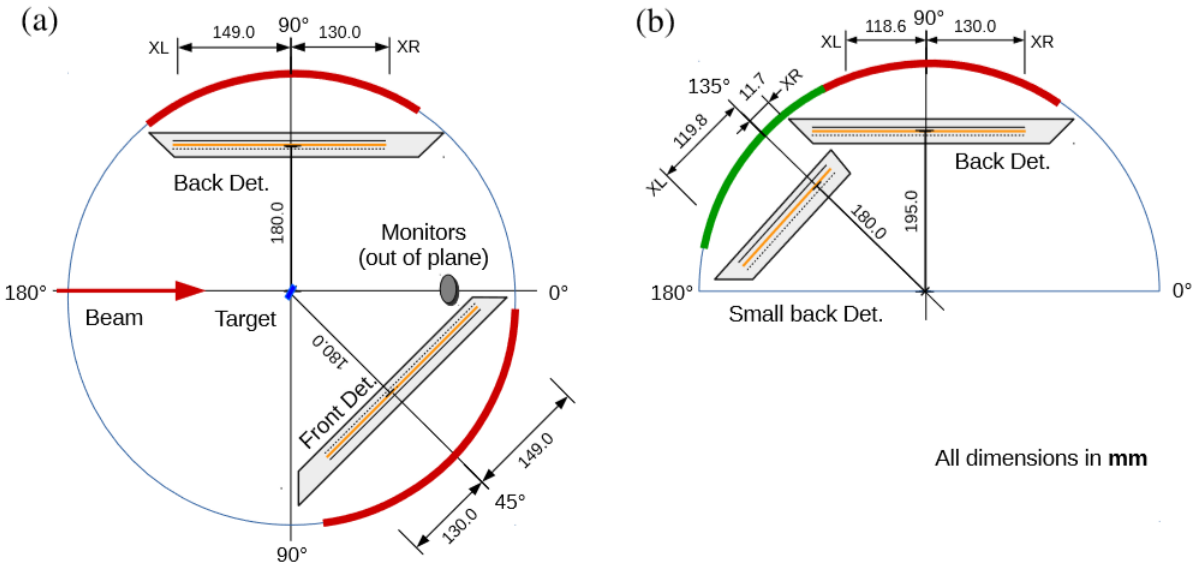


Figure 5.2: (a) Orientation of the front and back MWPCs with respect to the beam and target (b) Orientation of the back and small back MWPCs with respect to the beam and target

is proportional to the energy loss of the charged particle. After calibration, the energy loss of the particle can be used to identify the Z of the particle using the Bethe-Bloch formula, calculations from SRIM, or simulations from TRIM. The energy resolution of the detector is not good enough to separate single Z values, but provides an estimate of the distribution. A target ladder is mounted in the middle of the detector in the path of the beam, oriented at 60° to the beam axis in order to minimize the loss of reaction products through the target and the target frame.

Two Si surface barrier detectors (monitors) are mounted symmetrically around the beam axis at 25° or 30° with respect to the beam in order to measure elastically scattered beam particles. The sum of the counts of the two detectors corrects for minor fluctuations in the beam spot location. These monitors are used for target thickness measurements, absolute cross section determination, and tuning the incident beam.

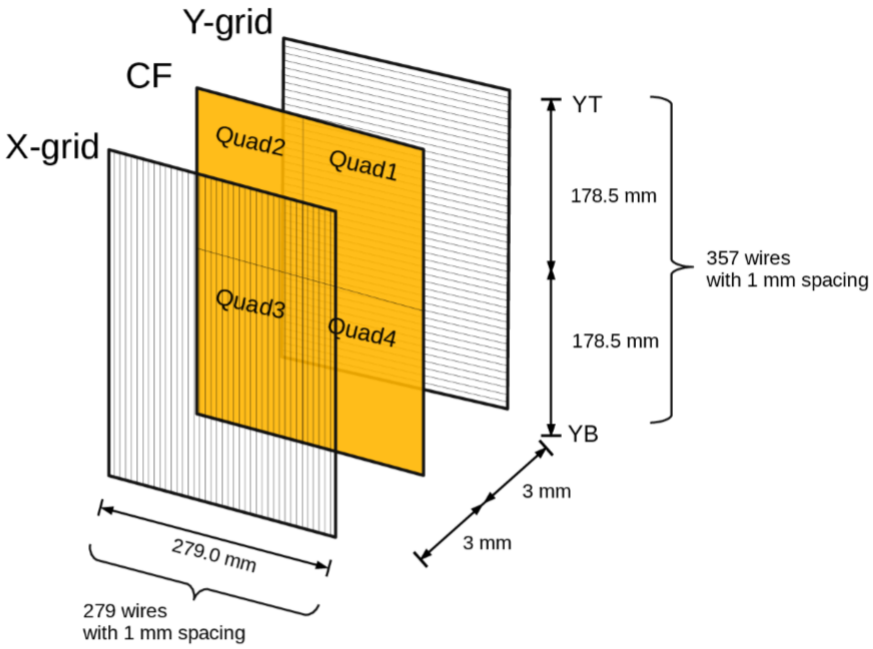


Figure 5.3: Schematic breakdown of the front or back MWPC.

## 5.3 Electronics and Data Acquisition

The signals from the MWPCs and silicon monitors are processed by the electronic setup in Figure 5.4. The timing signal from the cathode of the front MWPC was in coincidence with the back and small back MWPC and was then used in an OR logic gate with the signals of the two silicon monitors. The output of the OR was sent to the DAQ as a trigger signal. The coincidence of the timing signals between the front and back MWPCs efficiently decrease the otherwise high trigger rate caused by elastically scattered particles into the front detector. The signal of the Si monitors is sent to a scaler as well as each MWPC's signal. The difference between the scalers and the signal processed in the data acquisition is then used to determine DAQ dead time. Once a trigger is issued, the DAQ uses analog-to-digital converters (ADC) and time-to-digital converters (TDC) to process the detector data and stores all channels from all ADC and TDC modules in an event.

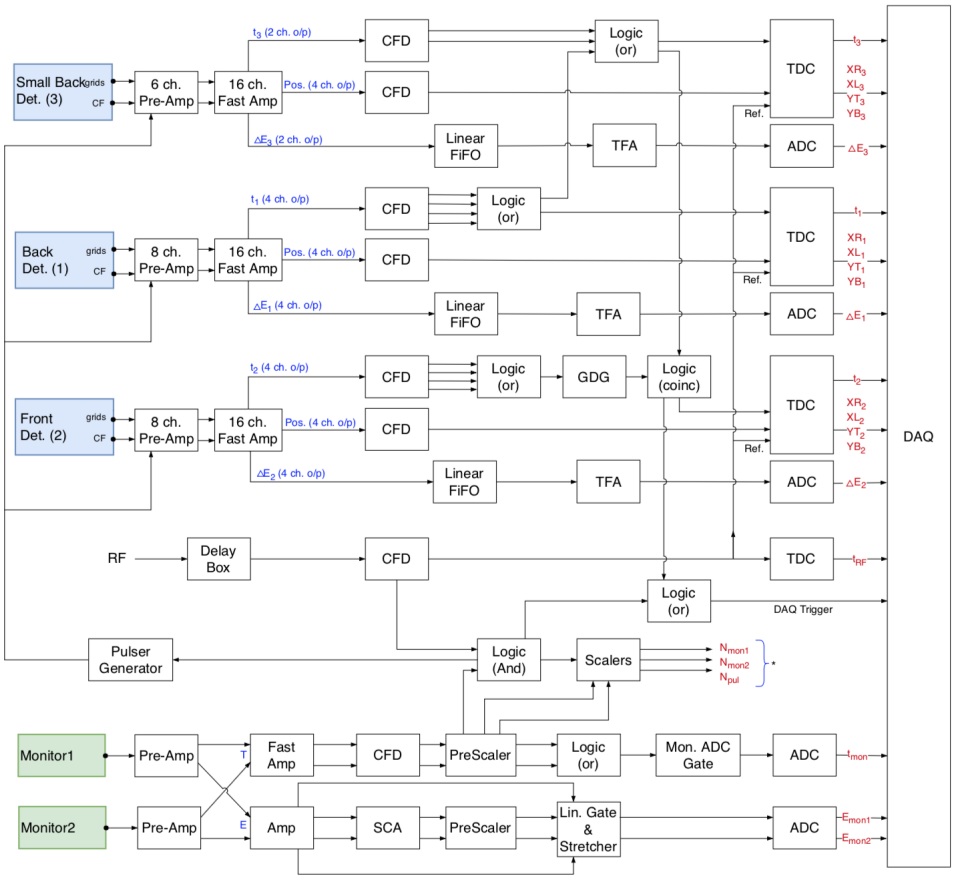


Figure 5.4: Electronics schematic of signal processing from the MWPCs and monitors to the DAQ.

## 5.4 Analyzing CUBE Data

Data taken from the CUBE detector is analyzed by a fission analysis program 'dacube', which was developed by the reaction dynamics group at ANU [96]. The program is a package of C/C++ codes with ROOT [97] libraries that reconstructs events, extracts reaction kinematics, processes event selection, and calculates absolute cross-sections. The following section describes the procedure 'dacube' to process CUBE data.

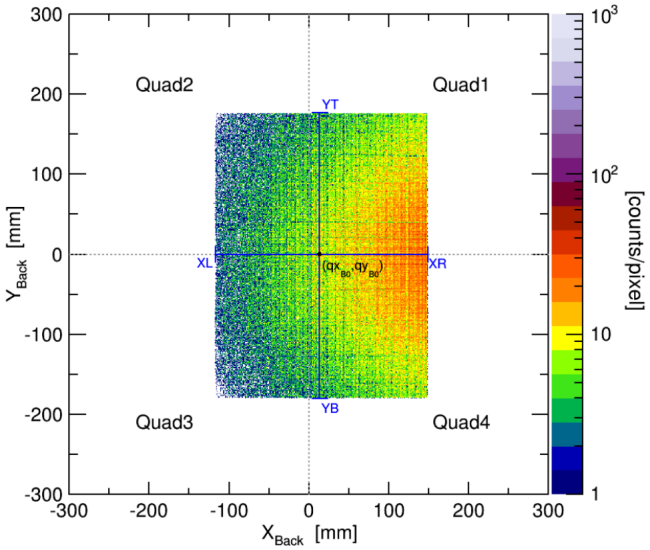


Figure 5.5: Full active area of the front MWPC in Cartesian coordinates

### 5.4.1 Track Reconstruction

#### 5.4.1.1 Position Transformation

The position of the particles is obtained from the crossing wire planes in each quadrant. These planes are connected to a delay line that is then read out at each side. This position is transformed into a physical position by a position calibration, which is done by matching the physical dimensions of each MWPC to the full active area recorded by the DAQ. Figure 5.5 shows an example of this position calibration with the back MWPC.

The 2D coordinates of each MWPC are then transformed into a 3D Cartesian coordinate reference frame with respect to the target using the known positions of the detectors in space, where the z axis aligns with the beam. From here these coordinates are transformed into spherical coordinates, where the radial coordinate r is the distance between the interaction of the particle with the MWCP and the origin (target) [98]. Figure 5.6 shows the full active area of all 3 MWCPs in spherical coordinates.

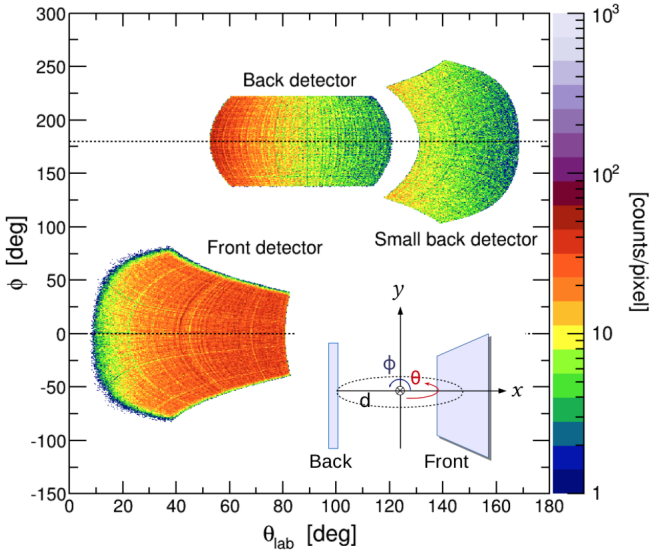


Figure 5.6: Full active area of all three MWPCs in polar coordinates

#### 5.4.1.2 Time of Flight

The time of flight for these experiments is defined as the time of interaction between the target foil ($t^{inter}$) and the cathode foil in the MWPCs ($t_i^{arr}$). As mentioned in section 5.2, the information obtained from the experiment is the time between the RF pulse and the time of interaction with the cathode foil. The true ToF can be extracted by removing the offset time between the RF signal and the arrival of the beam as well as the offset delay between each detector by:

$$\begin{aligned} ToF_1 &= T_1 - T_0 - \delta T_1 \\ ToF_2 &= T_2 - T_0 - \delta T_2 \\ ToF_3 &= T_3 - T_0 - \delta T_3 \end{aligned} \tag{5.1}$$

Figure 5.7 shows a diagram of the timing for the experiment. During analysis, $\delta T_1$ is set to zero and $T_0$ is set to yield the correct time for $ToF_1$. $\delta T_2$ and $\delta T_2$ are the offset times between detectors 2 and 1 and 3 and 1 respectively. ($T_0$, $\delta T_2$, $\delta T_2$) are dependent on velocity

and this determination is described in Section 5.4.2.3.

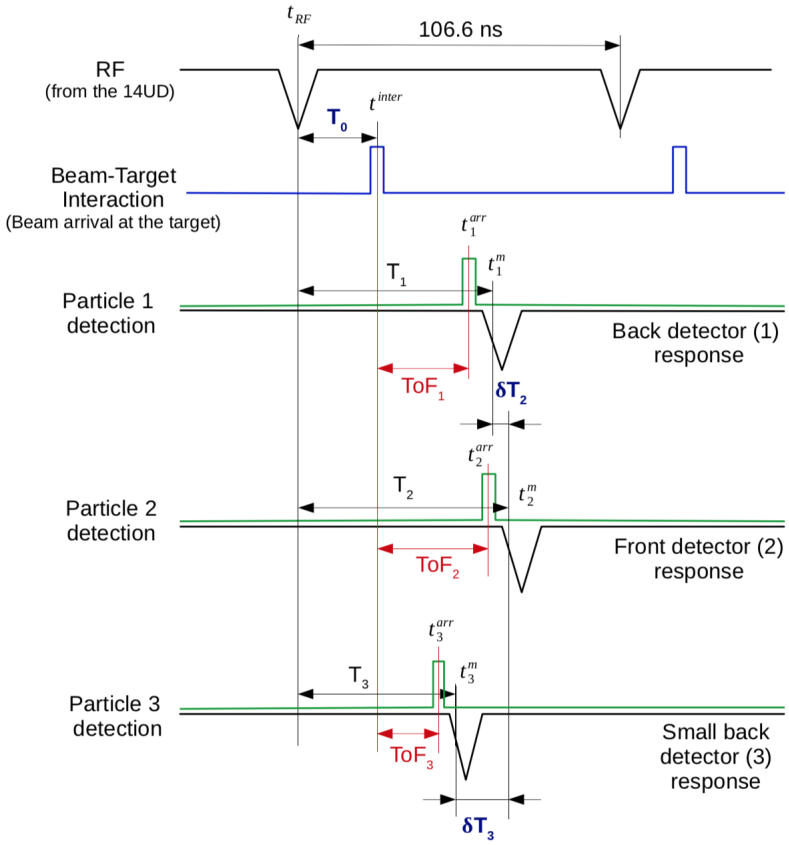


Figure 5.7: Timing of particle detection in MWPCs in conjunction with RF signal and beam-target time.

## 5.4.2 Kinematic Reconstruction

### 5.4.2.1 Velocity

Figure 5.8 shows the velocity vectors of a binary fission event and they can be broken down into parallel and perpendicular components relative to the beam axis:

$$w_i = v_i cos\theta_i \tag{5.2}$$

$$u_i = v_i sin\theta_i \tag{5.3}$$

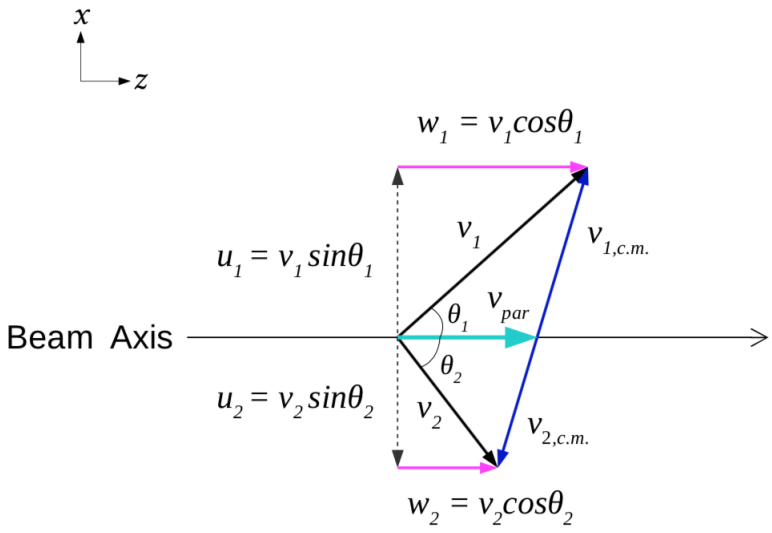


Figure 5.8: Vector breakdown of fission fragment velocities, with the origin at the reaction center on the beam axis.

Disregarding particle evaporation during fission and incomplete fusion, it can be approximated that fission fragments are emitted at 180° to each other in the center of mass frame for binary fission events. The sum of their momentum is always zero, yielding the equation:

$$\frac{u_i}{w_1 - v_{par}} = -\frac{u_2}{w_2 - v_{par}} \tag{5.4}$$

where $v_{par}$ is the velocity of the compound nucleus parallel to the beam. This equation can be rearranged to obtain $v_{par}$ using the measured quantities $v_i$ and $\theta_i$, giving the equation:

$$v_{par} = \frac{v_1 v_2 sin(\theta_1 + \theta_2)}{v_1 sin\theta_1 + v_2 sin\theta_2} \tag{5.5}$$

The perpendicular velocity of the compound nucleus can be represented by

$$v_{perp} = \frac{u_1 u_2 sin\phi_{12}}{\sqrt{u_1^2 + u_2^2 - 2u_1 u_2 cos\phi_{12}}} \tag{5.6}$$

where $\phi_{12} = \phi_1 + \phi_2$ are the folding angles perpendicular to the reaction plane. While it is possible to have small perpendicular velocities due to particle emission, measured values are expected to be centered around zero for full momentum transfer (FMT) fusion reactions.

#### 5.4.2.2 Mass Ratio

The mass ratio of the fission fragments can be described as the mass of one fragment relative to the combined masses of both fragments and can be calculated using conservation of linear momentum. :

$$A_1 v_{1cm} = A_2 v_{2cm} \tag{5.7}$$

Rearranging this equation and using the definition of mass ratio yields:

$$M_R = \frac{A_1}{A_1 + A_2} = \frac{v_{1cm}}{v_{1cm} + v_{2cm}} \tag{5.8}$$

Using the mass ratio, the total pre-neutron emission kinetic energy of the fission fragments can be estimated assuming both masses sum to the compound nucleus mass by:

$$< TKE >= \sum_{i=1}^{2} \frac{1}{2} m_i v_{icm}^2 \tag{5.9}$$

#### 5.4.2.3 Time Calibration

The timing parameters discussed in Section 5.4.1.2 were determined by the calculated values of the velocities of the binary fission fragments. These parameters are considered optimized when the velocities meet two requirements:

1. $< v_{perp} >= 0$

The average velocity perpendicular to the reaction plane should be zero for FMT binary fission events. There is the possibility to have small components due to the emission of light particles, but this will not have an effect on mass ratio calculation.

2. $< v_{par} > - v_{CN} = 0$

As a direct result of the first requirement, the average velocity parallel to the reaction plane should be equal to the velocity of the compound nucleus in the center of mass frame. The velocity of the compound nucleus can be calculated from experimental values by:

$$v_{CN} = 0.982 \frac{A_p}{A_p + A_t} \sqrt{\frac{2E_{lab}}{A_p}} \tag{5.10}$$

where $E_{lab}$ is the energy of the beam in the laboratory frame in MeV and $A_p$ and $A_t$ are the masses of the projectile and target respectively. The constant 0.982 is a conversion factor for converting atomic mass units to MeV/$c^2$.

Figure 5.9 shows a plot of these two requirements with optimized timing parameters for the $^{48}$Ca + $^{144}$Sm reaction at 201.0 MeV that was studied for this work.

### 5.4.3 Fission Selection

With proper reconstruction of events using the methods described in the previous sections, fission events need to be selected out of the pool of binary events. These binary events can consist of elastically scattered events with ejected target nuclei, reactions with the target backing or impurities within the target, coincidences with a single fission fragment and beam particle, and the desired binary fission event.

The cross-section for an elastically scattered event is orders of magnitude higher than a binary fission event for these types of reactions. The calculated velocity of the fissioning

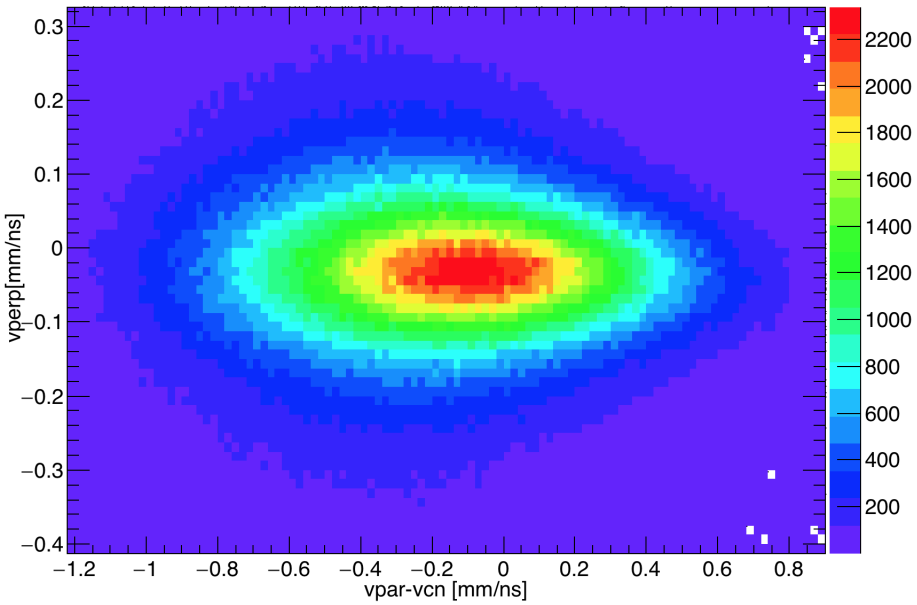


Figure 5.9: Experimentally derived perpendicular fission fragment velocities (vperp) as a function of parallel velocity (vpar) subtracted the velocity of the compound nucleus (vcn) after time parameter optimization for the $^{48}$Ca + $^{144}$Sm reaction at 201.0 MeV. This data includes fission events as well as elastically scattered events.

compound nucleus and the reconstructed velocities of both the elastically scattered particles and fission fragments are approximately equal, so elastic events must be differentiated by examining the mass ratio and TKE. Figure 5.10a shows the distinction between the two types of events, where the elastically scattered events are the high density regions at low and high mass ratio, corresponding with the light mass beam and heavy mass target. The fission events occur between these two regions. Any reactions with the target backing or impurities in the target will subsequently have reconstructed velocities much different from the calculated velocity of the compound nucleus. As a result, these reactions can be differentiated as $v_{par}/v_{CN}$ will have a value other than 1.

Variations of the deduced TKE from the expected TKE can also help select binary fission events from random coincidence events, as well as ensuring proper reconstruction of fission events. The expected TKE comes from Viola systematics [40], which assumes the projectile

kinematic energy is fully dissipated in the compound nucleus. The estimated TKE can be calculated using Viola systematics using the equation

$$TKE_{Viola} = 0.1189\frac{Z_{CN}^2}{A_{CN}^{1/3}} + 7.3(MeV) \tag{5.11}$$

and can be rearranged into an estimate that depends on mass ratio [99]

$$TKE_{Viola}(M_R) = \frac{0.789(1 - M_R)Z_{CN}^2}{[M_R^{1/3} + (1 - M_R)^{1/3}]A_{CN}^{1/3}} \tag{5.12}$$

A comparison of the experimental TKE to the estimated $\text{TKE}_{Viola}$ should result in a value close to 1 ($\text{TKE}/\text{TKE}_{Viola} = \text{RTKE} = 1$). Figure 5.10b shows this comparison of TKE values with the mass ratio. The fission fragments within the predicted mass ratio region lie along the $\text{RTKE} = 1$ region. The elastically scattered and quasi-fission events are represented with high intensity near the high and low mass ratio regions. They are elongated along the TKE axis due to the poor energy resolution of the MWPCs; these events are significantly faster than fission fragments, resulting in less energy loss in the MWPCs. Events that consist of a fission fragment in coincident with a fast, projectile-like particle are observed to appear above fission events with $\text{RTKE} > 1$.

Using these visual aids, a series of gates can be applied to isolate the binary fission events used in total cross-section calculation and can be seen applied in Figures 5.10a,b with red polygons.

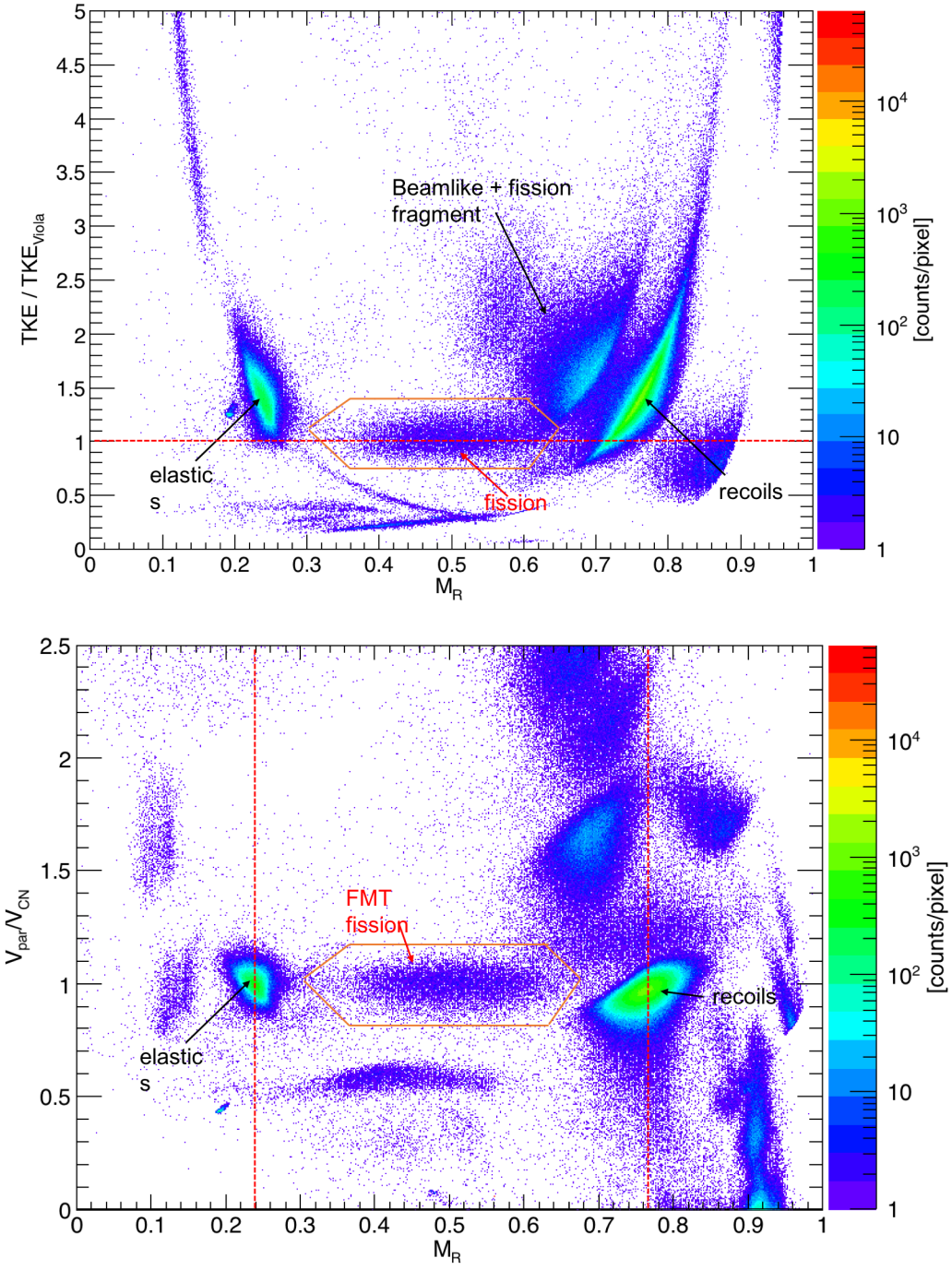


Figure 5.10: Visual cuts applied to mass ratio $M_R$ spectra in order to isolate fission fragments

# Chapter 6

# Cross Section Determination

In order to deduce the capture cross-section, all exit channels from the compound nucleus need to be taken into account, including fission, evaporation, and quasi-fission. This chapter focuses on extrapolating the fission cross-sections over the full angular range and integrating to get the total fission cross-section, and incorporating the evaporation cross-section to determine the total capture cross-section.

## 6.1 Differential Cross Section

The differential cross section in units of mb/sr for a reaction at a specific angle and beam energy can be defined as

$$\frac{d\sigma}{d\Omega}(\theta, E) = \frac{N(\theta, E)}{I_p N_t d\Omega} \tag{6.1}$$

where N($\theta, E$) is the number of particles hitting the detector at a specific angle $\theta$ and beam energy E, $I_p$ is the number of incoming beam particles, $N_t$ is the target density (atoms/cm$^2$), and d$\Omega$ is the solid angle (sr) [100]. Due to the CUBE detector's large angular coverage and position sensitivity, the solid angle can be assigned to angle bins within the total coverage (Figure 5.6) and can be written as

$$d\Omega_{cube} = \int\int sin\theta d\theta d\phi \approx sin\theta_c \Delta\theta \Delta\phi \tag{6.2}$$

where $\theta_c$ is the center degree of a bin with a width $\Delta\theta$. The silicon monitor detectors are not as large and do not have position sensitivity and as such cannot be represented in this way.

Using Equation 6.1, one can write the differential cross sections for the CUBE detectors and the silicon monitors as

$$\frac{d\sigma_{fis}}{d\Omega_{cube}}(\theta_c, E) = \frac{N_{cube}^{fis}(\theta_c, E)}{I_p N_t sin\theta_c \Delta\theta \Delta\phi} \tag{6.3}$$

$$\frac{d\sigma_{el}}{d\Omega_{mon}}(\theta_m, E) = \frac{N_{mon}^{el}(\theta_m, E)}{I_p N_t d\Omega_{mon}} \tag{6.4}$$

The monitors detect elastically scattered beam particles at forward angles ($el$), where $\theta_m$ is the monitor angle, and the CUBE detectors can detect both fission fragments and elastically scattered particles ($fis$).

The ratio of the differential cross sections between detectors can be taken and rearranged to give the fission differential cross section

$$\frac{d\sigma_{fis}}{d\Omega_{cube}}(\theta_c, E) = \frac{N_{cube}^{fis}}{N_{mon}^{el}} \frac{d\sigma_{el}}{d\Omega_{mon}}(\theta_m, E) \frac{d\Omega_{mon}}{sin\theta_c \Delta\theta \Delta\phi} \tag{6.5}$$

and then multiplied by $2\pi \text{sin}\theta_c$ to give the angular cross section

$$\frac{d\sigma_{fis}}{d\theta_{cube}}(\theta_c, E) = \frac{N_{cube}^{fis}}{N_{mon}^{el}} \frac{d\sigma_{el}}{d\Omega_{mon}}(\theta_m, E) \underbrace{\frac{2\pi d\Omega_{mon}}{\Delta\theta \Delta\phi}}_{S(\theta)} \tag{6.6}$$

This last term, denoted S($\theta$), is labelled as the normalization constant per bin and is determined by measuring the Rutherford scattering in both the CUBE detectors and silicon monitors at an energy below the fusion barrier. Equation 6.6 can be rearranged to solve for the normalization constant by replacing $fis$ with $el$ and adding $cal$ for calibration,

$$S(\theta) = \frac{N_{mon}^{el,cal}}{N_{cube}^{el,cal}} \left( \frac{d\sigma_{el}^{cal}}{d\Omega_{cube}}(\theta_c, E) \right) / \left( \frac{d\sigma_{el}^{cal}}{d\Omega_{mon}} \right) 2\pi sin\theta_c \tag{6.7}$$

It is important that when using Equation 6.7 in Equation 6.6 for cross section calculation, the widths of the angular bins $\Delta\theta$ and $\Delta\phi$ must be equivalent.

## 6.2 Cross Section Code

This section outlines the process of implementing Equation 6.6 in the analysis by resolving all of the components involved.

### 6.2.1 Establishing Variables

In order to evaluate the equations in the previous sections, certain variables need to be defined.

1. Angle bin width ($\Delta\theta$).

   The bin width depends on the statistics of a run along with the solid angle normalization, which is dependent on the type of reaction. For light systems, the angular distribution for fusion-fission does not vary drastically with angle, so typically 5° bins are used[101]. Heavy reactions, such as in this experiment, tend to have a more drastic change in angular distribution. As a result, 3° bins were used.

2. Elastic scattering on the silicon monitors ($N_{mon}$).

   As mentioned in Section 5.2, two silicon monitor detectors are mounted at forward angles ($\theta_m = 30^\circ$). The sum of these two yields resolves any issue with variations in beam spot position or entry angle to the first order.

3. Correction of dead time ($N_{mon}$ and $N_{cube}$)

   The DAQ used for data collection has a certain dead time which needs to be accounted for. Figure 5.4 shows the signals from the monitors and MWPCs go to both the DAQ as well as a scaler module. The ratio of the number of counts from each yields a dead time correction factor that is then applied to both $N_{mon}$ and $N_{cube}$.

4. Normalization constant per bin S($\theta$).

   This constant is determined by performing calibration runs below the fusion barrier. These runs were performed using one MWPC at a time and scaled to the back detector due to differences in time of run and beam current. The angular coverage of the detectors and the normalization constant can be seen in Figure 6.1.

### 6.2.2 Lab Frame to Center of Mass Frame

The angular cross sections are evaluated event by event in the lab frame and then converted to the center of mass frame. The reason for this is two-fold: 1) The solid angles and normalization constant are measured in the lab frame. This eliminates any unnecessary transformations that could lead to potential error, and 2) multiple lab angle bins can occupy a single center of mass bin for reactions with a large range of mass ratios. By making the transformation event-by-event, this eliminates the potential for round-off error due to the

binning effect. Figure 6.1 shows the lab to center of mass transformation. It is important to note that the nearly full detection in the lab frame has a coverage of about 90°-160° in the center of mass frame. Since fission angular distributions are symmetric with respect to 90° in the center-of-mass frame, the events can be reflected over a "mirror line"

### 6.2.3 Mass-Angle Distributions (MADs)

Figure 6.2 shows a plot of the normalized fission events seen by the back detector for a run, specifically the mass ratios and angles of fragments. It is important to note that the DAQ only records an event when there is a coincidence between the back and front detectors or the small back and front detectors, as a result there will be complimentary fission fragment recorded by the front detector. Examples of this can be plotted with black squares and white circles. If left unchecked, this would produce an excess of identical points when reflected over the "mirror line". In order to remove this excess, events are rejected from the front detector if they lie beyond the mirror line. An acceptable mirror line should run through (0.5,90) and can be represented in Figure 6.2 by the dashed black line.

The angular distribution can be obtained by projecting the MAD plot onto the y-axis. For mirrored plots and heavy systems, the mass ratio range should be restricted to either $M_R > 0.5$ or $M_R < 0.5$. This is applied due to the notable presence of fast quasifission in heavy systems, which has a strong correlation of emission angles and fragment mass.

### 6.2.4 Experimental Differential Cross Sections

## 6.3 Cross Section Extrapolation

The CUBE detectors cover only a specific angular range. In order to calculate the total fission cross section, the differential cross sections obtained from the angular coverage of the CUBE detectors need to be extrapolated. The method of extrapolation for this analysis relies on the transition state model (TSM) introduced in Section 2.2 and utilized in Section 3.6.4. Due to the broader range of angular cross sections in these data compared to Section 3.6.4, the application of the TSM is slightly altered. The fission angular distribution, assuming the projectile and target spins are zero and a Gaussian K distribution, can be expressed by

$$W(\theta) = \sum_{J=0}^{\infty}(2J+1)T_J \sum_{K=-J}^{J} \rho_J(K)|D^J_{0,K}(\theta)|^2 \tag{6.8}$$

where $\rho_J(K)$ is are the density levels at the transition state and $T_J$ is the transmission coefficient for fusion of partial wave J. $\rho_J(K)$ can be expressed as

$$\rho_J(K) \propto \begin{cases} \frac{exp(-K^2/2K_0^2)}{\sum_{K=-J}^{J} exp(-K^2/2K_0^2)}, & if K \leq J \\ 0, & K > J \end{cases} \tag{6.9}$$

where the variance of the K distribution is expressed as $K_0$ and is characterized by $K_0^2$. The K distribution is assumed to be independent of J. $K_0^2$ can be estimated from the transition state as seen in Equation 3.11 Because these variables aren't well known for compound nuclei at the saddle point, $K_0$ is used as a fitting parameter by adjusting the value for a calculated J distribution until a minimum $\chi^2$ fit to the fission angular distribution was met.

Figure 6.3 shows the fits of $^{40,48}$Ca + $^{144}$Sm and $^{39}$K + $^{208}$Pb over all experimental energies using this method. The total fission cross sections are calculated by integrating the fit from 90° to 180° and multiplying by $2\pi sin\theta_{cm}$.

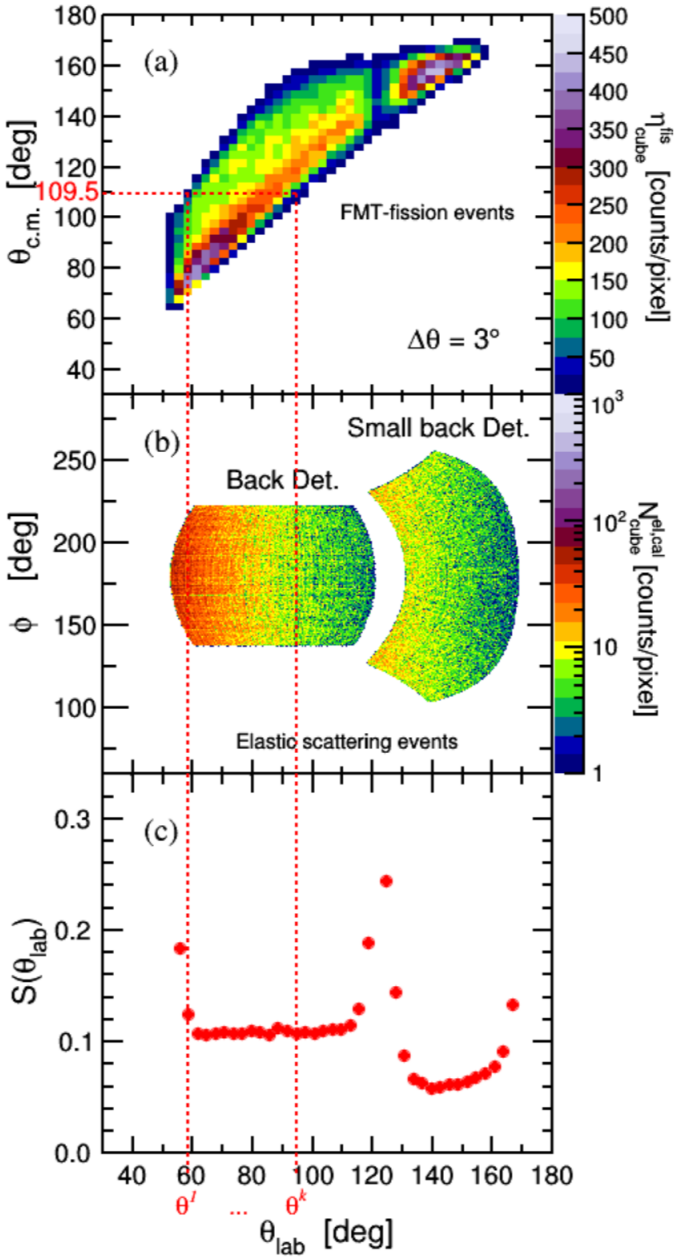


Figure 6.1: (a) Scatter plot of $\theta_{lab} vs. \theta_{c.m.}$ with only full momentum transfer (FMT) events. The efficiency corrected yield $\eta^{fis}_{cube}$ is represented on the z-axis. (b) The active area of the small back and back detectors represented in spherical coordinates from an elastic scattering calibration run; the results of which provide solid angle normalization coefficients S($\theta_{lab}$) shown in (c).

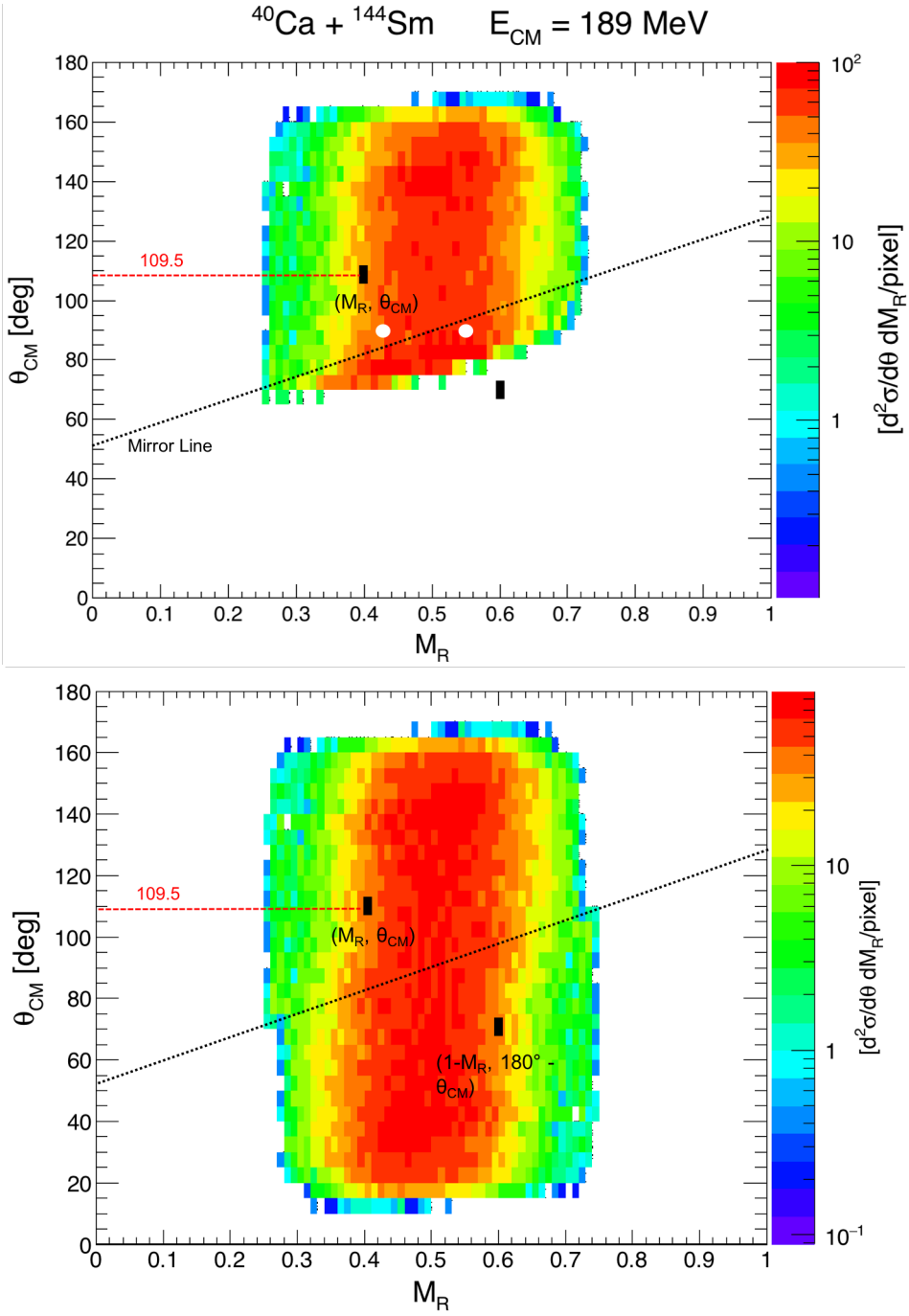


Figure 6.2: Top: Experimental mass ratio data for $^{40}$Ca + $^{144}$Sm reaction with applied mirror line. Bottom: Reflection of experimental mass ratio data across mirror line.

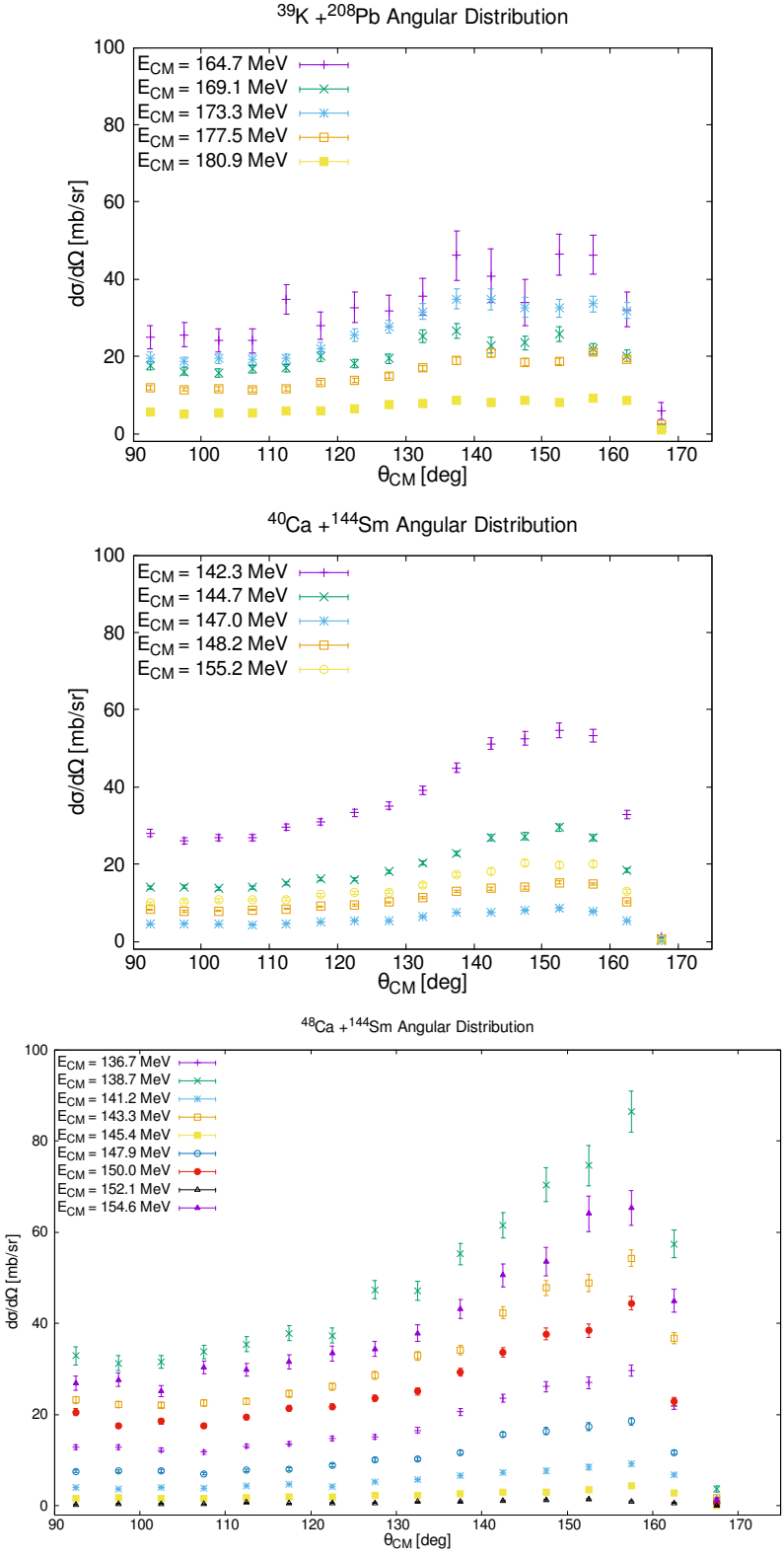


Figure 6.3: Fission angular distributions for $^{40,48}$Ca + $^{144}$Sm and $^{39}$K + $^{208}$Pb reactions over all experimental energies.

# Chapter 7

# Results

This section describes the processes to extract the total capture barriers and interaction radii after the addition of evaporation residue cross sections. The data are used for comparison in reduced excitation functions, models, and competing fission modes.

## 7.1 Evaporation Residue

The total capture cross section can be described as the sum of the fission, evaporation residue, and quasi-fission cross sections. The fission and quasi-fission cross sections cannot be distinguished in the analysis and the evaporation residue cross sections were not measured. Therefore the evaporation-residue cross-sections need to be estimated from another source in order to calculate the fusion barrier and interaction radius properly. There have been no evaporation residue cross-sections measured experimentally for the $^{39,46}$K + $^{208}$Pb and $^{40,48}$Ca + $^{144}$Sm reactions. Therefore theoretical models are needed. Two requirements that need to be fulfilled in order to validate the calculation are that 1) it reproduces the previously measured experimental fusion-evaporation residue cross-sections of the $^{28}$Si+$^{164}$Er reaction (the reaction generates the same compound nucleus, $^{192}$Pb, as the $^{48}$Ca + $^{144}$Sm reaction) and 2) it reproduces experimental fusion-fission cross-sections of the reactions done in this work. ER cross-sections for the $^{28}$Si+$^{164}$Er reaction are shown below in Figure 7.1 using a number of different Monte-Carlo calculations and are compared to experimental cross

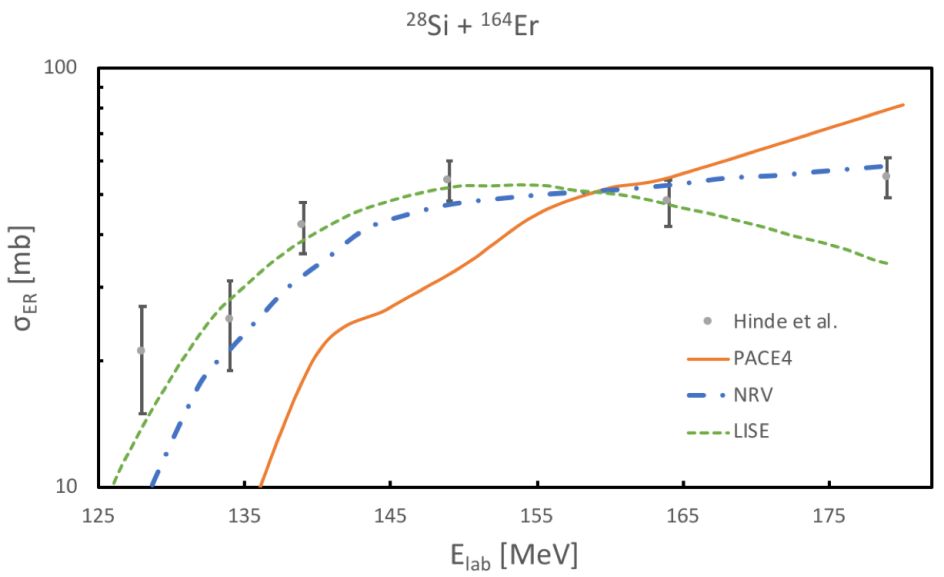


Figure 7.1: Experimental ER cross sections measured by Hinde [102] with Monte Carlo calculations, including PACE4 and implementations of the Decay of Excited Nuclei by the Nuclear Reactions Video website and LISE++.

sections measured by Hinde et al. [102]. The implementation of the Decay of Excited Nuclei implemented in LISE++ [103, 104], mentioned in Section 2.3.2, shows the best fit to the experimental data, specifically at lower energies. This is important in determining the fusion barrier, as the method for barrier extraction discussed in the next section is sensitive to cross sections measured near the barrier energy.

The Monte-Carlo used by LISE++ for the $^{39}$K + $^{208}$Pb and $^{40,48}$Ca + $^{144}$Sm reactions are shown in Figure 7.2. The calculated fission cross sections (black) are adjusted to fit the experimental cross sections (green) by adjusting the Sierk fission barrier height and the curvature parameter of the parabolic potential describing the fission barrier. The total capture cross section (red) is the sum of the fusion-fission and fusion-evaporation (blue) curves. For these reactions the calculated fusion-evaporation residue cross sections are orders of magnitude smaller than the fusion-fission cross sections and will should not affect the capture cross sections. Nevertheless, the calculated evaporation residue cross sections are

added to the measured fission cross sections at their respective energies.

## 7.2 Barrier Height and Interaction Radius Extraction

The barrier heights and interaction radii for the $^{39}$K + $^{208}$Pb and $^{40,48}$Ca + $^{144}$Sm reactions were extracted from the capture cross sections (experimental fission + calculated evaporation residue) using the $1/E_{cm}$ method seen in Figure 7.3. The classical equation for the fusion cross section above the fusion barrier given in Equation 2.6 is fitted to the high energy points above the barrier to be extracted. The inverse of the x-intercept of this fit yields the experimental barrier heights and interaction radii. As mentioned in Section 2.1.1, this function is for energies above the capture barrier. Therefore the deviation of the cross-sections at lower energies at or below the barrier from the fitted function is due to quantum-mechanical effects and cannot be included in the fit.

W. J. Świątecki et al.[105] uses an empirical description to represent systematics of experimental capture barriers as

$$V_B = 0.85247z + 0.001361z^2 - 0.00000223z^3(MeV) \tag{7.1}$$

where the Coulomb barrier parameter $z$ is

$$z = \frac{Z_1 Z_2}{A_1^{1/3} + A_2^{1/3}} \tag{7.2}$$

Christensen et al.[106] uses an empirical method to derive the radius of the Coulomb barrier as

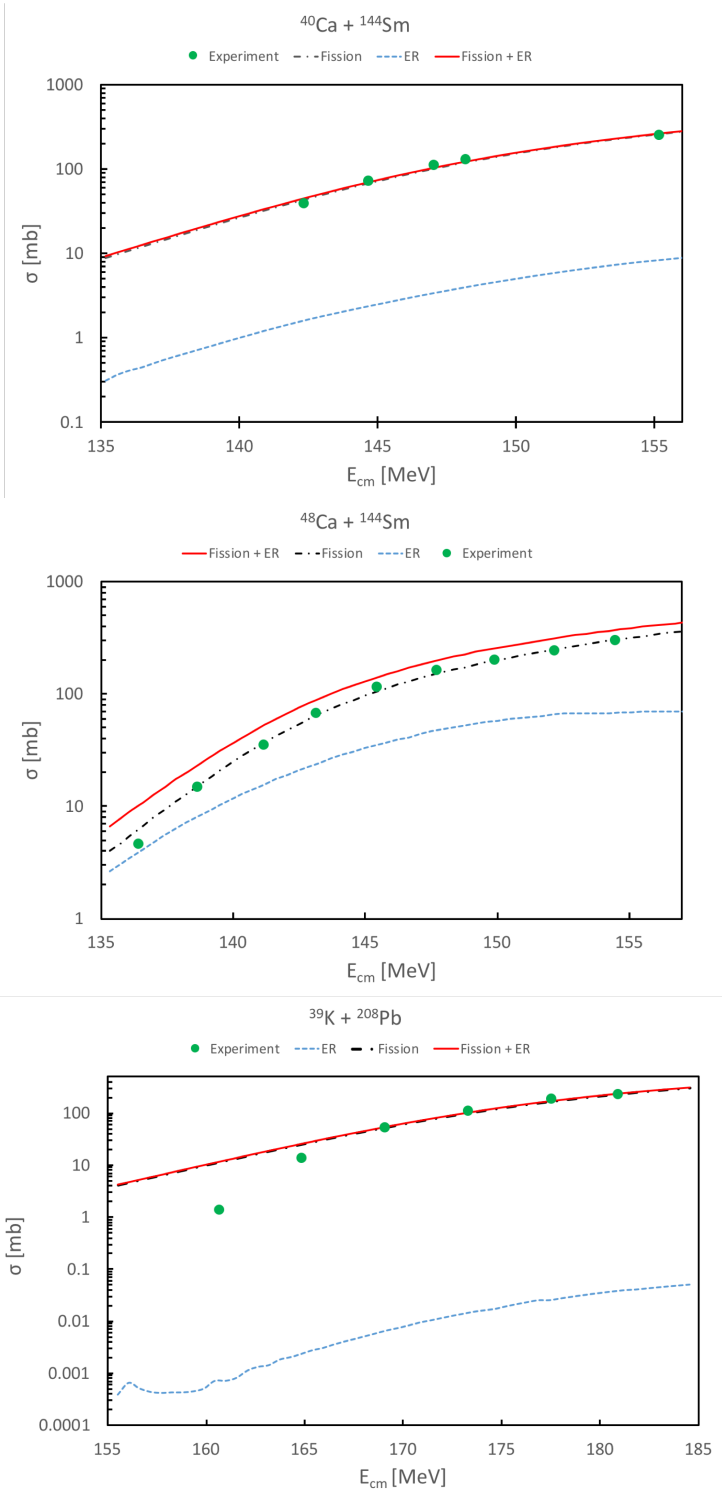


Figure 7.2: Experimental fission cross sections for $^{39}$K + $^{208}$Pb and $^{40,48}$Ca + $^{144}$Sm reactions compared to calculated total capture, fusion-fission, and fusion-evaporation cross sections from the Decay of Excited Nuclei Monte Carlo implemented by LISE++.

$$r_B = 1.07(A_1^{1/3} + A_2^{1/3}) + 2.72(fm) \tag{7.3}$$

A comparison of measured and calculated barriers and interaction radii can be found in Tables 7.1 and 7.2. Measured barriers are in good agreement with calculated values within $2\sigma$ and measured radii are between 1-3 fm less than calculated values. The uncertainties in the measured values were evaluated from statistical uncertainties in the fitted cross sections and the uncertainty of the fitted function.

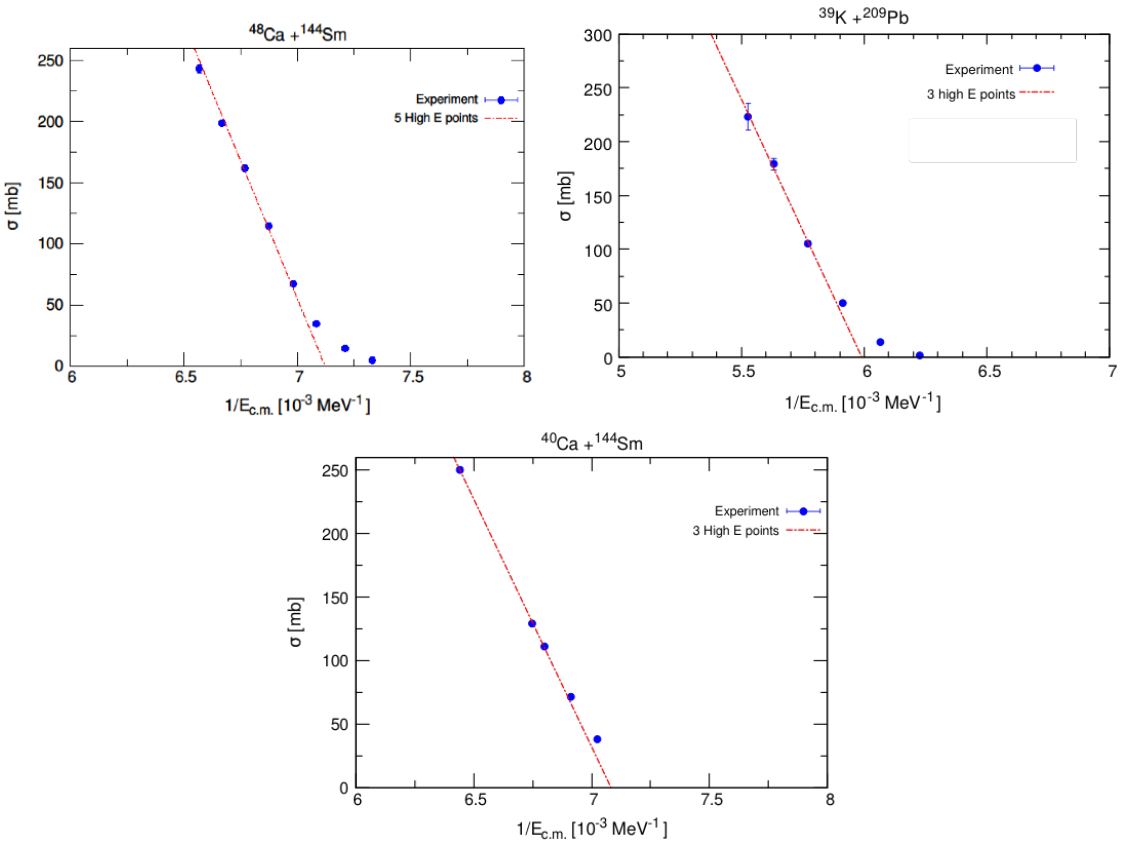


Figure 7.3: Measured cross sections as a function of $1/E_{cm}$ fitting with the classical equation Eq. 2.6 with points high above the barrier. The inverse of the x-intercept yields the experimental barrier height and interaction radius.

| | Capture Barriers (MeV) | |
|---|---|---|
| **System** | **Experiment** | **W. J. Swiatecki et al.** |
| $^{39}$K + $^{208}$Pb | 167.0 ± 0.6 | 168.0 |
| $^{40}$Ca + $^{144}$Sm | 141.2 ± 0.2 | 141.1 |
| $^{48}$Ca + $^{144}$Sm | 140.0 ± 0.3 | 138.6 |

Table 7.1: Experimental barrier heights in comparison with calculated barriers [105].

| | Interaction Radius (fm) | |
|---|---|---|
| **System** | **Experiment** | **Christensen et al.** |
| $^{39}$K + $^{208}$Pb | 9.7 ± 0.3 | 12.1 |
| $^{40}$Ca + $^{144}$Sm | 9.5 ± 0.1 | 11.4 |
| $^{48}$Ca + $^{144}$Sm | 11.1 ± 0.1 | 11.8 |

Table 7.2: Experimental interaction radii in comparison with calculated radii [106].

### 7.2.1 Reduced Excitation Functions

A comparison of the reduced excitation functions from the systems in this work, $^{40,48}$Ca + $^{144}$Sm, and the excitation functions measured by J. J. Kolata [107] in the neighboring systems $^{40,48}$Ca + $^{124,132}$Sn using inverse kinematics can be found in Figure 7.4.

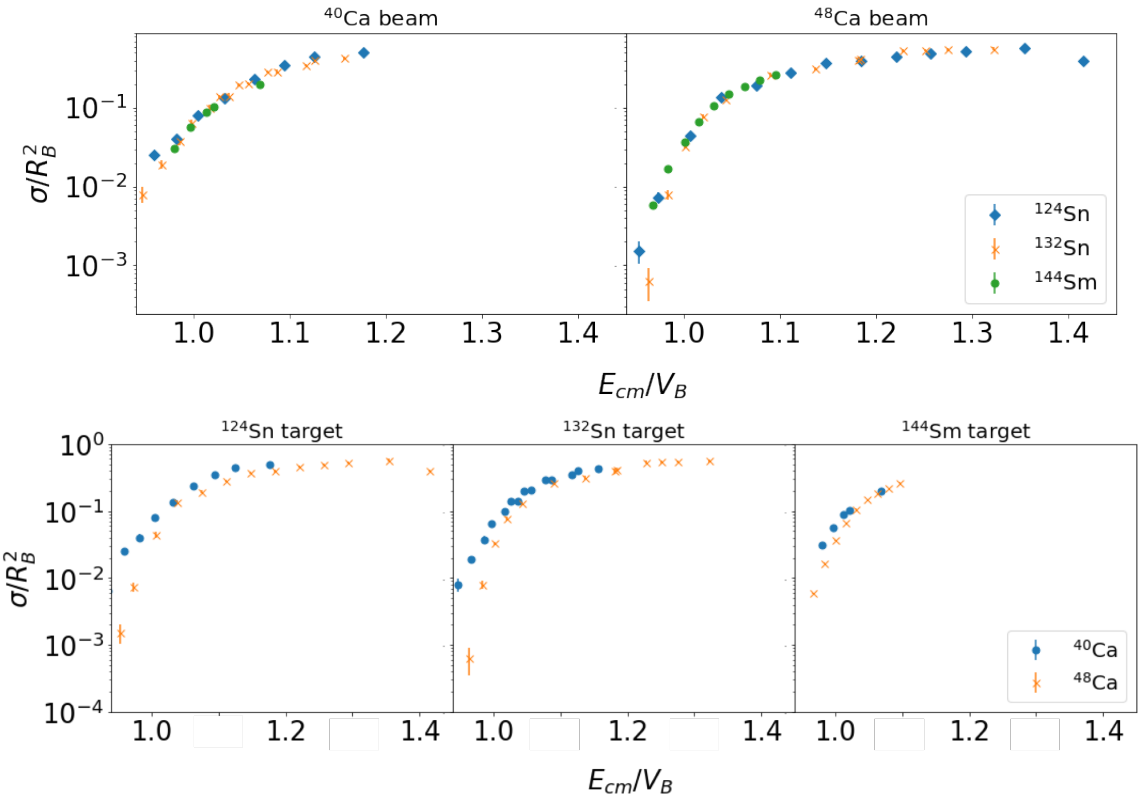


Figure 7.4: Comparison of the reduced excitation functions of this work, $^{40,48}$Ca + $^{144}$Sm, and by J. J. Kolata, $^{40,48}$Ca + $^{124,132}$Sn. Top: Light ion is identical while changing the heavy ion. Bottom: Heavy ion is the same with different light ions.

Above the barrier $E_{cm}/V_B > 1$, there are no enhancements observed of the capture cross section like observed by Loveland et al. for the $^{38}$S + $^{208}Pb$ reaction. For $E_{cm}/V_B \leq 1$ there is an enhancement of the capture cross sections for $^{40}$Ca compared to $^{48}$Ca (Figure 7.4 bottom). Kolata et al. observed that the sub barrier enhancements of $^{40}$Ca + $^{124,132}$Sn are due to positive Q-value neutron channels not present in the $^{48}$Ca + $^{124,132}$Sn systems. This conclusion can be applied for the $^{40}$Ca + $^{144}$Sm reaction as well. Tables 7.3 and 7.4 shows the

presence of positive Q-value neutron channels for the $^{40}$Ca + $^{144}$Sm reaction not found with $^{48}$Ca + $^{144}$Sm, which explains the slight capture cross section enhancement at the barrier. This enhancement is suppressed when compared with $^{124,132}$Sn, and this suppression can be attributed to the number of open channels. The $^{40}$Ca + $^{144}$Sm reaction has one extra positive Q-value neutron channel in comparison to the $^{48}$Ca + $^{144}$Sm reaction. J. J. Kolata observed that there are more many more for the $^{40}$Ca + $^{124,132}$Sn reactions, resulting in a higher enhancement.

| | **$^{40}$Ca + $^{144}$Sm** | **$^{48}$Ca + $^{144}$Sm** |
|---|---|---|
| **+1p** | -5.2 | +3.3 |
| **+2p** | -5.8 | +11.2 |
| **+1n** | -2.2 | -5.4 |
| **+2n** | +0.7 | -7.6 |
| **+1p1n** | -3.5 | -0.5 |
| **+2p2n** | +5 | +7.5 |

Table 7.3: Q-values for neutron and proton pick-up channels from the heavy to the light reaction partner.

| | **$^{40}$Ca + $^{144}$Sm** | **$^{48}$Ca + $^{144}$Sm** |
|---|---|---|
| **-1p** | -5.0 | -12.5 |
| **-2p** | -15.5 | -20.7 |
| **-1n** | -8.8 | -3.2 |
| **-2n** | -13.7 | -2.0 |
| **-1p1n** | -11.0 | -13.7 |
| **-2p2n** | -10.3 | -17.2 |

Table 7.4: Q-values for neutron and proton stripping channels from the light to the heavy reaction partner.

### 7.2.2 Competing Fission Modes

Tseckhanovich et al.[108] observed competition between symmetric and asymmetric fission modes for the $^{36}$Ar + $^{142}$Nd reaction by deducing fragment distributions from measured fragment velocities. Motivated by these observations, a similar analysis was done for the $^{40,48}$Ca + $^{144}$Sm reactions and an example is demonstrated in Figure 7.5. The TKE spectrum, reconstructed in Section 5.4.2.2, for these reactions at different beam energies show a slight skew that can only be fitted by a two-Gaussian distribution. This fit reveals two TKE components, $TKE^{low}$ and $TKE^{high}$, which are linked to the symmetric and asymmetric fission modes. This can be illustrated by the contrast of the shape of the partial mass distributions reconstructed in the regions above $TKE^{high}$ and below $TKE^{low}$ and projected onto the mass axis (Fig 7.5 bottom). The best fit description of these partial mass distributions are obtained by either one- or two-Gaussian fits, where a one-Gaussian fit implies a symmetric fission mode and a two-Gaussian fit implies an asymmetric fission mode.

This difference in mass distributions between $TKE^{low}$ and $TKE^{high}$ is expected. The kinetic energy follows $TKE \propto \frac{Z_1 Z_2}{(A_1^{1/3}+A_2^{1/3})}$. The highest kinetic energy that can be obtained from this equation from a fissioning system is when $Z_1 = Z_2$, or mass symmetric mode. In the mass asymmetric mode $Z_1 \neq Z_2$, resulting in a lower kinetic energy. This is observed in the data, where the higher kinetic energy region $TKE^{high}$ has a more symmetric fission mode and lower kinetic energy region $TKE^{low}$ has a more asymmetric fission mode.

### 7.2.3 Comparison to Models

A more quantitative interpretation can be obtained by comparing to models. The fission fragment mass distributions (FFMD's) for the $^{40,48}$Ca + $^{144}$Sm reactions are compared to

Monte Carlo codes GEF and Gemini (described in Section 2.3) in Figure 7.6. Gemini over-estimates the symmetric mass yield and under-estimates the heavy fragment yield for the $^{40,48}$Ca + $^{144}$Sm reactions. GEF predicts an asymmetric yield for the $^{48}$Ca + $^{144}$Sm reaction which isn't reproduced by experiment.

The level density at the saddle point at low excitation energy is heavily influenced by structure effects, which include shell effects and the Q-values of the splitting system. These effects begin to disappear at high excitation energy of the compound nucleus. The inaccurate predictions of Gemini for these compound nuclei at high excitation energies would mean that Gemini has too low of a transition of level densities with shell effects (low excitation energy) to level densities without these effects (high excitation energy).

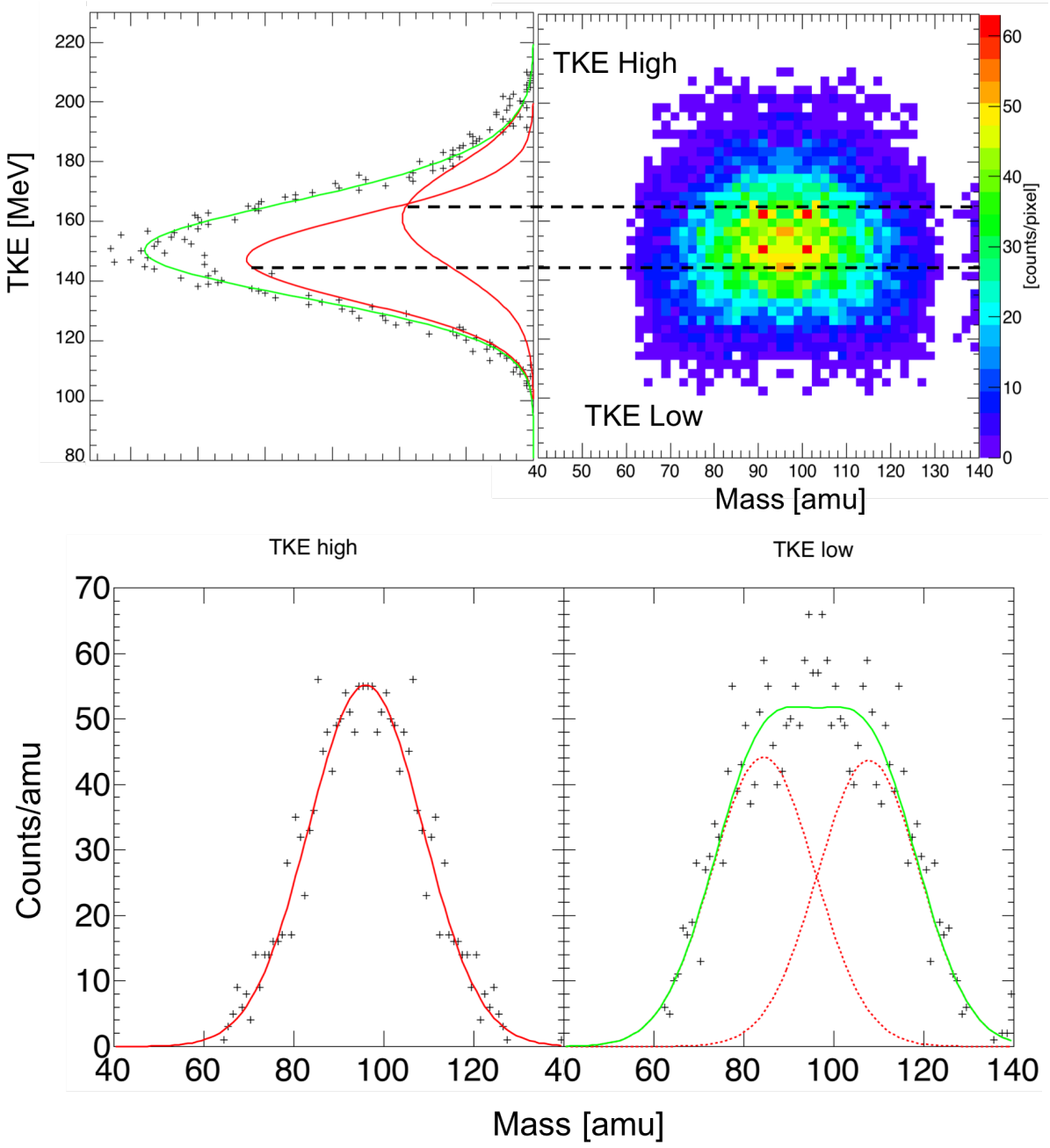


Figure 7.5: Reconstructed TKE and mass distributions of $^{40}$Ca + $^{144}$Sm at 186 MeV. Top left: TKE distribution with a two-Gaussian fit and partition into high and low TKE regions. Top right: Fission fragment mass distribution with projected TKE partitions based on two-Gaussian fit. Bottom: Projected fission fragment mass distributions above $TKE^{high}$ and below $TKE^{low}$ with best fit descriptions by either one- or two-Gaussian fits.

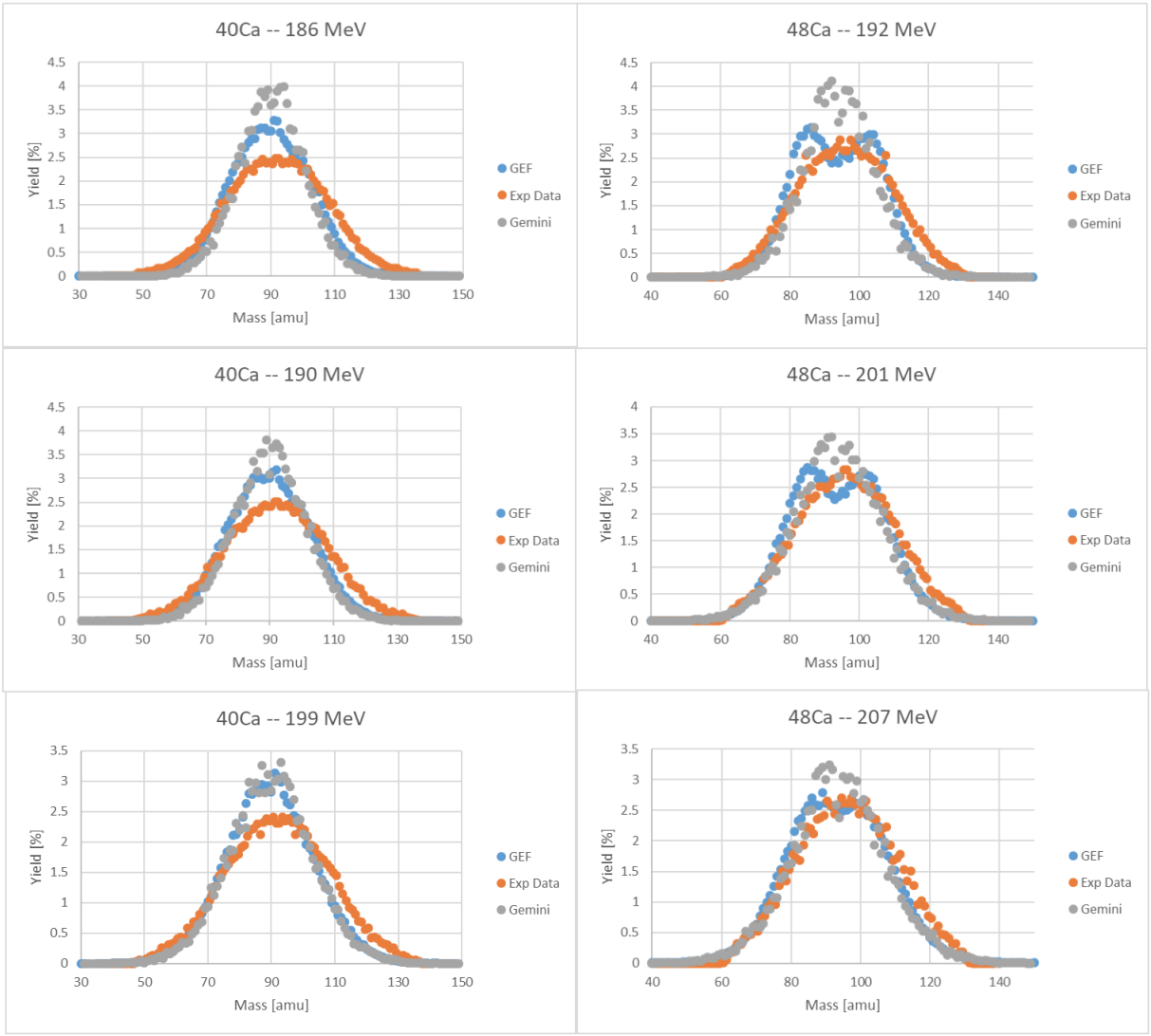


Figure 7.6: Experimental fission fragment mass distributions compared to mass distributions calculated by Monte Carlo codes GEF and Gemini for $^{40,48}$Ca + $^{144}$Sm

# Chapter 8

# Interpretation and Future Work

The results of fusion-fission experiments performed by Loveland et al. [9] showed important enhancements to the capture cross sections when using more neutron-rich RIBs, in this case $^{38}$S. This opened the prospect of increasing the extremely small cross-sections for super-heavy element formation and of creating more neutron-rich super-heavy isotopes, which are studied to better understand nuclear stability, structure, and dynamics. The present study of similar systems, $^{39,46}$K + $^{208}$Pb, $^{40,48}$Ca + $^{144}$Sm, and $^{40,48}$Ca + $^{124,132}$Sn, reveals that medium to low neutron excess does not seem to affect the capture cross sections above the barrier, and the results are consistent with Hinde et al [109].

The fusion excitation functions measured in this work found clear enhancements in the capture cross sections at and below the barrier for less neutron rich beams due to positive Q-value neutron pickup channels not present in the more neutron rich beams. Preliminary results from FRESCO calculations reinforce this conclusion. Figure 8.1 shows a clear enhancement of the experimental cross section when compared to the calculated cross sections without the inclusion of open transfer channels. Alternatively, Q-value calculations of much more neutron-rich beams, $^{50}$Ca + $^{144}$Sm for example, result in positive Q-value proton pickup channels, which could yield enhancements to capture cross sections at and below the barrier as well.

The introduction of the Facility for Rare Isotope Beams (FRIB) at Michigan State Univer-

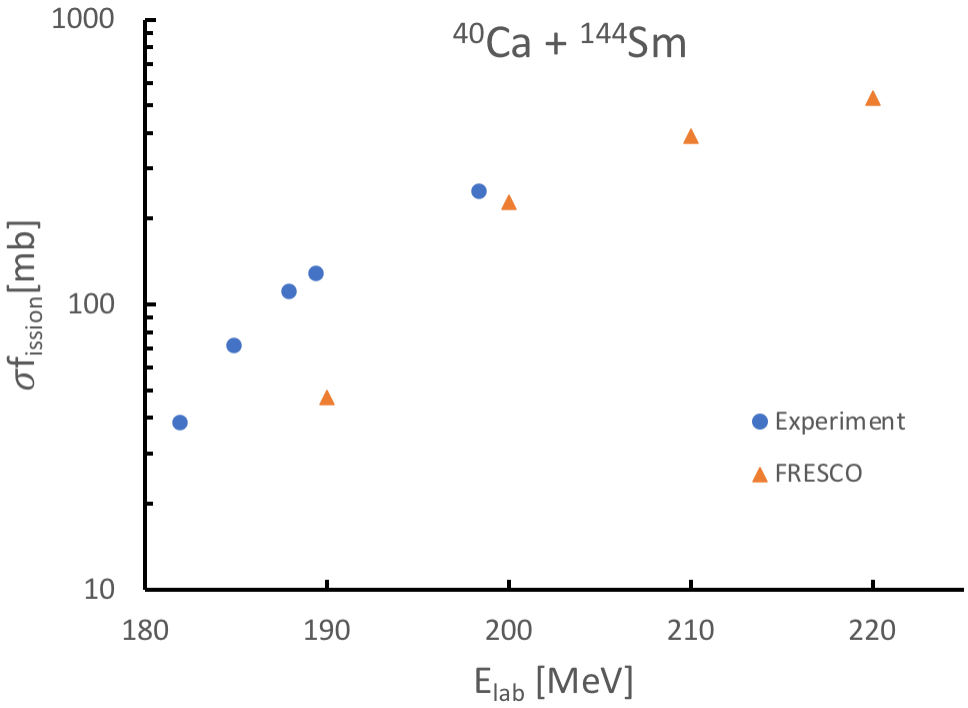


Figure 8.1: Experimental fission cross sections of $^{40}$Ca + $^{144}$Sm (blue circles) compared to calculated cross sections using FRESCO (gold triangles) without coupling to open transfer channels.

sity will produce high intensity neutron-rich RIBs which will enable the AT-TPC to measure the fusion excitation functions of reactions with high neutron excess. The transition from ReA3 to ReA6 and from ReA6 to ReA12 will enable the exploration of these fusion reactions at higher energies and will also allow the use of ancillary detectors upstream of the AT-TPC that can assist in beam identification.

The fusion-fission experiments utilizing the AT-TPC, $^{46}$K,$^{19}$F + $^{208}$Pb, were the initial assessment of this detector for use of future fusion-fission and fusion-evaporation measurements using both solid and gas targets. The AT-TPC has been found to be ideal for highly efficient anisotropy and fusion excitation function measurements. With more systematic studies of detector conditions and data analysis, Z identification of fission fragments will be possible and lead to the measurement of Z-distributions and quasi-fission studies. The present experiments also led to the creation of a new analysis method for AT-TPC data that will be a guide for future experiments measuring fusion-fission reactions.

Since the AT-TPC can measure total excitation functions when using a gas target, capture excitation function measurements can be expedited using the AT-TPC with a gaseous heavy target. Future work using the AT-TPC detector can focus on heavy ion fusion-fission reactions using a heavy gas target with neutron excess beam such as $^{54}$Ca or $^{53}$K, with intensities of $\sim 10^2$ pps, to explore fusion excitation functions at the limit of stability. Possible heavy gas targets include high Z noble gases including $^{40}$Ar, $^{84}$Kr, $^{129,131,132}$Xe, and more speculatively organometallic compounds such as tetraethyl- and tetramethyl-lead.

# BIBLIOGRAPHY

# BIBLIOGRAPHY


[1] A. Sobiczewski, F. Gareev, and B. Kalinkin. "Closed shells for Z > 82 and N > 126 in a diffuse potential well". In: *Physics Letters* 22.4 (1966), pp. 500–502. DOI: https://doi.org/10.1016/0031-9163(66)91243-1.

[2] W. D. Myers and W. J. Swiatecki. "Nuclear masses and deformations". In: *Nuclear Physics* 81.1 (1966), pp. 1–60. DOI: https://doi.org/10.1016/0029-5582(66)90639-0.

[3] L. Örström and J. Reedijk. "Names and symbols of the elements with atomic numbers 113, 115, 117 and 118 (IUPAC Recommendations 2016)". In: *Pure and Applied Chemistry* 88.12 (2016), pp. 1225–1229. DOI: https://doi.org/10.1515/pac-2016-0501.

[4] S. Hofmann and G. Münzenberg. "Discovery of the Heaviest Elements". In: *Reviews of Modern Physics* 72 (July 2000). DOI: 10.1103/RevModPhys.72.733.

[5] Walter Loveland. "Synthesis of new neutron-rich heavy nuclei: An experimentalist's view". In: *Fission and Properties of Neutron-Rich Nuclei* (Jan. 2013), pp. 295–392. DOI: 10.1142/9789814525435_0032.

[6] W. Loveland. "Synthesis of transactinide nuclei using radioactive beams". In: *Phys. Rev. C* 76 (1 July 2007), p. 014612. DOI: 10.1103/PhysRevC.76.014612. URL: https://link.aps.org/doi/10.1103/PhysRevC.76.014612.

[7] "Quantum coherence and decoherence in low energy nuclear collisions: from superposition to irreversibility". In: *Nuclear Physics A* 834.1 (2010). The 10th International Conference on Nucleus-Nucleus Collisions (NN2009), pp. 117c–122c. ISSN: 0375-9474. DOI: https://doi.org/10.1016/j.nuclphysa.2009.12.019.

[8] N. Bohr. "Neutron Capture and Nuclear Constitution". In: *Nature* 137 (1936), pp. 344–348. DOI: https://doi.org/10.1038/137344a0.

[9] W. Loveland, D. Peterson, and A. M. Vinodkumar. "Fusion Enhancement in the $^{38}$S + $^{208}$Pb reaction". In: *Physical Review C* 74.4 (2006), p. 044607. DOI: https://doi.org/10.1103/PhysRevC.74.044607.

[10] K. E. Zyromski et al. "Fusion enhancement in the $^{32,38}$S+$^{181}$Ta reaction". In: *Phys. Rev. C* 63 (2 Jan. 2001), p. 024615. DOI: 10.1103/PhysRevC.63.024615.

[11] K. E. Zyromski et al. “Fusion enhancement with neutron-rich radioactive beams”. In: *Phys. Rev. C* 55 (2 Feb. 1997), R562–R565. DOI: 10.1103/PhysRevC.55.R562.

[12] R. Bass. “Fusion of heavy nuclei in a classical model”. In: *Nuclear Physics A* 231.1 (1974), pp. 45–63. DOI: https://doi.org/10.1016/0375-9474(74)90292-9.

[13] R. Bass. *Nuclear Reactions with Heavy Ions*. 1st ed. Springer-Verlag Berlin Heidelberg, 1980. ISBN: 978-3-540-09611-5.

[14] D. J. Hinde et al. “Isotopic dependence of fusion barrier energies in reactions forming heavy elements”. In: *Phys. Rev. C* 75 (5 May 2007), p. 054603. DOI: 10.1103/PhysRevC.75.054603.

[15] D. J. Hinde et al. “Isotopic dependence of fusion barrier energies in reactions forming heavy elements”. In: *Phys. Rev. C* 75 (5 May 2007), p. 054603. DOI: 10.1103/PhysRevC.75.054603.

[16] Roger D. Woods and David S. Saxon. “Diffuse Surface Optical Model for Nucleon-Nuclei Scattering”. In: *Phys. Rev.* 95 (2 July 1954), pp. 577–578. DOI: 10.1103/PhysRev.95.577.

[17] “Fusion barriers, empirical and theoretical: Evidence for dynamic deformation in sub-barrier fusion”. In: *Physics Reports* 69.5 (1981), pp. 373–399. ISSN: 0370-1573. DOI: https://doi.org/10.1016/0370-1573(81)90094-6.

[18] “Fusion of 16O + 144Sm at sub-barrier energies”. In: *Physics Letters B* 176.3 (1986), pp. 322–326. ISSN: 0370-2693. DOI: https://doi.org/10.1016/0370-2693(86)90172-3.

[19] D. Brink. *Semi-Classical Methods for Nucleus-Nucleus Scattering*. Cambridge University Press, 2009. ISBN: 0521114381.

[20] K. Hagino and A. B. Balantekin. “WKB approximation for multichannel barrier penetrability”. In: *Physical Review A* 70.3 (2004), p. 032106. DOI: https://doi.org/10.1103/PhysRevA.70.032106.

[21] M. Dasgupta et al. “Measuring Barriers to Fusion”. In: *Annual Review of Nuclear and Particle Physics* 48.1 (1998), pp. 401–461. DOI: https://doi.org/10.1103/PhysRevLett.105.252502.

[22] J. R. Leigh et al. "Barrier distributions from the fusion of oxygen ions with $^{144,148,154}$Sm and $^{1}$86W". In: *Physical Review C* 52.6 (1995), p. 3151. DOI: https://doi.org/10.1103/PhysRevC.52.3151.

[23] R. G. Stokstad et al. "Effect of Nuclear Deformation on Heavy-Ion Fusion". In: *Physical Review Letters* 41.7 (1978), p. 465. DOI: https://doi.org/10.1103/PhysRevLett.41.465.

[24] A. N. Andreyev et al. "New Type of Asymmetric Fission in Proton-Rich Nuclei". In: *Physical Review Letters* 105.25 (2010), p. 252502. DOI: https://doi.org/10.1103/PhysRevLett.105.252502.

[25] Guillaume Scamps and Kouichi Hagino. "Multidimensional fission model with a complex absorbing potential". In: *Phys. Rev. C* 91 (4 Apr. 2015), p. 044606. DOI: 10.1103/PhysRevC.91.044606. URL: https://link.aps.org/doi/10.1103/PhysRevC.91.044606.

[26] Michael Bender et al. "Future of Nuclear Fission Theory". In: *Journal of Physics G: Nuclear and Particle Physics* (July 2020). DOI: 10.1088/1361-6471/abab4f.

[27] P. Möller and et al. "Nuclear fission modes and fragment mass asymmetries in a five-dimensional deformation space". In: *Nature* 409 (2001), pp. 785–790. DOI: https://doi.org/10.1038/35057204.

[28] M. BRACK et al. "Funny Hills: The Shell-Correction Approach to Nuclear Shell Effects and Its Applications to the Fission Process". In: *Rev. Mod. Phys.* 44 (2 Apr. 1972), pp. 320–405. DOI: 10.1103/RevModPhys.44.320. URL: https://link.aps.org/doi/10.1103/RevModPhys.44.320.

[29] S. Bjørnholm and J. E. Lynn. "The double-humped fission barrier". In: *Rev. Mod. Phys.* 52 (4 Oct. 1980), pp. 725–931. DOI: 10.1103/RevModPhys.52.725. URL: https://link.aps.org/doi/10.1103/RevModPhys.52.725.

[30] H. Krappe and K. Pomorski. *Theory of Nuclear Fission*. Springer, Berlin, Heidelberg, 2012. ISBN: 978-3-642-23515-3.

[31] Gamow G. and Rutherford Ernest. "Mass defect curve and nuclear constitution". In: *Proceddings of the Royal Society A* 126 (1930), pp. 632–644. DOI: https://doi.org/10.1098/rspa.1930.00320.

[32] A.V. Ignatyuk et al. "The shape of the heated fast-rotating nuclei". In: *Nuclear Physics A* 346.1 (1980), pp. 191–215. ISSN: 0375-9474. DOI: https://doi.org/10.

1016/0375-9474(80)90497-2. URL: http://www.sciencedirect.com/science/article/pii/0375947480904972.

[33] V. M. Strutinsky. "Shell effects in nuclear masses and deformation energies". In: *Nuclear Physics A* 95.2 (1967), pp. 420–442. DOI: https://doi.org/10.1016/0375-9474(67)90510-6.

[34] Walter D. Loveland, David J. Morrissey, and Glenn T. Seaborg. *Modern Nuclear Chemistry*. John Wiley Sons, Inc, 2001. ISBN: 9780471115328.

[35] Niels Bohr and John Archibald Wheeler. "The Mechanism of Nuclear Fission". In: *Phys. Rev.* 56 (5 Sept. 1939), pp. 426–450. DOI: 10.1103/PhysRev.56.426. URL: https://link.aps.org/doi/10.1103/PhysRev.56.426.

[36] H. Rossner, J. R. Huizenga, and W. U. Schröder. "Fission fragment angular distributions". In: *Phys. Rev. C* 33 (2 Feb. 1986), pp. 560–575. DOI: 10.1103/PhysRevC.33.560.

[37] Arnold J. Sierk. "Macroscopic model of rotating nuclei". In: *Phys. Rev. C* 33 (6 June 1986), pp. 2039–2053. DOI: 10.1103/PhysRevC.33.2039. URL: https://link.aps.org/doi/10.1103/PhysRevC.33.2039.

[38] C. R. Morton et al. "Resolution of the anomalous fission fragment anisotropies for the $^{16}$O + $^{208}$Pb reaction". In: *Phys. Rev. C* 52 (1 July 1995), pp. 243–251. DOI: 10.1103/PhysRevC.52.243.

[39] H. A. Kramers. "Brownian motion in a field of force and the diffusion model of chemical reactions". In: *Physical Review C* 7.4 (1940), pp. 284–304. DOI: https://doi.org/10.1016/S0031-8914(40)90098-2.

[40] V. E. Viola, K. Kwiatkowski, and M. Walker. "Systematics of fission fragment total kinetic energy release". In: *Physical Review C* 31.4 (1985), p. 1550. DOI: https://doi.org/10.1103/PhysRevC.31.1550.

[41] J.A. Maruhn et al. "The TDHF code Sky3D". In: *Computer Physics Communications* 185.7 (2014), pp. 2195–2216. ISSN: 0010-4655. DOI: https://doi.org/10.1016/j.cpc.2014.04.008. URL: http://www.sciencedirect.com/science/article/pii/S0010465514001313.

[42] Md Afibuzzaman, Bastian Schuetrumpf, and Hasan Metin Aktulga. "Scalable nuclear density functional theory with Sky3D". In: *Computer Physics Communications* 223 (2018), pp. 34–44. ISSN: 0010-4655. DOI: https://doi.org/10.1016/j.cpc.

2017.10.009. URL: http://www.sciencedirect.com/science/article/pii/S0010465517303491.

[43] W. Ryssens et al. "Solution of the Skyrme–HF+BCS equation on a 3D mesh, II: A new version of the Ev8 code". In: *Computer Physics Communications* 187 (2015), pp. 175–194. ISSN: 0010-4655. DOI: https://doi.org/10.1016/j.cpc.2014.10.001. URL: http://www.sciencedirect.com/science/article/pii/S0010465514003361.

[44] C. Simenel and A.S. Umar. "Heavy-ion collisions and fission dynamics with the time-dependent Hartree–Fock theory and its extensions". In: *Progress in Particle and Nuclear Physics* 103 (2018), pp. 19–66. ISSN: 0146-6410. DOI: https://doi.org/10.1016/j.ppnp.2018.07.002. URL: http://www.sciencedirect.com/science/article/pii/S0146641018300693.

[45] R. Hasse and W. Myers. *Geometrical Relationships of Macroscopic Nuclear Physics*. Springer Series in Nuclear and Particle Physics. Springer-Verlag Berlin Heidelberg, 1988. ISBN: 978-3-642-83019-8.

[46] Karl-Heinz Schmidt et al. "General Description of Fission Observables: GEF Model Code". In: (2015). DOI: http://hal.in2p3.fr/in2p3-01241907.

[47] C. Schmitt, K.-H. Schmidt, and B. Jurado. "Benchmark of the GEF code for fission-fragment yields over an enlarged range in fissioning nucleus mass, excitation energy, and angular momentum". In: *Phys. Rev. C* 98 (4 Oct. 2018), p. 044605. DOI: 10.1103/PhysRevC.98.044605. URL: https://link.aps.org/doi/10.1103/PhysRevC.98.044605.

[48] K.-H. Schmidt et al. "General Description of Fission Observables: GEF Model Code". In: *Nuclear Data Sheets* 131 (2016). Special Issue on Nuclear Reaction Data, pp. 107–221. ISSN: 0090-3752. DOI: https://doi.org/10.1016/j.nds.2015.12.009. URL: http://www.sciencedirect.com/science/article/pii/S0090375215000745.

[49] *Statistical Model of Decay of Excited Nuclei*. URL: nrv.jinr.ru/nrv/webnrv/evaporation_residue_theory/description/Decay%20of%20excited%20nuclei.pdf.

[50] Walter Hauser and Herman Feshbach. "The Inelastic Scattering of Neutrons". In: *Physical Review* 87.2 (1952), p. 366. DOI: https://doi.org/10.1103/PhysRev.87.366.

[51] A. Bohr and B. R. Mottleson. In: *Nuclear Structure* 1 (1975).

[52] Peter Möller et al. "Fission barriers at the end of the chart of the nuclides". In: *Phys. Rev. C* 91 (2 Feb. 2015), p. 024310. DOI: 10.1103/PhysRevC.91.024310. URL: https://link.aps.org/doi/10.1103/PhysRevC.91.024310.

[53] R. J. Charity. "Systematic description of evaporation spectra for light and heavy compound nuclei". In: *Physical Review C* 82.1 (2010), p. 014610. DOI: https://doi.org/10.1103/PhysRevC.82.014610.

[54] B. Blank et al. "Evaluation of fusion-evaporation cross-section calculations". In: *Nuclear Instruments and Methods in Physics Research Section B: Beam Interactions with Materials and Atoms* 416 (2018), pp. 41–49. ISSN: 0168-583X. DOI: https://doi.org/10.1016/j.nimb.2017.12.003. URL: http://www.sciencedirect.com/science/article/pii/S0168583X17310054.

[55] J.S. Randhawa et al. "Beam-induced space-charge effects in time projection chambers in low-energy nuclear physics experiments". In: *Nuclear Instruments and Methods in Physics Research Section A: Accelerators, Spectrometers, Detectors and Associated Equipment* 948 (2019), p. 162830. DOI: https://doi.org/10.1016/j.nima.2019.162830.

[56] D. R. Nygren. "The Time Projection Chamber — A New 4pi Detector for Charged Particles". In: *in Proceedings of the 1974 pep summer study* (1974), pp. 58–79. DOI: http://lss.fnal.gov/conf/C740805/p58.pdf.

[57] Thomas Lohse and Werner Witzeling. "The Time Projection Chamber". In: *Instrumentation in High Energy Physics*, pp. 81–155. DOI: 10.1142/9789814360333_0002.

[58] S. Beceiro-Novo et al. "Active targets for the study of nuclei far from stability". In: *Progress in Particle and Nuclear Physics* 84 (2015), pp. 124–165. ISSN: 0146-6410. DOI: https://doi.org/10.1016/j.ppnp.2015.06.003.

[59] Lisa Carpenter. "Cluster Structure and 3-Body Decay in $^{14}$C". PhD thesis. Michigan State University, 2019.

[60] D. Suzuki et al. "Prototype AT-TPC: Toward a new generation active target time projection chamber for radioactive beam experiments". In: *Nuclear Instruments and Methods in Physics Research Section A: Accelerators, Spectrometers, Detectors and Associated Equipment* 691.1 (2012), pp. 39–54. DOI: https://doi.org/10.1016/j.nima.2012.06.050.

[61] D. Suzuki et al. "Resonant $\alpha$ scattering of $^{6}$He: Limits of clustering in $^{10}$Be". In: *Phys. Rev. C* 87 (5 May 2013), p. 054301. DOI: 10.1103/PhysRevC.87.054301. URL: https://link.aps.org/doi/10.1103/PhysRevC.87.054301.

[62] J. Bradt et al. "Commissioning of the Active-Target Time Projection Chamber". In: *Nuclear Instruments and Methods in Physics Research Section A: Accelerators, Spectrometers, Detectors and Associated Equipment* 875 (2017), pp. 65–79. ISSN: 0168-9002. DOI: https://doi.org/10.1016/j.nima.2017.09.013. URL: http://www.sciencedirect.com/science/article/pii/S0168900217309683.

[63] Y. Giomataris et al. ""MICROMEGAS: a high-granularity po-sition sensitive gaseous detector for high particle flux environments". In: *Nuclear Instrumental Methods A* 376 (1996), pp. 29–35. DOI: https://doi.org/10.1016/0168-9002(96)00175-1.

[64] Emanuel Pollacco et al. "GET: A Generic Electronic System for TPCs for Nuclear Physics Experiments". In: *Physics Procedia* 37 (2012). Proceedings of the 2nd International Conference on Technology and Instrumentation in Particle Physics (TIPP 2011), pp. 1799–1804. ISSN: 1875-3892. DOI: https://doi.org/10.1016/j.phpro.2012.02.506.

[65] S. Anvar et al. "AGET, the GET front-end ASIC, for the readout of the Time Projection Chambers used in nuclear physic experiments". In: *2011 IEEE Nuclear Science Symposium Conference Record*. 2011, pp. 745–749.

[66] P. Baron and E. Delagnes. *AGET, a Front End ASIC for Active Time Projection Chamber: Data Sheet*. 2013.

[67] S. Anvar et al. "AGET, the GET front-end ASIC, for the readout of the Time Projection Chambers used in nuclear physic experiments". In: *2011 IEEE Nuclear Science Symposium Conference Record*. 2011, pp. 745–749. DOI: 10.1109/NSSMIC.2011.6154095.

[68] P. Baron and E. Delagnes. "AGET, a Front End ASIC for Active Time Projection Chamber: Data Sheet". In: (2013).

[69] F. Marti et al. "Commissioning of the Coupled Cyclotron system at NSCL". In: 600 (Dec. 2001). DOI: 10.1063/1.1435199.

[70] D.J. Morrissey et al. "Commissioning the A1900 projectile fragment separator". In: *Nuclear Instruments and Methods in Physics Research Section B: Beam Interactions with Materials and Atoms* 204 (2003). 14th International Conference on Electromagnetic Isotope Separators and Techniques Related to their Applications, pp. 90–96.

ISSN: 0168-583X. DOI: https://doi.org/10.1016/S0168-583X(02)01895-5. URL: http://www.sciencedirect.com/science/article/pii/S0168583X02018955.

[71] Oliver Kester et al. "ReA3 - the Rare Isotope Re-accelerator at MSU". In: *25th International Linear Accelerator Conference*. 2011, MO203.

[72] D. C. Rafferty et al. "Multinucleon transfer in $^{16,18}$O,$^{19}$F+$^{208}$Pb reactions at energies near the fusion barrier". In: *Physical Review C* 94.2 (2016), p. 024607. DOI: https://doi.org/10.1103/PhysRevC.94.024607.

[73] James F. Ziegler, M.D. Ziegler, and J.P. Biersack. "SRIM – The stopping and range of ions in matter (2010)". In: *Nuclear Instruments and Methods in Physics Research Section B: Beam Interactions with Materials and Atoms* 268.11 (2010). 19th International Conference on Ion Beam Analysis, pp. 1818–1823. ISSN: 0168-583X. DOI: https://doi.org/10.1016/j.nimb.2010.02.091. URL: http://www.sciencedirect.com/science/article/pii/S0168583X10001862.

[74] M. Anderson et al. "The STAR time projection chamber: a unique tool for studying high multiplicity events at RHIC". In: *Nuclear Instruments and Methods in Physics Research Section A: Accelerators, Spectrometers, Detectors and Associated Equipment* 499.2 (2003), pp. 659–678. ISSN: 0168-9002. DOI: https://doi.org/10.1016/S0168-9002(02)01964-2.

[75] *Random Sample Consensus*. URL: https://en.wikipedia.org/wiki/Random_sample_consensus. (accessed: 03.05.2020).

[76] Yassid Ayyad et al. "Novel particle tracking algorithm based on the Random Sample Consensus Model for the Active Target Time Projection Chamber (AT-TPC)". In: *Nucl. Instrum. Meth. A* 880 (2018), pp. 166–173. DOI: 10.1016/j.nima.2017.10.090.

[77] A. Lapierre et al. "First two operational years of the electron-beam ion trap charge breeder at the National Superconducting Cyclotron Laboratory". In: *Phys. Rev. Accel. Beams* 21 (5 May 2018), p. 053401. DOI: 10.1103/PhysRevAccelBeams.21.053401. URL: https://link.aps.org/doi/10.1103/PhysRevAccelBeams.21.053401.

[78] R. Vandebosch and J.R. Huizenga. *Nuclear Fission*. Academic Press, New York/London, 1973. ISBN: 978-0-12-710850-6.

[79] S. S. Kapoor and V. S. Ramamurthy. "Fragment angular distributions in fission and fission-like reactions". In: *J Phys.* 33.1 (1989), pp. 161–174.

[80] B. B. Back and et al. "Angular distributions in heavy-ion-induced fission". In: *Physical Review C* 32.1 (1985), p. 195. DOI: https://doi.org/10.1103/PhysRevC.32.195.

[81] A. Breskin et al. "A concise review on THGEM detectors". In: *Nuclear Instruments and Methods in Physics Research Section A: Accelerators, Spectrometers, Detectors and Associated Equipment,* 598.1 (2009), pp. 107–111. DOI: https://doi.org/10.1016/j.nima.2008.08.062.

[82] Yorito Yamaguchi et al. "Development and performance evaluation of Thick-GEM". In: vol. 6. Jan. 2007, pp. 4645–4648. ISBN: 978-1-4244-0922-8. DOI: 10.1109/NSSMIC.2007.4437144.

[83] Fabio Sauli. "The gas electron multiplier (GEM): Operating principles and applications". In: *Nuclear Instruments and Methods in Physics Research Section A: Accelerators, Spectrometers, Detectors and Associated Equipment,* 805.1 (2016), pp. 2–24. DOI: https://doi.org/10.1016/j.nima.2015.07.060.

[84] T.R. Ophel et al. "The 14UD pelletron accelerator at the Australian National University". In: *Nuclear Instruments and Methods* 122 (1974), pp. 227–234. ISSN: 0029-554X. DOI: https://doi.org/10.1016/0029-554X(74)90485-6. URL: http://www.sciencedirect.com/science/article/pii/0029554X74904856.

[85] D.Allan Bromley. "The development of electrostatic accelerators". In: *Nuclear Instruments and Methods* 122 (1974), pp. 1–34. ISSN: 0029-554X. DOI: https://doi.org/10.1016/0029-554X(74)90468-6. URL: http://www.sciencedirect.com/science/article/pii/0029554X74904686.

[86] "A cesium-sputtering negative ion source for AMS investigations". In: *Nuclear Instruments and Methods in Physics Research Section A: Accelerators, Spectrometers, Detectors and Associated Equipment* 382.1 (1996). Proceedings of the Seventh International Conference on Heavy Ion Accelerator Technology, pp. 327–331. ISSN: 0168-9002. DOI: https://doi.org/10.1016/S0168-9002(96)00457-3.

[87] R. Middleton. "A survey of negative ion sources for tandem accelerators". In: *Nuclear Instruments and Methods* 122 (1974), pp. 35–43. ISSN: 0029-554X. DOI: https://doi.org/10.1016/0029-554X(74)90469-8.

[88] K. Brand. "Improvement of the reflected beam sputter source". In: *Nuclear Instruments and Methods* 154.3 (1978), pp. 595–596. ISSN: 0029-554X. DOI: https://doi.org/10.1016/0029-554X(78)90095-2.

[89] V.S. Nikolaev and I.S. Dmitriev. "On the equilibrium charge distribution in heavy element ion beams". In: *Physics Letters A* 28.4 (1968), pp. 277–278. ISSN: 0375-9601. DOI: https://doi.org/10.1016/0375-9601(68)90282-X.

[90] J.L. Yntema. "Heavy ion stripping in tandem accelerator terminals". In: *Nuclear Instruments and Methods* 122 (1974), pp. 45–52. ISSN: 0029-554X. DOI: https://doi.org/10.1016/0029-554X(74)90470-4.

[91] R.H. Spear et al. "Energy calibration of the A.N.U. 14UD Pelletron accelerator". In: *Nuclear Instruments and Methods* 147.4 (1977), pp. 455–459.

[92] D. J. Hinde et al. "Conclusive evidence for the influence of nuclear orientation on quasifission". In: *Phys. Rev. C* 53 (3 Mar. 1996), pp. 1290–1300. DOI: 10.1103/PhysRevC.53.1290.

[93] D. J. Hinde et al. "Conclusive evidence for the influence of nuclear orientation on quasifission". In: *Phys. Rev. C* 53 (3 Mar. 1996), pp. 1290–1300. DOI: 10.1103/PhysRevC.53.1290.

[94] R. Leo. *Techniques for Nuclear and Particle Physics Experiments*. 2nd ed. Springer-Verlag Berlin Heidelberg, 1994. ISBN: 978-3-540-57280-0. DOI: 10.1007/978-3-642-57920-2.

[95] G. Knoll. *Radiation detection and measurement*. 4th ed. John Wiley  Sons, 2010. ISBN: 9780470131480.

[96] Dongyun Jeung. "Investigation of the Energy Dissapation and Capture through Fission Measurements". PhD thesis. Australian National University, Oct. 2018.

[97] Rene Brun and Fons Rademakers. "ROOT — An object oriented data analysis framework". In: *Nuclear Instruments and Methods in Physics Research Section A: Accelerators, Spectrometers, Detectors and Associated Equipment* 389.1 (1997). New Computing Techniques in Physics Research V, pp. 81–86. ISSN: 0168-9002. DOI: https://doi.org/10.1016/S0168-9002(97)00048-X.

[98] G. Arfken, H. Weber, and F. Harris. *Mathematical Methods for Physicists: A Comprehensive Guide*. 7th ed. Academic Press, 2012. ISBN: 9780123846549.

[99] S. Giraud. "Light particle induced fission, test of a new time-difference model". Master's Thesis. MA thesis. Australian National University, July 2015.

[100] K. Krane. *Introductory Nuclear Physics*. 3rd ed. John Wiley Sons, 1987. ISBN: 978-0-471-80553-3.

[101] C.R. Morton. "Fusion Barrier Distributions and Fission Fragment Anisotropies in Heavy-Ion Fusion Reactions". PhD thesis. Australian National University, 1995.

[102] D.J.Hinde et al. "Fission barriers of Pb nuclei at high angular momentum". In: *Nuclear Physics A* 398.2 (1983), pp. 308–324. DOI: https://doi.org/10.1016/0375-9474(83)90489-X.

[103] O. Tarasov et al. "The code LISE: a new version for "Windows"". In: *Nuclear Physics A* 701.1 (2002). 5th International Conference on Radioactive Nuclear Beams, pp. 661–665. ISSN: 0375-9474. DOI: https://doi.org/10.1016/S0375-9474(01)01663-3. URL: http://www.sciencedirect.com/science/article/pii/S0375947401016633.

[104] O.B. Tarasov and D. Bazin. "Development of the program LISE: application to fusion–evaporation". In: *Nuclear Instruments and Methods in Physics Research Section B: Beam Interactions with Materials and Atoms* 204 (2003). 14th International Conference on Electromagnetic Isotope Separators and Techniques Related to their Applications, pp. 174–178. ISSN: 0168-583X. DOI: https://doi.org/10.1016/S0168-583X(02)01917-1. URL: http://www.sciencedirect.com/science/article/pii/S0168583X02019171.

[105] W. J. Świątecki, K. Siwek-Wilczyńska, and J. Wilczyński. "Fusion by diffusion. II. Synthesis of transfermium elements in cold fusion reactions". In: *Physical Review C* 71.1 (2005), p. 014602. DOI: https://doi.org/10.1103/PhysRevC.71.014602.

[106] P.R.Christensen and A.Winther. "The evidence of the ion-ion potentials from heavy ion elastic scattering". In: *Physics Letters B* 65.1 (1976), pp. 19–22. DOI: https://doi.org/10.1016/0370-2693(76)90524-4.

[107] J. J. Kolata et al. "Fusion of $^{124,132}$Sn with $^{40,48}$Ca". In: *Physical Review C* 85.5 (2012), p. 054603. DOI: https://doi.org/10.1103/PhysRevC.85.054603.

[108] I. Tsekhanovich et al. "Observation of the competing fission modes in $^{178}$Pt". In: *Physics Letters B* 790 (2019), pp. 583–588. DOI: https://doi.org/10.1016/j.physletb.2019.02.006.

[109] D. J. Hinde et al. "Isotopic dependence of fusion barrier energies in reactions forming heavy elements". In: *Physical Review C* 75.5 (2007), p. 054603. DOI: https://doi.org/10.1103/PhysRevC.75.054603.